


Doctoral Dissertation
Doctoral Program in Physics (32.nd cycle)

Electric field effect in disordered thin films

Francesco Galanti

* * * * * *

Supervisor
Prof. R. S. Gonnelli

Doctoral Examination Committee:
Prof. A. Perali, Referee, Università di Camerino, Italy
Prof. J. Ye, Referee, University of Groningen, The Netherlands
Prof. D. Daghero, Politecnico di Torino, Italy
Prof. G. Ghigo, Politecnico di Torino, Italy
Dr. A. Rossi, Istituto Nazionale di Ricerca Metrologica, Italy

Politecnico di Torino
2019

I hereby declare that, the contents and organisation of this dissertation constitute my own original work and does not compromise in any way the rights of third parties, including those relating to the security of personal data.

. . . . . .

Francesco Galanti

Turin, 2019

Summary

Granular conductors acquired importance in the past decades because of their tunable electronic properties, which can be controlled at the nanoscale. Their importance comes from the fact that they combine the mesoscopic properties that dominate inside each grain and the collective properties of coupled nanocrystals. However, the ease of adjusting their electronic properties makes them convenient also from the fundamental point of view. In recent years the electric double layer (EDL) gating has received great attention as a powerful tool to efficiently control the surface carrier density of a wide range of different materials, reaching almost two order of magnitude higher electric fields than standard well-known field effect transistor (FET) architecture.

In this Ph.D. thesis we performed field effect measurements on different disordered thin-film systems: nominally, P-doped Barium Iron Arsenide ($BaFe_2(As,P)_2$), nano-crystalline diamond (NCD), inkjet-printed graphene and MXene, two of them being metallic systems, and the other two being carbon based semiconductors. We also performed preliminary measurements on gold and niobium nitride (NbN) with the aim of exploring the properties of ultrathin films via the ferroelectric gating technique.

Chapter 1 will introduce three different techniques to perform electric-field-effect experiments. We will introduce the solid gating technique, as a well-established tool to modulate the transport properties of low-density carrier systems; Then, the ionic gating technique, as a tool that allows to go beyond the solid-gating technique limits as far as the maximum induced charge density is concerned; Finally, the ferroelectric gating technique, which combines the ferroelectric and the piezoelectric effects to modulate the transport properties of the studied material. We will investigate the three techniques and we will resume the pros and cons for each of them.

Chapter 2 will present the results obtained on optimally-doped $BaFe_2(As,P)_2$ ultrathin films (10 nm) epitaxially grown on MgO substrates via molecular beam epitaxy. We controlled the charge density at the film surface by means of ionic gating. In order to suppress undesirable electrochemical interactions with the sample,

we designed and employed an optimized electrolyte. The resulting modulations to the resistivity were found to be compatible with an electrostatic operation of the ionic gate, with a scaling on the induced charge density consistent with an asymmetric scattering efficiency between cations and anions. At low temperatures, the T_c was suppressed both upon electron and hole doping, indicating that field-effect doping and isovalent P substitution share the same T_c maximum in the Ba-122 phase diagram. We thus demonstrated that the superconductivity (SC) is fully optimized by P substitution and any further deviation from this optimal condition is detrimental to the SC state. Additionally, we showed that field-effect doping leads to a broadening of the resistive transition. This indicates that gate-induced modulations to the SC order parameter in Ba-122 are not uniform across the entire film thickness.

Chapter 3 will show the results of ionic gating experiments on nanocrystalline boron-doped diamond (300 nm thick films) grown by Micro Wave Chemical Vapor Deposition (MW CVD). The presence of boron doping enhances the maximum induced carrier density with respect to undoped films and single crystals. By disentangling the sheet conductance of the field-induced conducting layer from that of the underlying bulk, we were able to probe the surface transport properties as a function of temperature and induced charge density. By increasing the hole density, we observed a transition from the variable-range hopping to the quantum critical regime of the insulator-to-metal transition in the surface conducting layer. However, the insulator-to-metal transition is never reached at the surface: this frustrated behaviour may be due to an increased disorder arising from a combination of surface roughness and extra scattering centres introduced by the ionic gate.

Chapter 4 will present the results obtained on graphene and MXene (specifically, Ti_3C_2) inkjet printed thin films. In the graphene-ink films, the sheet conductance reveals a dominating variable range hopping regime for 3-dimensional systems without the opening of a Coulomb gap. Electric field effect mobility measurements and magnetoresistance measurements confirm the aforementioned transport mechanism and allows to recover the hopping parametes. In MXene-ink films we observed a metallic behaviour that is closely similar to the epitaxially grown counterparts. An upturn of the resistance at low temperatures suggests the presence of incoming localization. Magnetotransport measurements reveals weak localization and the study of this allows to recover the characteristic lengths of the phenomenon.

Chapter 5 will show some preliminary results of piezoelectric gating technique on CVD gold thin films. The ferroelectric characterization of PZT was used to modulate the resistance of the gold film. With further increasing the maximum applied electric field across the PZT activates the piezoelectric polarization: this

latter has stronger effects on the gold film transport properties, covering the ferroelectric effect.
We then performed preliminary ionic-gating experiments on ultrathin CVD NbN films. Besides of hampering the superconducting properties, reducing the sample thickness has the positive effect of enhancing the capability of the SC T_c (up to 0.5 K). However, the maximum induced surface charge density we reached is $\sim 10^{14}$ e^-/cm^2, that is one order of magnitude lower than what already found in the literature for ionic-gating technique on thicker NbN films. We account this to the formation of a dead layer at the surface.
Thus, we suggest that there are perspectives of exploiting the ferroelectric gating to tune the superconductivity making these films actual superconducting transistors at low temperature. The application of ferroelectric gating technique to NbN ultrathin films is ongoing, and are not treated in this work.

Concluding, we will present future perspectives about each of the studied materials and techniques.

Acknowledgements

I am using this opportunity to express my gratitude to everyone who supported me throughout the course of this PhD program.

I would first and foremost thank my supervisor, Prof. Renato Gonnelli for his guidance, continuous support and knowledge.

I would also like to thank Dr. Erik Piatti who provided insight and expertise that greatly assisted my research.

I would like to thank the other members of my research group: Prof. Dario Daghero, Prof. Gianni Ummarino, and Davide Romanin for their scientific support.

I would also like to thank the collaborators who provided me the samples I worked on. In particular, Prof. Felice Torrisi and Adrees Arbab, from the University of Cambridge, for the inkjet-printed devices, the preliminary characterizations and the fruitful discussions; Marco Colangelo and Prof. Karl Bergren, from the Massachusetts Institute of Technology, for the ultra-thin NbN films; Prof. Alberto Pasquarelli, from the University of Ulm, who provided the boron-doped diamond thin films; Prof. Takafumi Hatano, from Nagoya University, for the work on iron-based superconductors.
I would also like to thank Prof. Andrea Ferrari, from Cambridge Graphene Centre, for hosting me as a visiting student in his laboratories.

A special thanks to my fellows for daily life sharing: Anja Visocnik, Mina Golshan Koviji, Federico Fraternale and Antonio Gallerati.

Contents

Chapter 1

The electric field-effect doping

The electric field effect is a phenomenon that is at the heart of modern electronics. Indeed, it allows to control the current that flows through a properly designed semiconducting channel and, thus, it helps building up a logic switch. For this reason, the electric field effect has been fundamental for the development of many technological applications. Moreover, it has also been demonstrated to be a very powerful tool for fundamental studies because it allows to change the native carrier density of a material via a pure electrostatic doping: field-effect-based techniques allow to control the charge doping while avoiding the undesired side effects introduced by, for example, chemical substitution.
The different materials investigated in this work required the exploitation of different field-effect techinques. Thus, this Chapter reviews the concepts and methods at the core of the approaches we employed in the field-effect experiments discussed in this work.
We will first discuss the solid-gating technique, which is well established and the most used for technological applications. We exploited this technique in order to modulate the transport properties of disordered graphene-ink films and to determine their field-effect mobility.
We will then present the ionic-gating technique. This second approach allows to increase the magnitude of the electric field with respect to the solid-gating technique, which is often required for fundamental studies. In particular we exploited this technique to study two thin–film superconductors – NbN and $BaFe_2(As,P)_2$ – and nanocrystalline boron-doped diamond thin films.
We will finally discuss the ferroelectric-gating technique. We used this approach when we wanted to increase the induced charge density w.r.t. the solid-gating technique, while maintaining the possibility of tuning the electronic properties of the materials even at low temperatures. Moreover, it allows to avoid electrochemical interactions at the interface between an ionic liquid and the material under study.

1.1 The solid-gating technique

The first idea of a field-effect-based device dates back to 1926 when Julius Edgar Lilienfeld patented a forerunner of a modern field-effect transistor (FET) [1]. However, his idea never reached popularity because of the lack of a complete understanding of the physics behind it and also because he couldn't have access to high purity semiconductors at that time. More than three decades later, the invention of metal-oxide-semiconductor FET (MOSFET) at the Bell Labs in 1959 revolutionized the world of technology [2, 3]. The invention of MOSFET represented a true milestone in the field of semiconducting industry, laying the foundations for the development of digital devices for the next 60 years until nowadays. From that moment on, the electronic industry started developing silicon- and germanium-based transistors more and more efficient.

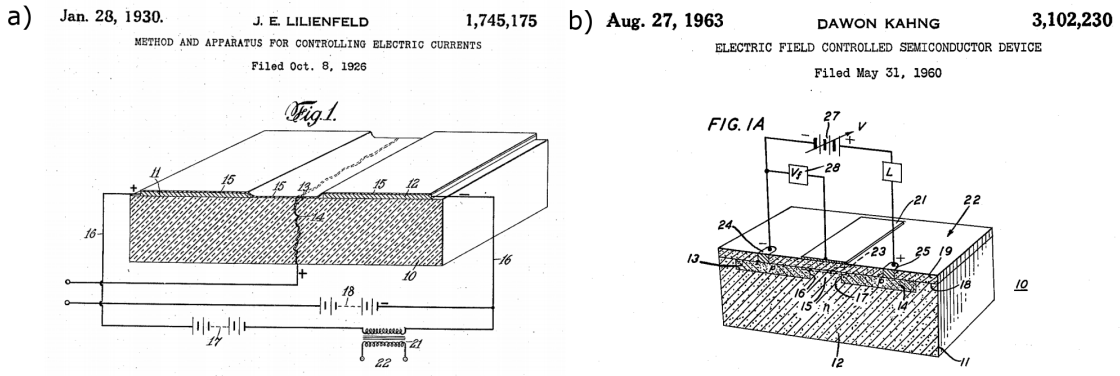

Figure 1.1: a) Initial patent of field-effect device submitted by Lilienfeld in 1926 [1]; b) The MOSFET patent submitted by Kahng in 1960 [2].

1.1.1 The metal-oxide-semiconductor field-effect transistor - MOSFET

The architecture of a MOSFET (see figure 1.2) is based on an asymmetric capacitor that uses a metal and a semiconductor as armatures. The MOSFET is a 4-terminal device: there are two contacts that act as source and drain of the electrons that flow in the channel, a gate contact and a bulk, or body, contact across which the gate voltage is applied. Usually the bulk contact is set at the same potential as the source contact. On the side of the semiconductor, that conventionally is represented at the bottom, there is a n-p-n or a p-n-p junction, where the heavily doped external regions are the reservoirs of the majority carriers, while the central region, i.e. the channel, is lightly-doped with dopants of the opposite sign to preclude the flow of the current when no gate voltage is applied. Depending on the

doping of the external regions it is possible to realize n-MOSFETs, if the external regions are n-doped, and p-MOSFETs if the external regions are p-doped. Up until 10 years ago, MOSFETs were built in a planar geometry; nowadays, technological constrains induced companies to develop 3D geometries to realize MOSFETs. Moreover, the dimensions of MOSFETs have gotten smaller with the passing of time down to few tens of nanometers. However, the basic principle remains the same.

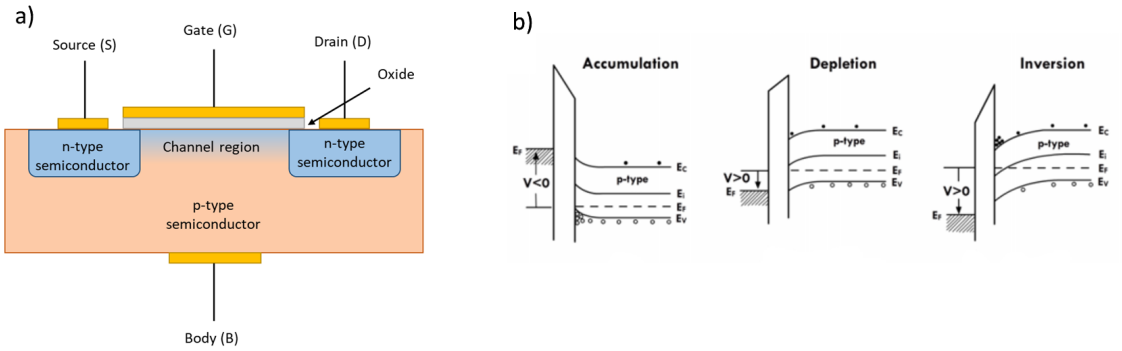

Figure 1.2: a) Cross section of a n-MOSFET: the flow of the source-drain current between the two heavily-doped islands is controlled by the transverse electric field applied from the gate pad. b) Simplified band diagram of the MOS junction in the case of a n-MOSFET in the accumulation, depletion and inversion regimes. [Adapted from [4]]

The MOSFET operation principle is based on the properties of the metal-oxide-semiconductor junction, which we here briefly describe in the case of an n-MOS junction.
The n-MOS junction behaviour is controlled by a gate voltage (V_G) applied from the metallic gate pad to the semiconductor across the junction. If we apply $V_G < 0$, the positive charges in the p-type semiconductor are driven towards the semiconductor-oxide interface, forming an accumulation layer where the positive carrier density is increased.
Oppositely, if we apply $V_G > 0$, the positive charges are repelled from the semiconductor-oxide interface and, thus, a depletion region with lower positive charge concentration forms in the semiconductor, close to the oxide. By further increasing the positive gate voltage applied to the metallic pad, negative charges start populating the semiconductor at the semiconductor-oxide interface – which is originally p-doped – forming an inversion layer (where the majority carrier sign is inverted). When the channel starts being populated by negative charges, the electronic current can flow from the heavily n-doped regions through the originally p-doped channel for the presence of electrons [4].

Figure 1.2b shows the formation of the accumulation, depletion and inversion regions upon different V_G applications: notice that, when a positive electric potential is applied, it bends the band structure in the semiconductor first forming a depletion layer, and then giving rise to an inversion layer populated by negative carriers. The thickness of the inversion layer at the interface can vary from few Angstroms to some nanometers, therefore the properties of the 2D insulator-semiconductor interface are crucial. In particular, high concentrations of surface states or dangling bonds due to impurities in the material can lead to a screening of the transverse field in the case of a p-MOSFET, or to the formation of a permanent inversion layer in the channel of a n-MOSFET even when no gate voltage is applied.
For this reason, FETs came out later than the bipolar junction transistors (BJTs): BJTs are based on the bulk properties of a double p-n junction; inversely, FETs working principle is heavily dependent on the physics that develops at the semiconductor-oxide interface and, thus, the production of working devices required to address the issues concerning the purity of the semiconductor at the interface. This is the reason why it took more than 3 decades from Lilienfeld's patent to get a FET working device.
Despite this delay, field-effect transistors bridged the gap with BJTs and nowadays almost the entirety of digital electronic devices are based on MOSFETs. The reason of this success can be identified in the development of a simpler fabrication technology, a better scalability to smaller dimensions and a much lower power consumption.

1.1.2 Threshold voltage and field-effect mobility

The microscopic expression of Ohm's law states that the current density is proportional to the electric field ($J = \sigma E$, where σ is the electrical conductivity), while in the free electron model $J = -envd$ ($J = epv_d$), where e is the electron charge, n (p) is the electron (hole) density and v_d is the drift velocity of the carriers. This means that in the semiconductor the conductance σ is proportional to the density of majority carriers, i.e. the transconductance (the source-drain conductance measured at constant V_{DS} and variable V_G applied) varies upon the application of the gate voltage: that is actually the primary figure of merit of a transconductance variable resistor (or transistor).
When the inversion region is formed by the application of a gate voltage, the majority carriers accumulate at the interface. The threshold voltage is the minimum gate-to-source voltage drop for which this inversion layer is formed:

$$V_{th} = V_{FB} + 2\Phi_p + \frac{1}{C_{OX}}\sqrt{2q\epsilon_s N_A 2\Phi_p} \tag{1.1}$$

where V_{FB} is the flat band voltage (i. e. the voltage you need to apply across the MOS junction in order to bend the band structure in such a way that the bands are

flat all over the system), Φ_p is defined as $q\Phi_p = E_{F_i} - E_F$ (being E_F the Fermi level and E_{F_i} the intrinsic Fermi level) and it depends on the doping concentration N_A, ϵ_s is the permittivity of the semiconductor and C_{OX} is the oxide specific capacitance. Typical values of V_{th} in a MOSFET are of the order of 1 V.
When a voltage drop V_{DS} is applied between the source and drain terminals, the inversion region is not uniform along the channel length L. Given that $V_G > V_{GD}+Vth$, where V_{GD} is the voltage drop between the gate and the drain terminals, the source-to-drain current I_{DS} can be expressed as a function of V_{th} as:

$$I_{DS} = \frac{\mu C_{OX} W}{L}[(V_G - V_{th})V_{DS} - \frac{V_{DS}^2}{2}] \tag{1.2}$$

Where W is the width of the channel and μ is the carrier mobility, that is also referred to as the field-effect mobility.
In the limit where V_{DS} is small, only the linear term remains. Now, if we calculate the differential transconductance for this region we obtain:

$$\frac{dI_{DS}}{dV_G} = \frac{\mu C_{OX} W}{L} V_{DS} \tag{1.3}$$

From which an explicit expression for the field-effect mobility comes out:

$$\mu = \frac{dG}{dV_G}\frac{L}{W}\frac{1}{C_{OX}} \tag{1.4}$$

Where $G = I_{DS}/V_{DS}$ is the channel conductance [4].

1.1.3 JFET, MESFET, TFT and Van-der-Waals based FET

As we have mentioned, the MOSFET is the most exploited FET, however there exist a wide variety of solid field-effect devices. To give an idea of how the same basic principles can be exploited to construct very different devices, we will briefly introduce some of the most widespread types of solid FETs.

The JFET A junction FET (JFET) is based on a doped channel surrounded by an inversely doped region (see Figure 1.3.a). The flow of the source-to-drain current is controlled by the gate voltage applied to the external region. By controlling the gate bias it is possible to induce an inversion region in the channel that squeezes of the channel itself, progressively reducing the conductive cross section until the pinch off voltage is reached. These kind of devices are said to be "naturally on" because the channel is conductive even without the application of the gate bias.

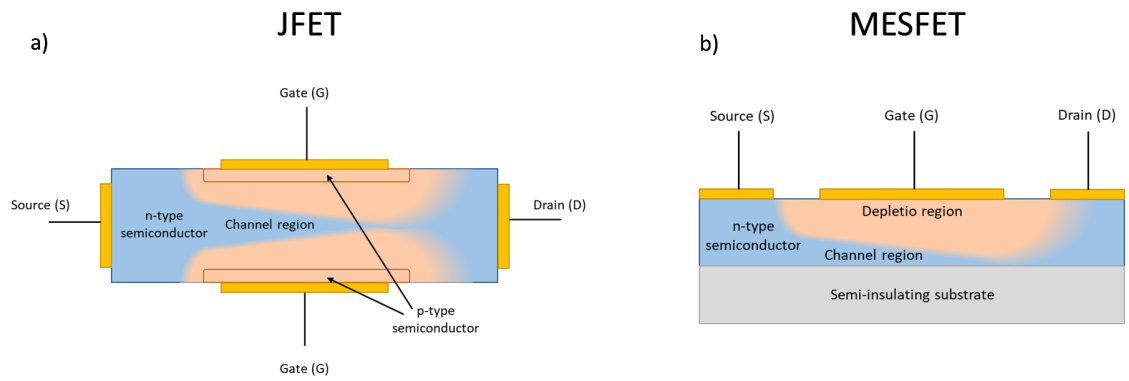

Figure 1.3: The depletion region in a JFET (a) and a MESFET (b) when they are biased for V_{DS} and V_G.

The MESFET In the MESFET structure a Schottky barrier is present between the metallic gate pad and the semiconducting channel, thus, even if there is no insulating layer between the metallic gate pad and the semiconductor, the current cannot flow through the junction. This allows the formation of a depletion layer that acts in a similar way as the JFET.
The first imagined FET exploited this structure.

The TFT A particular case of MOSFET is the family of thin film transistors (TFT): also this class of FETs is based on a metal-insulator-semiconductor junction. Often, the channel is made of a wide band gap semiconductor, thus, differently from MOSFETs, the conduction is achieved by an accumulation layer.
The realization of TFTs occurs via different steps of depositions on an insulating substrate (glass, mostly) [5] and each layer of the transistor is very thin – from which the name.
TFTs are growing in popularity because of the ease of fabrication with the modern nano-lithography and also because, as MOSFETs, they work on a naturally off state.
In the next chapters we will see that our devices show the same architecture of TFTs. Even though the channels of our devices are far from being wide energy gap semiconductors, nevertheless, we will exploit the TFT architecture to modulate the charge density of our thin films.

The Van der Waals FET Nano-layered FETs realized with van-der-Waals heterostructures are among the latest advances in FETs. The novelty of these devices arises from the possibility to mechanically stack atomically-thin layers of different

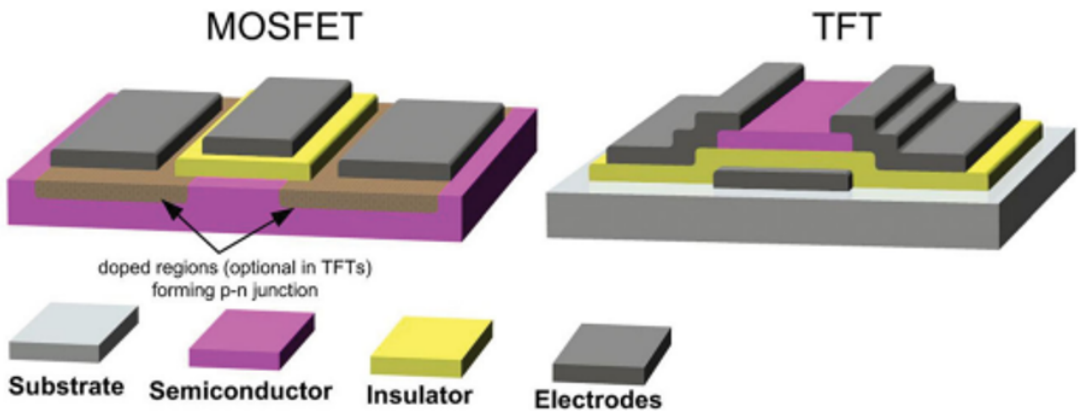

Figure 1.4: Comparison between the typical structures of MOSFETs and TFTs [6].

2D materials. These materials and their heterostructures are at the forefront of scientific research, as they exhibit novel properties which are often very different from their 3D counterparts [7, 8].

1.1.4 Limit of the solid-gating technique

The solid-gating technique is an effective tool to tune the charge doping in low carrier density systems, but usually for high carrier density systems, the generated electric field, and hence the induced charge density, are not high enough to trigger significant changes in the electric transport properties.
The physical limit for the maximum induced charge density is represented by the breakdown electric field: overcoming this limit means, most of the times, the complete failure of the device. Therefore, in a solid gate configuration, the electric field across the insulator cannot exceed 10^8 V/m which corresponds to a maximum surface induced carrier density $n_{2D} \sim 10^{13}$ carriers/cm^2 [9, 10].
Since, basically, the specific capacitance of a solid FET is the one of a parallel plate capacitor - i.e. $C_s = \epsilon_0 \epsilon_r / d$ where d is the distance between the two armatures, ϵ_0 is the vacuum permittivity and ϵ_r is the dielectric relative permittivity - a way to increase the charge doping could be either to increase ϵ_r or to reduce d. High dielectric constant materials (also known as high-κ materials) have been widely investigated by the semiconductor industry but so far no order-of-magnitude improvements have been reached [11]. On the other hand, reducing the oxide thickness, in solid-gating configuration, leads to the decrease of the breakdown voltage and the increase of the gate current due to the tunnel effect that arises when approaching thicknesses of the order of few nanometers.

1.2 The ionic gating

In order to overcome the limitations of standard solid-dielectric gating, an electrochemical cell – which electrolyte could be an ionic liquid (IL) or a polymer electrolyte system (PES) - is incorporated in the FET architecture (see Figure 1.5). By means of this technique, it is possible to generate electric fields as high as $10^9 - 10^{10}$ V/m and induced charge densities of the order of $n_{2D} \simeq 10^{14} - 10^{15}$ cm^{-2}, depending on the properties of the material under investigation [9, 12].

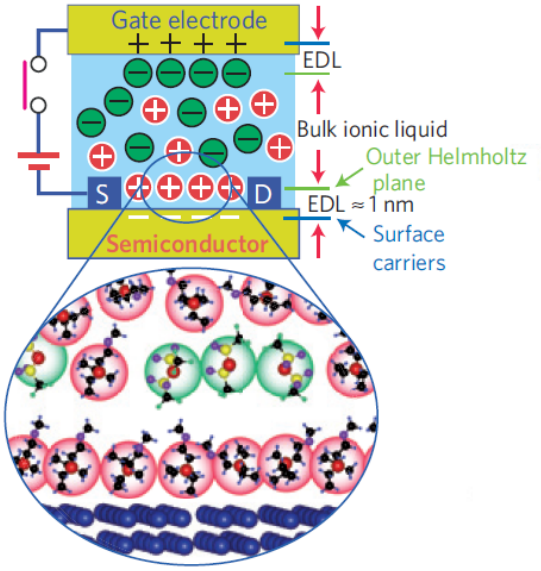

Figure 1.5: Schematic representation of an EDL transistor, with the capacitor-like structure (top) and a magnified view of the EDL formed at the semiconductor interface (bottom). Notice that, upon application of a positive gate voltage at the gate pad, the anions (green circles) move toward the gate electrode and the cations (red circles) move toward the interface with the semiconductor, and, thus, electrons accumulate at the surface of the semiconductor. [Adapted from [12]]

Ionic gating relies on the ion mobility of the electrolyte: when the gate pad is biased, the ions inside the liquid are driven to form an electric double layer (EDL) at the interface with each electrode (refer to Figure 1.5). The structure forming at the interface is also called Helmholtz layer [13]. It is worth to notice that the distance between the ions accumulation layer and the electrode, i.e. the armatures of the effective capacitor that forms at the interfaces, is of the order of the ionic radius and, thus, it is often of the order of the nanometer. Coming back to the specific capacitance of a parallel plate capacitor - $C = \epsilon_0 \epsilon_r / d$ - it is straightforward that the specific capacitance of such devices is extremely high. Coupled with relatively high dielectric constants of the ionic media [14], these systems can reach values in

excess of 10 $\mu F/cm^2$.
Moreover, most of the applied voltage drop occurs within the EDL. As a direct consequence, given a $V_G \simeq 1$ V, the electric field produced at the interface is extremely large (>10 MV/cm or 1 V/nm).
Notice that, differently from the solid-gating technique, in this case no charge carrier can diffuse from one side to the other of the EDL, thus we don't have to care about tunnelling currents or breakdown field as long as electrochemical reactions are not activated at the surface.
However, some drawbacks have to be taken into account when dealing with the ionic-gating technique.
While the solid-gating technique allows to tune the induced charge density at any temperature, the ionic medium undergoes a glass transition that quenches the ion motion. Consequently, it is necessary to heat up the sample above the glass transition temperature of the electrolyte to modify the amount of charge stored in the capacitor. During device operation, the glass transition temperature can be recognized by the drop of the measured gate current under $\simeq 10^{-10}$ A.
Another very important condition for the experimental success of the ionic gating is the mechanical stability of the device. An important cause of device failure is due to mechanical failure of the device due to a mismatch in the thermal expansion coefficients of the electrolyte and the material under study. Device failures can be minimized by reducing the contact angle of the electrolyte on the sample surface, which can be achieved by gently applying a light leaf of inert (e.g. Kapton®) material that squeezes the drop.
Finally, the most critical situations can occur when the gate voltage is large enough compared to the reduction potential of the elecrolyte components to trigger the onset of electrochemical reactions. In these cases, we are no longer in an electrostatic regime and the consequences have to be taken into account specifically. We will discuss this scenario in the next subsection.

1.2.1 Beyond the electrostatic regime

In some cases, the system is intentionally driven out of the electrostatic regime: this is the case of alkali ion intercalation [15–17] or controlled chemical reactions [18–21]. However, in most cases, driving the system outside the electrostatic regime is detrimental to the purpose of the experiment.
The first simple check, that is often sufficient to show that the gate is driven in an electrostatic regime, is the reversibility of the changes in the transport properties upon removal of the gate voltage.
However, there are cases in which this simple check is not enough to guarantee the electrostatic nature of the process. This is the case of a hysteretic behaviour of intercalation in some materials [17], or the permanent modifications that high

electric fields can induce at the material structure even without the rising of electrochemical interactions (eg. The change in oxygen stoichiometry in [18–21]). In general, when electrochemical effects come into play, it is necessary to combine transport measurements with supplementary characterizations (e.g. XPS, XRD, TEM, Raman) in order to exactly determine the nature of the changes in the sample properties.
Finally, the electrochemical regime can also be exploited to perform in-situ nanomachining: like in the remarkable cases of FeSe [22] and $NbSe_2$ [23] thin films where the ionic-gating technique is used to both electrostatically modulate the transport properties and reduce the sample thickness.
In order to maintain the system in the electrostatic regime, it is crucial to investigate the interaction between the electrolyte and the sample. In particular, the right choice of the ionic medium can increase the reduction potential. The reduction potential is the potential energy needed for two chemical reactants to start a redox reaction - being a redox reaction a chemical reaction where two different species exchange charge carriers. The reduction potential depends on the two species involved and, in general, on the temperature. Thus, as long as V_G is lower than this value, one should not incur in electrochemical reactions.
Typically, the electrochemical stability window (i.e. voltage range where no redox reactions occur) varies between 1 and 5-6 Volts for positive and negative values of V_G. Notice that, since cations and anions have in principle different behaviours at the interface with the specimen, the electrochemical stability window is often not symmetric. Moreover, the higher is the temperature at which the gate voltage is applied, the more probable are the reactions to occur, since their occurrence exponentially depend on the temperature. For this reason, the gate voltage is usually applied immediately above the glass temperature, in order to minimize the reactions and maximize the maximum values of V_G that can be safely applied.

1.2.2 The quantum capacitance

As we have seen, the maximum charge density that can be induced via field effect by means of the ionic-gating technique can reach values as high as $10^{14} \div 10^{15}$ cm^{-2} depending on the material under study. There is an intrinsic limitation to this value that depends on the quantum capacitance of the material itself. This is a quantum mechanical property specific for each material.
To better understand where this concept comes from, we can consider first a metallic system under an external electric field: in this system all the external field is screened within a thin surface layer where the carriers accumulate. But, if we consider a very thin material, with a very low density of states (DOS) the field-induced carriers may not be enough to screen out all the external electric field.
This is what S. Luryi formulated while investigating the screening of a two-dimensional

electron gas (2DEG): he demonstrated that this effect can be modelled as an additional capacitance in series to the EDL capacitance, and the expression per unit area is:

$$C_Q = \frac{me^2}{\pi\hbar^2} = \frac{eQ}{E_F} = e^2 DOS(E_F) \tag{1.5}$$

where E_F is the Fermi energy, m is the electron effective mass, e is the electron charge, and Q is the charge per unit area. A schematic representation of Luryi's model is shown in Figure 1.6.
However, in a typical EDL transistor, the bottom plate is the material itself, meaning that we remain with only two capacitances in series and the effective capacitance of the system ($1/C_{eq} = 1/C_Q + 1/C_{EDL}$) is severely limited by the quantum capacitance.

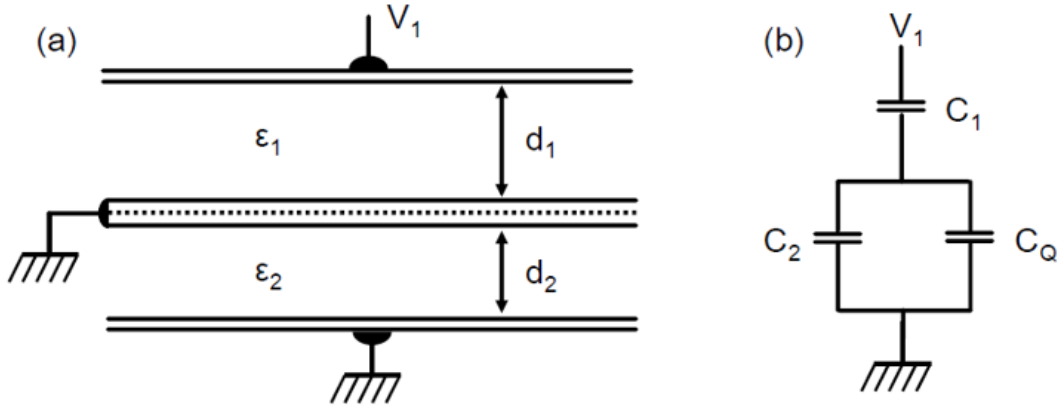

Figure 1.6: a) schematic representation of Luryi's model: the capacitor is biased and the 2DEG layer is grounded. Two dielectric media fill the space between the layers. The electric field is not completely screened by the middle plate. b) circuital representation of a). [Adapted from [24]]

Concluding, we want to stress that the quantum capacitance can often be neglected. It becomes crucial only when it limits the total capacitance. But, for most of the solid-gating architectures and for high DOS materials (like bulk metals), the limitation to the total capacitance comes not from the quantum capacitance.
In conclusion, the quantum capacitance plays a crucial role when either the gating technique has very high specific capacitance or the specimen has low DOS.

1.2.3 Dimensionality of gating

We now discuss whether the changes to the ion-gated material are limited to the surface or involve the whole of the bulk.

The ionic layer at the interface with the gate pad/material under study has a thickness defined by the Debye-Huckel length [25] which means, for a typical electrolyte, of the order of one nanometer.
On the other side of the capacitor, the electronic screening length can range from few Angstroms to several nanometers, depending on the material under study. In metals, the electronic screening length (represented by the Thomas-Fermi length) is smaller than, or of the order of, one atomic diameter. Because of this the charge induction layer is expected to be confined in a surface region of the metallic film which is smaller than the first atomic layer, making the field effect phenomenon almost unobservable for most metallic systems. This is the reason why field-effect experiments on metals have always received little attention [26].
However, in some cases the surface perturbation could affect the bulk of the material if either the sample is thin enough that the screening length is comparable to the thickness, or some coupling phenomenon extends the effective range of the perturbation.
For example, if the total thickness of a superconducting sample is smaller than the coherence length of the Cooper pairs, the surface layer and the bulk are coupled by the proximity effect, and any modification to the surface layer affects the superconductivity also in the bulk of the system [27]. Similar effects can be found in strongly correlated electron systems [28].

1.2.4 Devices preparation

The architecture of most ion-gated field-effect devices is based on a planar geometry where the material under investigation is covered by the electrolyte, which can be either an ionic liquid or a polymer electrolyte system (PES).
A PES can be prepared by mechanically mixing, in inert atmosphere, pondered weights of a structural polymer, an electrolyte (a salt or an ionic liquid) and, if necessary, a diluent and a photo-initiator. The solution is then drop-casted on the surface of the film under test in a dry room (<0.1 ppm H2O) to avoid the moisture absorbed by the polymer lead to a faster degradation of the PES itself. Immediately after drop-casting, the PES is photochemically cured using a medium vapour pressure Hg UV lamp (Helios Italquartz, Italy), with a radiation intensity of 28 mW/cm^2 over the surface of the sample.
The exposition time for the photochemical curing process depends on the particular chemical composition of the PES. Usually the polymerization is performed in two steps of 60-90 seconds: it is preferable to split the process into different steps to avoid overheating the sample.
Figure 1.7 shows two typical measurement configurations. The electrical resistance is measured by a four-probe configuration where the electric contacts are obtained by silver paste spots and micro-diameter gold wires; the electrolyte in which the

EDL is formed is set in between the channel under investigation and the gate pad.

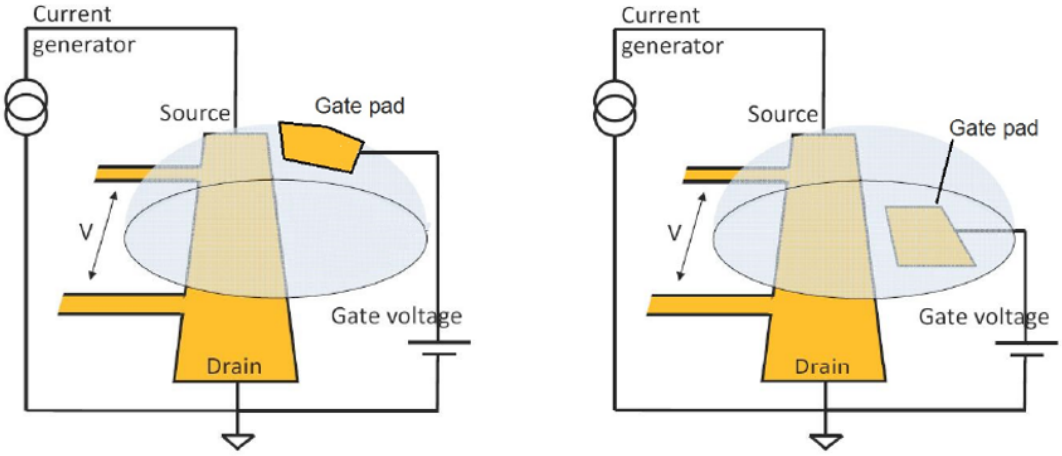

Figure 1.7: Two different architectures adopted for the gate electrodes: a) suspended configuration b) planar or side-gate configuration [Adapted from [24]].

Note that, in these systems, the efficiency of charge accumulation is due to the ionic conduction, and the capacitor is formed at the EDL interfaces (i.e. it does not extend to the whole system). This means that, the top- and side-gate configurations are actually equivalent from the point of view of the carrier accumulation.
A crucial step in the sample preparation is the right choice of the electrolyte. In order to do so, we must consider the chemical and mechanical stability of the electrolyte coupled with the material under study.
Different electrolyte compositions were employed in this Thesis work depending on their chemical and mechanical stability, as well as the requirements of the specific material under study. Concerning the electrochemical stability, we availed ourselves of the expertise of the electrochemistry group of prof. Claudio Gerbaldi of our department.
The mechanical stability, on the other hand, mostly depends on the size of the sample. In very small devices, such as exfoliated devices, the capillary force is sufficient to hold the droplet where drop-casted. However, the typical size of the samples employed in this Thesis work was up to few millimeters: hence, a PES is required, because, after the in situ polymerization, its jelly phase holds the drop attached to the sample and prevents it to drip away.
This solution also works well in the cases in which the sample needs to be held in a vertical position due to experimental constrains.

1.2.5 Double-step Chronocoulometry

A crucial point of a field-effect experiment is to determine the induced carrier density.
Differently from the solid-gating technique, in ion-gated devices the induced charge density does not simply depend on the geometry of the sample and the applied gate voltage.
A typical method employed in the literature to determine the gate-induced charge density is to measure the Hall voltage in the pristine material and as a function of the applied gate voltage. The Hall effect takes place when an electric current flows in a conductive material that is set in a magnetic field: the Lorentz force deflects the trajectory of the electrons along the direction that is perpendicular to the carrier velocity and the magnetic field direction (following the right-hand rule); thus, a voltage drop V_H is generated in that direction.
The Hall voltage V_H is then related to the sheet density n_s of charge carriers in the conductive material by the following equation:

$$n_s = \frac{IB}{e|V_H|} \tag{1.6}$$

where I, B and e are the known values of the electric current, the magnetic field intensity and the elementary charge respectively.

However, this technique is of difficult application in our experiments for a variety of reasons. First, to reliably measure the Hall voltage one requires a precise Hall-bar shaped geometry which requires a further lithographic step that could be either not possible or detrimental for the sample integrity. Second, measuring the Hall coefficient requires the application of a suitably large magnetic field, which is not always achievable in our experimental equipment.
In addition, the Hall effect can be inhibited by the transport properties of the material under study: V_H is often difficult to detect in high-carrier-density conductors, since the Hall signal is inversely proportional to the sheet density n_s of charge carriers; in highly-resistive materials, noise can cover the Hall signal; in granular materials with a hopping transport mechanism the Hall signal is not directly related to n_s [29] – rendering the Hall effect useless for our purpose -; finally, quantum mechanical features, like multi-band or exotic band structures, can increase the complexity of an interpretation of the Hall signal [30, 31].
To overcome all these drawbacks, we employ an electrochemical technique to estimate the total amount of the induced charge density in our devices that is called double-step Chronocoulometry [9, 32]. It is based on the decoupling of the two main contributions to the ionic current inside the electrolyte. When a gate voltage is applied to the gate pad, the ions start to diffuse through the electrolyte and simultaneously they accumulate on the electrodes. This generates two contributions to the gate current: the capacitive current due to the formation of the accumulation

layer at the interface, and the diffusive current due to the ion motion inside the electrolyte.
The diffusive current – or Faradaic current – originates from the two Faraday's laws of electrolysis, that reflect the conservation of mass and charge, and it has the following form:

$$I_d(t) = \frac{nFAD^{\frac{1}{2}}c^*}{\sqrt{\pi t}} \tag{1.7}$$

Where n is the number of electrons, F the Faraday's constant, A the area of the electrode, c^* is the equilibrium concentration and D the diffusion coefficient. By integrating in time the current we obtain a time dependence of the diffusing charge:

$$Q_d(t) = \int_0^t \frac{nFAD^{\frac{1}{2}}c^*}{\sqrt{\pi t}} dt = \frac{2nFAD^{\frac{1}{2}}c^*\sqrt{t}}{\sqrt{\pi}} \tag{1.8}$$

Note that the Faradaic charge is directly proportional to the square root of time while the Faradaic current is inversely proportional to it, and, at t=0, Q_d=0.
The capacitive current, that is due to the formation of the EDL, is the contribution we are interested in. It gives us information about the charge accumulated on the EDL capacitor. The equation that describes the capacitive current in case of a step-like application of a voltage Vg is:

$$I_c = \frac{V_G}{R_s} \exp\left(-\frac{t}{R_s C}\right) \tag{1.9}$$

Where R_s is the ohmic resistance of the electrolyte – that can be $\gtrsim 10^8$ Ω [33] – and C is the effective capacitance of the system. We can recover also in this case the amount of charge involved in the process by simply integrating eq. 1.9:

$$Q_c(t) = \int_0^t \frac{V_G}{R_s} \exp\left(-\frac{t}{R_s C}\right) = V_G C \left(1 - \exp\left(-\frac{t}{R_s C}\right)\right) \tag{1.10}$$

In particular, for $t \to \infty$, $Q_c = V_G C$. Figure 1.8.a shows a qualitative sketch of the behaviour of the two currents and charges involved.
To obtain the induced charge density in the material under study, it is sufficient to determine the value of Q_c. To do this, a first approach is to recover the total charge (i.e. $Q(t) = Q_d(t) + Q_c(t)$) by numerically integrating the measured gate current $I_G(t)$, then rescaling the abscissa to show the total charge as function of the square root of time, and finally fitting the linear region. The intercept of the linear fit with $x = 0$ returns Q_c. The steps of this procedure are summarized in figure 1.8.b.
A second equivalent approach is based on the non-linear fit of the measured gate current via the fitting function $I_G(t) = I_d(t) + I_c(t)$. This method leads to the calculation of Q_c as a fitting parameter equivalent to $V_G \cdot C$. This method is more properly referred to as Chronoamperometry, since it directly studies the current.

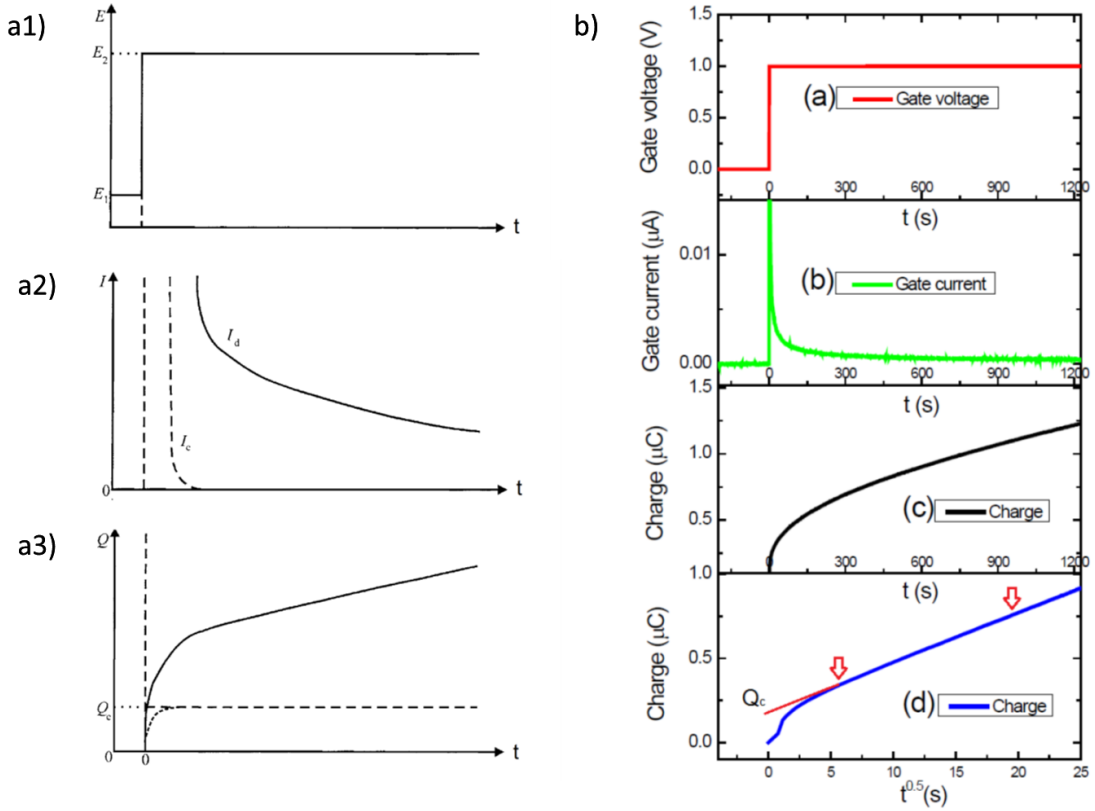

Figure 1.8: (a1) potential step application; (a2) Faradaic current I_d and capacitive current I_c; (a3) diffused (Q_d) and electrical double layer (Q_c) charge. (b) Graphical representation of the Cronocoulometry procedure: (i) a step voltage is applied; (ii) the total gate current is measured; (iii) $Q(t)$ is recovered by integrating the $I_G(t)$; (iv) Rescaling $Q(t)$ as a function of the square root of time, it is possible to fit the linear region for t large enough (the red arrows show the linear fit region); Finally, the intercept of the linear fit returns Q_c. [Adapted from [32] and [24]]

Notice that to implement this method it is crucial to subtract from the measured $I_G(t)$ possible offset currents (I_0) introduced by technical characteristics of the instrumentation.
The same procedures mentioned right now can be applied also to the removal of the gate voltage, when the EDL dissolves and an inverse current is generated. This provides a consistent method to double check the values obtained for the measured Q_c. In this regard, notice that it is necessary to subtract the residual diffusion current due to the charging process when applying the chronoamperometry procedure to the discharging process.
For completeness, the parametrical functions used in the chronoamperometry are

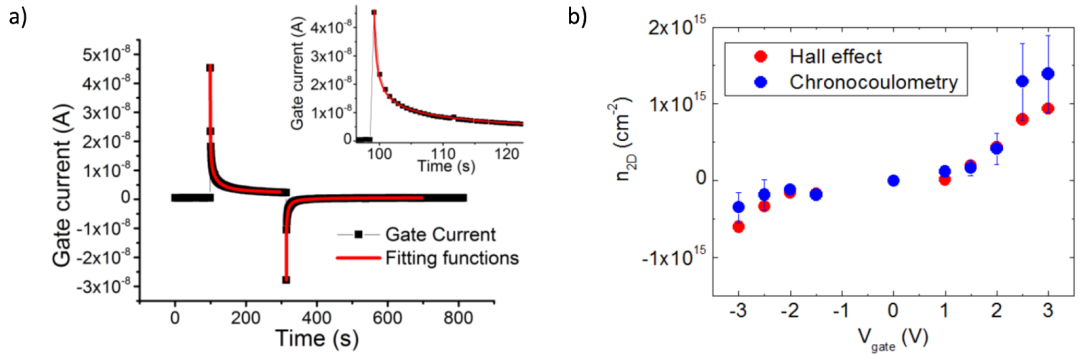

Figure 1.9: (a) Fit of the gate current I_G in the charge and discharge processes by means of the chronoamperometry method. The inset shows the good agreement between the fitting function and the experimental data for low values of $t - t_0$. (b) Simultaneous measurements of induced charge densities via Hall effect (red dots) and by DSCC (blue dots) [24].

the following:

$$I_{G,charge} = I_0 + \frac{A}{\sqrt{t - t_0}} + B \exp\left(-\frac{t - t_0}{C}\right) \tag{1.11}$$

$$I_{G,discharge} = I_0 + A\left(\frac{1}{\sqrt{t - t_1}} - \frac{1}{\sqrt{t - t_0}}\right) + B \exp\left(-\frac{t - t_1}{C}\right) \tag{1.12}$$

Where t_0 and t_1 are the times where the gate voltage is applied and removed respectively, while A, B and C are parameters related to the quantities seen before. Finally we notice that it has been proven that the induced charge densities measured via the Hall effect match with the Double Step Chronocoulometry (DSCC) ones (see figure 1.9.b [24]).

1.3 The ferroelectric gating

Certain materials show a spontaneous electric polarization, i.e. a not null electric dipole moment, even without the application of an external electric field that can be tuned by an external electric field. These materials are referred to as ferroelectrics, in analogy with the ferromagnetic materials that show a spontaneous magnetization.
The first material discovered that showed ferroelectricity is the Rochelle salt, i.e. potassium sodium tartrate tetrahydrate (chemical formula: $KNaC_4H_4O_6 \cdot 4H_2O$) in 1920. This double salt was invented in 1665 by Pierre Seignette at La Rochelle, France, and at that time was already used in medicine. Two centuries later, it led to

the discovery of pyroelectricity and the first systematic studies on piezoelectricity. Nowadays, this does not sound as a coincidence: it has been found that every ferroelectric material also shows pyroelectricity and piezoelectricity, and their crystal structure is non centrosymmetric.
Pyroelectricity is the property of generating a temporary voltage when the material is heated or cooled, while piezoelectricity instead is the ability of generating a voltage when stressed or strained. Piezoelectric properties work also inversely (i.e. when a voltage is applied to a piezoelectric, it shows stress or strain).

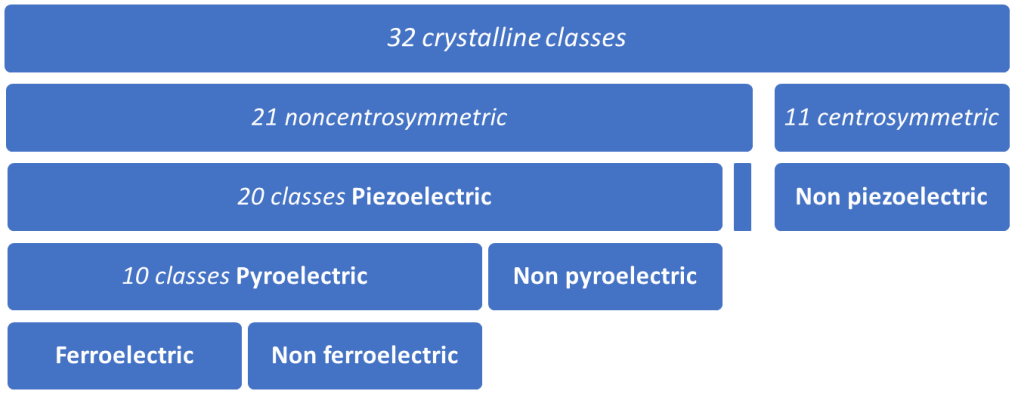

Figure 1.10: Crystalline structures that show piezo- pyro- and ferro-electricity. Crystals can be found in 32 different crystalline classes. Excluding 11 centrosymmetric classes, 20 of the remaining 21 show piezoelectricity. 10 of these show spontaneous polarization with temperature changing, therefore they are called pyroelectric. Ferroelectrics are a subset of pyroelectric materials, implying that every ferroelectric crystal is also pyroelectric and piezoelectric.

Because of their properties, ferroelectric materials are massively used in a disparate variety of applications. For example, ferroelectrics can be used to build capacitors with tunable capacitance. The architecture of these devices resembles again that of the MOSFET, but now the dielectric is substituted by a ferroelectric material. It is noteworthy that the permittivity of such materials is often very high, allowing to reach very good capacitances.
Most importantly, the polarization of a ferroelectric present an hysteresis loop, and a remnant polarization: this means that even when the external electric field returns to zero, the ferroelectric is still polarized. This property allows to make ferroelectric memories like RAM for computers or radio-frequency identification (RFID) cards. The combination of memory, piezoelectric and pyroelectric effects allows also to use ferroelectric materials also for sensor application. Ultrasound-based medical equipment, infrared cameras, fire sensors, sonar, vibration sensors, fuel injectors in diesel engines are only a few of the applications of these materials.
Nowadays, after almost one century from the discovery of ferroelectricity, ferroelectrics are growing in popularity also because of their perspectives to be used

as non-volatile random-access memories (NVRAM). Indeed, semiconductor-based devices cannot be miniaturized further without facing huge costs for the semiconducting industry [34], while ferroelectric-based FETs show perspectives that they could go beyond these limits.

1.3.1 The piezoelectric effect

An exhaustive approach to the piezoelectric linear behaviour is provided in Ref. [35]. In this approach (i) mechanical and electrical dissipation are not considered; (ii) elastic, dielectric and piezoelectric coefficients are considered as constants upon variation of magnitude and frequencies of mechanical and electrical forces. This is due to the fact that it is not possible to establish a standard approach to piezoelectric materials including those aspects, and, even though real materials are affected by non-linear behaviour as well as finite mechanical and electrical dissipation, this approximation helps to figure out the elements that play a role in the piezoelectric effect.
So, under these conditions, the electric displacement D (3×1 vector, with dimensions Coulomb/m^2) and the strain ϵ (6×1 vector, dimensionless) can be written in a tensor form as functions of the applied electric field E (3×1, Volt/m) and the applied stress σ_m (6×1, N/m^2) as:

$$D_i = e^{\sigma}_{ij} E_j + d^{d}_{im} \sigma_m \tag{1.13}$$

$$\epsilon_k = d^{c}_{jk} E_j + s^{E}_{km} \sigma_m \tag{1.14}$$

The other quantities involved are piezoelectric constants: the dielectric permittivity e^{σ}_{ij} (3×3, F/m), the direct d^{d}_{im} (3×6, C/N or m/V) and converse d^{c}_{jk} (6×3, C/N or m/V) piezoelectric coefficients, and the elastic compliance s^{E}_{km} (6×6, m^2/N).
To better understand, consider the case of a sheet of piezoelectric polarized along the out-of-plane direction (say, polarized along the $\hat{z}$ direction, being $\hat{x}$, $\hat{y}$ and $\hat{z}$ the orthonormal unit vectors of the canonical Cartesian space).
The piezoelectric coefficients d^{c}_{jk}, that define the strain per unit field at constant stress in the converse piezoelectric effect, can be expressed by the matrix:

$$d = \begin{pmatrix} 0 & 0 & d_{31} \\ 0 & 0 & d_{32} \\ 0 & 0 & d_{33} \\ 0 & d_{24} & 0 \\ d_{15} & 0 & 0 \\ 0 & 0 & 0 \end{pmatrix} \tag{1.15}$$

The coefficients d_{31}, d_{32} and d_{33} express the normal components of the strain upon the application of an electric field along the $\hat{c}$ direction, while d_{15} (d_{24}) expresses

the shear strain in the 1-3 (2-3) plane for the field E_1 (E_2) applied along the 1-axis (2-axis). Even though the two matrices d^d_{im} and d^c_{jk} in principle describe two different behaviours, in practice the coefficients are equivalent [36] but the matrices are one the transposed form of the other. For completeness, explicit forms of the compliance matrix S^E and the permittivity matrix e^σ are [36]:

$$S^E = \begin{pmatrix} S_{11} & S_{12} & S_{13} & 0 & 0 & 0 \\ S_{21} & S_{22} & S_{23} & 0 & 0 & 0 \\ S_{31} & S_{32} & S_{33} & 0 & 0 & 0 \\ 0 & 0 & 0 & S_{44} & 0 & 0 \\ 0 & 0 & 0 & 0 & S_{55} & 0 \\ 0 & 0 & 0 & 0 & 0 & S_{66} \end{pmatrix} \tag{1.16}$$

$$e^\sigma = \begin{pmatrix} e^\sigma_{11} & 0 & 0 \\ 0 & e^\sigma_{22} & 0 \\ 0 & 0 & e^\sigma_{33} \end{pmatrix} \tag{1.17}$$

Equation 1.13 expresses the direct piezoelectric effect, i.e. an electric displacement appears under the application of an external stress. The generated charge is thus recovered by:

$$q = \int\int \begin{pmatrix} D_1 & D_2 & D_3 \end{pmatrix} \begin{pmatrix} dA_1 \\ dA_2 \\ dA_3 \end{pmatrix} \tag{1.18}$$

where dA_1, dA_2 and dA_3 are the infinitesimal components of the electrode areas orthogonal to the 1-axis, 2-axis and 3-axis respectively. The relation between the generated charge and voltage across the sensors is defined by

$$V_c = q/C_p \tag{1.19}$$

where C_p is the capacitance of the sensor.

1.3.2 The ferroelectric phase transition

As we have already introduced, the unicity of ferroelectric materials relies on the possibility to permanently change their electric polarization under the application of an external electric field [37].
A first macroscopic theory that addresses the behaviour of the polarization in response to an external electric field is the Landau-Devonshire theory [38]. It takes the moves from the famous Landau theory about phase transitions [39] which shows that when a phase transition is associated to a symmetry change, it must occur accompanied with abrupt changes. The quantity that changes its symmetry is considered as the order parameter of a macroscopic approach: when the symmetry is at its maximum, the order parameter is zero over the whole system. For this reason,

Landau's approach is well designed for long-range interaction phase transitions like the superconducting and the ferroelectric ones.
It is worth noticing that Landau theory offers a feasible background to ferromagnetism too. However, unlike the great similarity between polarization and magnetization, electric dipoles are far more (i.e. 137^2 times) energetic than magnetic dipoles (both considered at the Bohr-radius scale) [38] and, thus, electric dipoles interactions have a longer range then their magnetic counterpart, that can be considered short-ranged. This marks a deep difference between the Landau theory for ferromagnetic and ferroelectric materials.
As far as our subject is concerned, Devonshire developed a phenomenological treatment to write the free energy in ferroelectric systems [40–42]. For a bulk ferroelectric system to be fully thermodynamically described, the variables involved are the temperature (T), the polarization (P), the strain (η), the electric field (E) and the stress (σ). Being the latter two externally controlled, we can consider P and η as dependent variables related to the "internal" state of the system. This suggests, and it is also a fundamental postulate of thermodynamics in crystals, that the free energy can be written as function of only two of the four mentioned quantities [40]. Moreover, since the order parameter we are interested in is the polarization of the system, we can choose to express the thermodynamic state of the ferroelectric as a function of P and, for example, σ, for a total of 10 variable components: three for P, 6 for the stress tensor and one is the temperature.
Here we don't want to give a complete treatment of the theory, but, instead, we are more interested in giving a flavour of where the macroscopic effects that we register on a ferroelectric are originated. To do this, it is not strictly necessary to continue having all the complete set of variables. We can restrict out treatment to the case of an uniaxial polarization when no external stress is applied. In this case, the free energy density per unit volume can be expandend in series and it takes the following form:

$$\mathcal{F}_P = \frac{1}{2}aP^2 + \frac{1}{4}bP^4 + \frac{1}{6}cP^6 - EP \tag{1.20}$$

The series is truncated at the power-six term, and a, b and c are generic coefficients. The equation can be differentiated to show that the minimum of $\mathcal{F}_P$ gives a relation between P and E:

$$E = aP + bP^3 + cP^5 \tag{1.21}$$

From which we can find an expression for the dielectric susceptibility χ:

$$\chi = \frac{P}{E} = \frac{1}{a} \tag{1.22}$$

In ferroelectrics, the susceptibility is expressed by the Curie-Weiss law:

$$\chi = \frac{a_0}{T - T_0} \tag{1.23}$$

where a_0 is the Curie constant and is related to the material characteristics, and T_0 is the Curie temperature. Hence:

$$a = a_0(T - T_0) \tag{1.24}$$

We can rewrite $\mathcal{F}_P$ with the explicit dependence on T:

$$\mathcal{F}_P = \frac{1}{2}a_0(T - T_0)P^2 + \frac{1}{4}bP^4 + \frac{1}{6}cP^6 - EP \tag{1.25}$$

where a_0 and c are found positive in all known ferroelectrics [38].

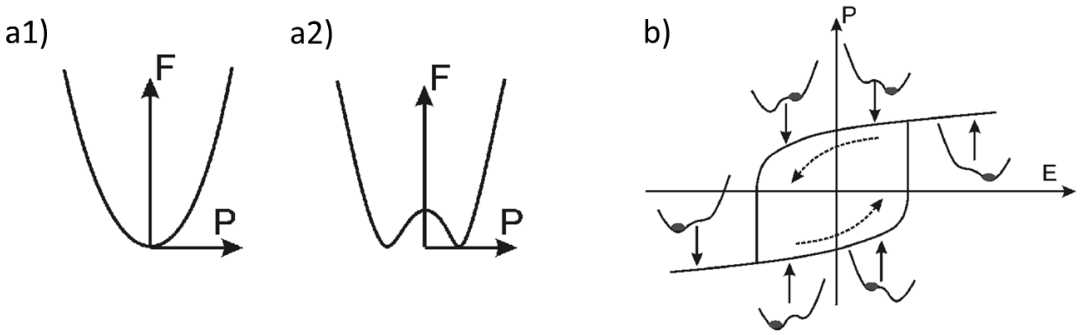

Figure 1.11: (a) Free energy for (a1) $T >> T_0$ and (a2) $T << T_0$. (b) The ferroelectric hysteresis loop of an ideal ferroelectric material (adapted from [38])

Figure 1.11.a shows the free energy (i.e. $\int \mathcal{F}_P \, dV$) as function of the polarization P in the limits for $T >> T_0$ and $T << T_0$ resulting in the two cases of a paraelectric and a ferroelectric material.
It can be easily verified that, by setting $E = 0$ and by considering only the first two terms of eq. 1.25, it is possible to define the value of the spontaneous polarization of the system as:

$$P_0 = \frac{a_0}{b}(T_0 - T)^{\frac{1}{2}} \tag{1.26}$$

However, if $b < 0$, we cannot retain only the first two terms, and the transition between the paraelectric and the ferroelectric phase shows a discontinuity [38]. Though, it is still possible to state that, for $T < T_0$, the free energy shows two minima that corresponds to the two spontaneous polarization states of the ferroelectric phase. Moreover, the application of an external electric field tilts the curve rendering one of the two minima convenient with respect to the other. Following these last considerations, figure 1.11.b gives the correct idea of what is the origin of the hysteretic behaviour of the polarization as function of the electric field, and we will see shortly the experimental evidences of this phenomenon.

1.3.3 The ferroelectric phase transition

From an experimental point of view, in order to measure the polarization of a ferroelectric material it is necessary to know the various contributions to the electrical displacement that are measured when performing such experiments. Proper $D-E$ loops are obtained by supplying an AC voltage across the ferroelectric material under investigation and by measuring the current that flows across the material under these conditions. The displacement D is recovered by the integration of such current and then by dividing it by the electrodes area [37].
Independently from the AC input signal profile, the electric displacement has different contributions. In general, apart from the polarization contribution we are interested in, there is a contribution due to the electrical conductivity, and another contribution arises from the capacitive current typical of such parallel-plate-capacitor–like devices. So, in an ideal experiment where a ferroelectric sheet is sandwiched between two electrodes, the electrical displacement is given by:

$$D = \epsilon_r \epsilon_0 E + P + \int \sigma E \tag{1.27}$$

where the first term arises from the capacitive dielectric contribution, the second is due to the domain switching, and the third takes into account the ohmic contribution to the overall current that is measured across the device (σ is the conductivity of the piezoelectric material).
In some cases, like that of our experimental setup, the electromagnetic coupling of the wiring could give rise to additional contributions to the current that have to be decoupled from the meaningful signal. In our setup we overcame this issue by performing the same experiments with and without the sample mounted: the difference in the signal is due to the contribution of the device. Moreover, dealing with small currents (of the order of $1 \div 50$ nA) that have to be integrated in long time periods (from few to several minutes), even a small amount of offset current due to the instrumental error, could lead to noticeable differences on the measured values. For this reason, another correction that has to be made to the raw data is the subtraction of this contribution before integrating the measured current.
To better understand the three different contributions to the electric displacement, referring to [37], we will briefly introduce the characteristic I-E and D-E loops for three different materials: the first material is Al_2O_3 and its high electrical resistivity ($> 10^{15} \Omega cm$) makes the contribution of dielectric permittivity dominant; the second is a multiferroic $Bi_{0.89}La_{0.05}Tb_{0.06}FeO_3$ (BLFO) ceramic where the dominant term is the electric conductivity; finally, we will present the $Na_{0.5}K_{0.5}NbO_3$ (sintered at 850° C; NKN850) ceramic case, where the dominant contribution is the polarization of the ferroelectric.
We will examine the response of all the three different materials upon the application of a triangular voltage waveform.

The contribution of dielectric permittivity The Al_2O_3 case is reported in 1.12.a and 1.12.b. The contribution to the current I is:

$$I = \frac{dQ}{dt} = \frac{d}{dt}(CV) = \frac{d}{dt}(\frac{\epsilon AEs}{s}))\frac{d}{dt}(\epsilon AE) = \epsilon A\dot{E} \tag{1.28}$$

where Q is the electric charge, C is the capacitance, V is the voltage, E is the electric field, s is the sample thickness, ϵ is the dielectric permittivity, A is the sample area and t is the time.
Since the input signal is a triangular waveform, the current in such a material is expected to be constant, positive or negative, depending on the gradient of the input signal variation.
The D dependence on E is clearly linear, since the main contribution to D is due to $\epsilon_r\epsilon_0 E$.

The contribution of electric conductivity In BLFO ceramics, the main contribution is due to electrical conductivity. This leads to the I-E and D-E loops showed in 1.12.c and 1.12.d. Here the current depends linearly on E as:

$$I = \frac{V}{R} = \frac{Es}{R} = \frac{EA}{\rho} \tag{1.29}$$

where R is the resistance and ρ is the resistivity. And the D-E loop (obtained as $\int I/Adt$) has an eye-like shape.

The contribution of ferroelectric polarization Figures 1.12.e and 1.12.f finally show the I-E and D-E loops respectively of NKN850 ceramics. It is clearly evident where the polarization occurs with increasing (or decreasing) of the current at a certain value of E. The hysteresis loop is clearly evident as well.
The value of D when $E = 0$ is called the remnant polarization P_r: in principle, the values for the positive and negative polarizations are not equal in absolute value. The electric field where the current reaches its peak is called coercive field E_c.
Finally, the polarization loop is strongly dependent on the input triangular voltage waveform frequency and on the temperature at which the experiment is performed, as we have seen in the previous section.
In our ferroelectric-gating experiments, the polarization contribution is the most relevant one, since it is the amount of charge that is driven to the surface of the capacitor. We will see in Chapter 5 that the induced charge densities due to ferroelectric polarization can reach 10^{14} e^-/cm^2, a value that is very high when compared with standard solid-gating devices, and that allows to investigate materials that could otherwise be damaged by electrochemical interactions in ion-gated devices.

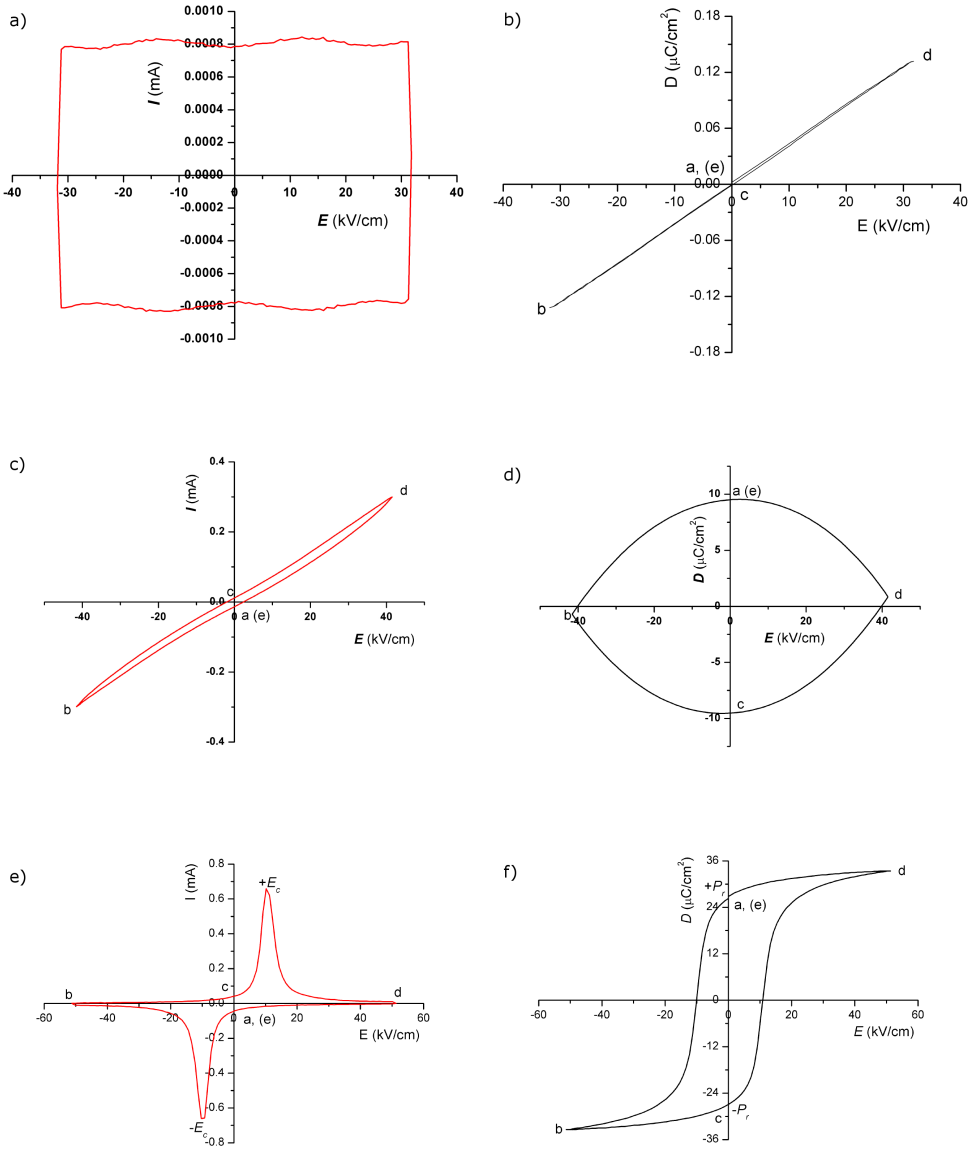

Figure 1.12: Current – Electric field ($I-E$) and electric displacement – electric field ($D-E$) loops measurements for Al_2O_3 (a and b), BLFO (c and d) and NKN850 (e and f) ceramics. Measurement on Al_2O_3 were performed at 10 Hz and 25 ° C; measurement on BLFO were performed at 20 Hz and 25° C; measurement on NKN850 were performed at 1 Hz and 25° C. (Adapted from [37]).

1.3.4 The strain loop

When an electric field is applied to a sheet of ferroelectric material, due to the fact that the ferroelectrics always are also piezoelectrics, the piezoelectric effect results in a strain of the sheet itself. We have already seen the response of the strain to the application of an external electric field E in eq. 1.14: the strain is linear with E. Often, we are interested in the response in the longitudinal and the latitudinal directions of a piezoelectric sheet to an out-of-plane E application. In this case, eq. 1.14 can be written as:

$$S = d_{33}E \tag{1.30}$$

where S represents the in-plane strain and E is the out-of-plane applied electric field.
However, the measured strain typically shows a peculiar behaviour that is well known as the S-E butterfly loop (see figure 1.13) where the measured strain S along a certain direction is plotted as function of E.

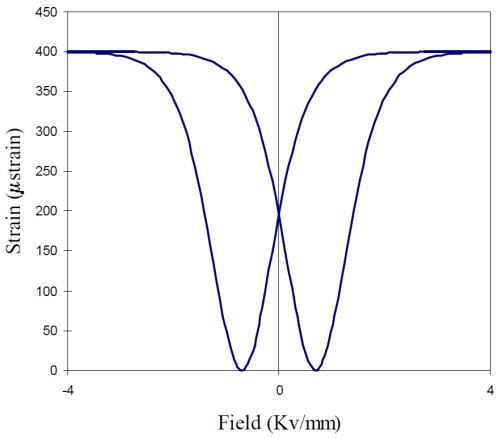

Figure 1.13: Schematic representation of a (S-E) butterfly loop. (Adapted from [43]).

In particular, frequently but not always, the S-E loop is proportional to the square of the P-E loop [43].
The difference between the linear and non-linear regimes depend on the applied E range: in an E applicative range between the saturation and the repolarization of the ferroelectric, the strain S is linear with E; with exceeding the saturation E, or with undergoing repolarization, we activate the non-linear behaviour. Moreover, to use piezoelectric materials as actuators, it is always preferable not to undergo repolarization that can cause fast degradation due to fatigue and difficulties to control [44].

In general, an hysteretic behaviour is always due to the presence of dissipative effects. It is possible to arrange the experimental setup in order to recover the anhysteretic D-E and S-E loops. For example, it is possible to drive an AC current with reduced amplitude at each cycle such that it indefinitely approaches a finite value [45]:

$$E(t) = E_{max} sin(\omega t) exp(-k\omega t) + E_{bias}[1 - exp(-k\omega t)] \tag{1.31}$$

It is possible to perform such a measurement for different values ofE_{bias}. Doing so, we obtain a $D(E_{bias})$ curve that is independent from the hysteresis.
Similarly, it is possible to perform simultaneous anhysteretic measurements for the S-E loop.
The importance of such a measurement technique relies on the fact that it is possible to construct a one-to-one relation between the applied field and the expected P and S. For most of our purposes, it is of utmost importance to decouple the ferroelectric and piezoelectric effects in order to address the measured changes in the transport properties of our samples to the right effect.

Chapter 2

Ionic gating in $BaFe_2(As_{1-x}P_x)_2$ superconducting thin films

2.1 Introduction:

Iron-based superconductors (IBSCs) are one of the most recently discovered superconductor classes. In 2006 low temperature superconductivity was discovered by Kamihara *et al.* [46] in F-doped LaFeAsO, by partial substitution of oxygen atoms with fluorine atoms, and in 2008, in the same compound and by the same group headed by Hosono, high temperature superconductivity was discovered reaching a T_c of 26 K for an optimal value of the F-doping [47] (i.e. $LaFeAs(O_{0.89}F_{0.11})$. The discovery of a new class of high temperature superconductors rekindled the interest of the scientific community so diffusively that, within two years, more than 200 species of iron-based superconductors were discovered [48].

2.1.1 The crystallographic structure

IBSCs present a layered structure made of FeX layers (where Fe is iron and X is either a pnictogen or a chalcogen) with a tetragonal structure at ambient conditions, most of the times alternated with a non-conducting layer, stacked along the c axis.
Figure 2.1 shows the most common lattice structures reported so far for IBSCs parent compounds (i.e. the compounds from which the IBSCs are derived by means of doping).
The first structure to be discovered was the *Re*FeAsO (where *Re* is a rare earth metal) and it is commonly known as the "1111" structure. Together with the "122" structure, it is the most studied structure. Compounds of the form AFe_2As_2 (where A is an alkali or rare earth metal) belong to the "122" structure. In FeSe the conductive layer is made of iron and a chalcogen: it is a typical example of the "11"

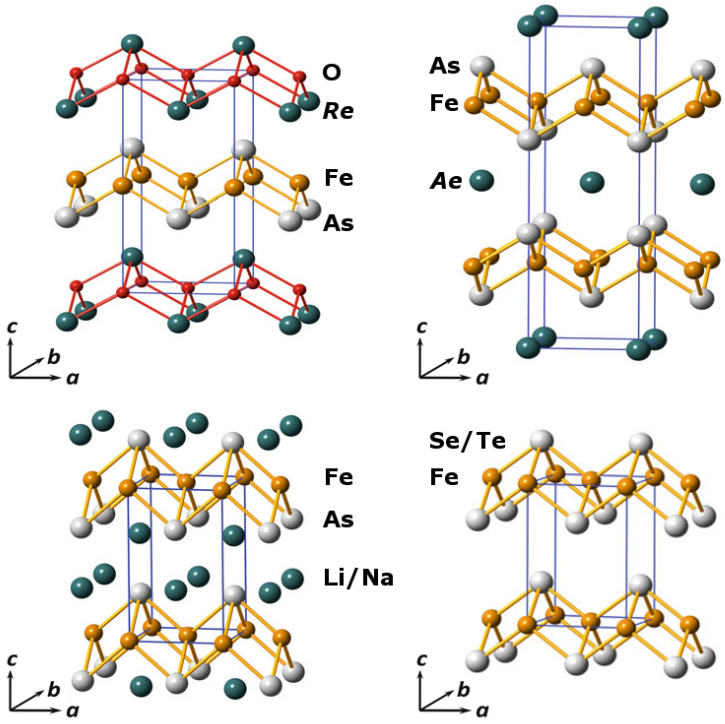

Figure 2.1: The most common crystallographic structures for IBSCs parent compounds. On the top-left corner there is the "1111" structure; on the top-right the "122"; on the bottom-left the "111"; on the bottom-right the "11". (adapted from Ref. [49]).

structure.
The layered structure is a feature that IBSCs share with cuprates. We will see in the following that it is not the only one. Among cuprates, it seems to be a tendency that the larger is the distance between two CuO_2 planes, the higher is T_c. Even though this correlation is far from being stringent, nevertheless, it encouraged researcher to build iron-based compounds with multi-layers inserted between two adjacent FeX layers. This led to very complicated structures. As an example, Ogino *et al.* reported superconductivity at temperatures higher than 40 K on $(Fe_2As_2)(Ca_m(\alpha,Ti)_nO_y)$ (with m,n integer numbers properly chosen and α = Al, Mg, Sc) with extremely thick blocking layers [50–52].

2.1.2 Doping of the parent compounds

Most of the parent compounds of each IBSC species at ambient pressure and native charge density do not show superconducting properties. Superconductivity

emerges when doping is introduced. Typically, there are four methods to induce superconductivity in a parent compound: the chemical charge doping, the chemical pressure doping, the electric-field-induced charge doping and the externally-applied pressure doping.
The chemical charge doping consists of a chemical substitution of an atomic species in a parent compound with another atomic species with different number of electrons in its external orbitals, thus leading to a change in the carrier density of the system. In particular, the change in the charge density affects the conductive layer, where charges are free to move, which accepts or donates electrons, and thus, leading to a change in the transport properties of the material. $Re\mathrm{FeAsO}_{1-x}(\mathrm{F/H})_x$ (with Re = rare-earth metals like La, Ce, Sm and Gd), $(\mathrm{Ba}_{1-x}\mathrm{K}_x)\mathrm{Fe}_2\mathrm{As2}$, and oxygen vacancies are some examples of this kind [53].
A particular mention is for $\mathrm{Ba}(\mathrm{Fe}_{1-x}\mathrm{Co}_x)_2\mathrm{As}_2$. In fact, in this case, Fe^{2+} and Co^{2+} ions have the same valence in the bonding but they belong to different atomic groups, thus introducing a change in the carrier density. Moreover, the peculiarity of this substitution is that Co atoms directly replace Fe atoms where the superconductivity emerges: it is called "direct doping".
Another effective method to induce superconductivity in a layered iron-based conductor is the chemical substitution of an atomic species with another of the same atomic group, thus leaving the carrier density unchanged but introducing a strain in the lattice that acts like an effective pressure doping. This is the case of $\mathrm{BaFe}_2(\mathrm{As}_{1-x}\mathrm{P}_x)$ and $\mathrm{FeSe}_{1-x}\mathrm{Te}_x$ [54, 55].
As mentioned in the previous chapter, external electric field applied by means of ionic gating can control the superconducting transition in FeSe [22, 56–58] and $\mathrm{FeSe}_{0.8}\mathrm{Te}_{0.2}$ [59].
Intercalation with small alkali atoms (like Li or Na) or groups (NH^+) are used to induce superconductivity by changing the interlayer spacing [53]. A very interesting case is the $\mathrm{H_2O}$ intercalation in $\mathrm{SrFe_2As_2}$ [60]: in this unique case, superconductivity is induced in the parent compound when the material is left in ambient conditions.
External pressure, combined with chemical doping, contributes to tune T_c. Optimally doped LaFeAsO reaches the maximum $T_c = 43$ K at 4 GPa [61].
Nowadays, the record T_c for bulk iron-based superconductors is 58.1 K, reached in the $\mathrm{SmFeAsO}_{0.84}\mathrm{F}_{0.16}$ [62].

2.1.3 The electronic structure

Theoretical calculations have been performed to investigate the electronic properties of IBSCs parent compounds.
Figure 2.2a presents the Fermi surfaces of LaFePO, the first investigated compound. There are illustrated the five sheets of the folded Fermi surfaces that originates from the Fe 3d orbital. Among the five different sheets, the two cylinders located at the

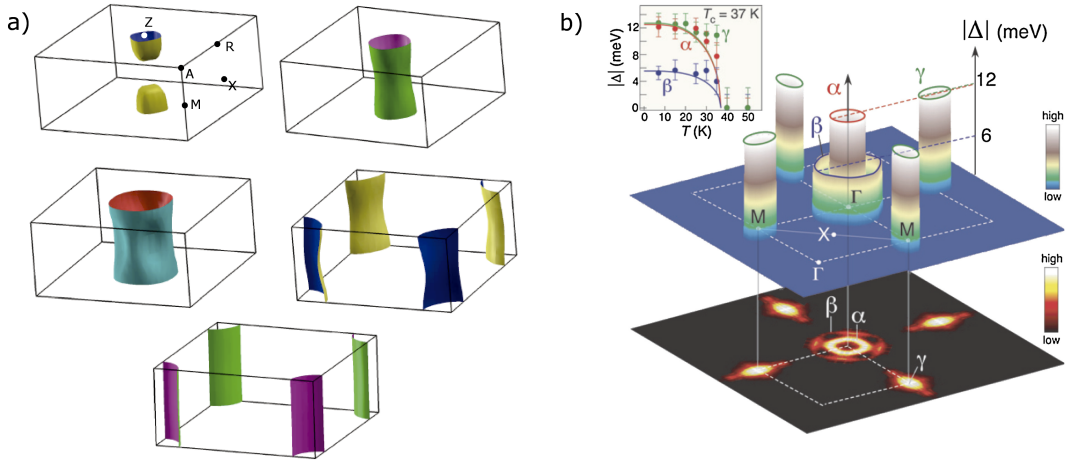

Figure 2.2: a) Band structure of LaFeOP. (adapted from Ref. [63]). b) Three-dimensional representation of the ARPES measurements on $Ba_{0.6}K_{0.4}Fe_2As_2$ at T = 15 K; in the inset, temperature dependence of the superconductive gaps (adapted from Ref. [64]).

centre of the Brillouin zone are holonic, while the two at the edge are electronic. A small hole pocket is centred in Z [63]. Experiments confirmed the theoretical predictions [65, 66]. Very similar results have been obtained for LaFeAsO [67]. In $BaFe_2As_2$ the concentric cylinders are strongly nested, giving rise to stripe-like spin-density-waves (SDW) [68].
In conclusion, the electronic structure of IBSCs is absolutely multiband.
The multiband electronic structure results in a multi-gap nature of the superconductive state. Ding *et al.* investigated the superconductive gap of $Ba_{0.6}K_{0.4}Fe_2As_2$ at T = 15 K by means of ARPES measurements (the results are shown in figure 2.2b). A larger gap ($\Delta \sim 12$ meV) corresponds to the small hole-like Fermi-surface sheet and the electron-like one; a smaller gap ($\Delta \sim 6$ meV) is measured for the larger hole-like Fermi-surface sheet. The two gaps close at the same temperature (i.e. T_c = 37 K).
Experiments were performed on IBSCs in order to measure their resistivity. The parent compounds of IBSCs are conductive and the conduction occurs in the iron-containing layer. This brings to a deep difference in the transport properties with respect to cuprates, where the CuO_2 layer is insulating. With the introduction of substitutional atoms in the parent compounds, the transport properties change deeply. As an example, figure 2.3a shows the resistivity measurements of $(Ba_{1-x}K_x)Fe_2As_2$ for x = 0, 0.4, 1.0 [69]. The parent compound is the most resistive of the three. A clear evidence of superconductivity appears for x=0.4, with T_c=38K. Moreover, Ba-122 shows a clear evidence of a phase transition at 140K. In

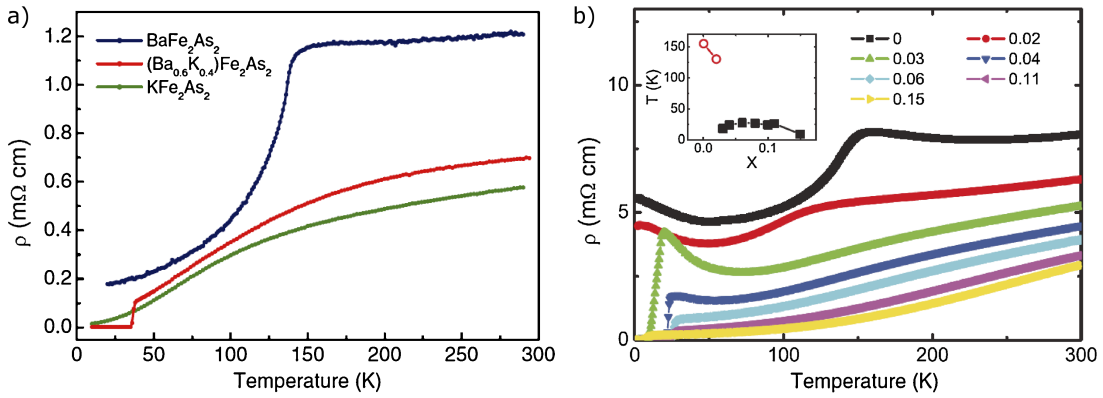

Figure 2.3: Electrical resistivity as function of temperature of (a) $(Ba_{1-x}K_x)Fe_2As_2$ for x = 0, 0.4, 1.0 (adapted from [69]) and (b) $LaFeAs(O_{1-x}F_x)$ for x = 0, 0.02, 0.03, 0.04, 0.06, 0.11, 0.15. In the inset of (b), the phase diagram reporting the temperatures of the resistivity anomalies (red empty circles) and the superconductive critical temperature (black filled squares) as function of the fluorine level of doping (adapted from [70]).

turn, it was demonstrated that a structural tetragonal-to-orthorhombic structural transition and a paramagnetic-to-antiferromagnetic phase transition occur simultaneously at that temperature [48]. We also notice that, for $x = 0.4$ there is no sign of such a phase transition.
Similar studies have been reported for $LaFeAs(O_{1-x}F_x)$ for different values of x (see figure 2.3b). It is clear that the phase transitions temperatures depend on the fluorine content, and the critical temperature too. In this particular case, the structural and magnetic phase transitions happen at two different temperatures [48].
The presence of a magnetic ordering is another main characteristic shared between cuprates and IBSCs. Before the discovery of superconductivity in cuprates, it was a common belief, among scientists, that a magnetic ordering would compete with the formation of Cooper pairs. And this fact remains true: in fact, superconductivity, in cuprates as well as in IBSCs, emerges only when the magnetic ordering is partially or totally suppressed.
In conclusion, an antiferromagnetic phase (AFM) appears in IBSC parent compounds when reaching low temperatures. Its appearance is accompanied with a structural phase transition from tetragonal to orthorhombic crystal structure. Moreover, depending on the doping concentration, a superconductive dome comes out. The phase diagram of an H-doped Sm-1111 and a Co-doped Sm-1111 are represented in figure 2.4.
Very often, more than one doping methods act simultaneously on the system. It can

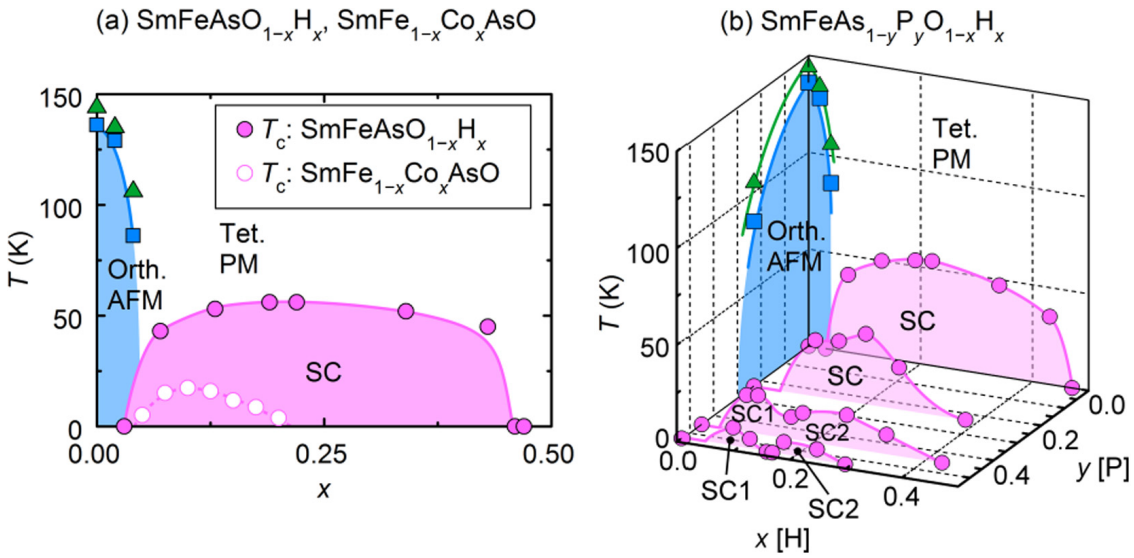

Figure 2.4: Phase diagram of (a) an H-doped Sm-1111 and a Co-doped Sm-1111 and (b) $SmFeAs_{1-y}P_yO_{1-x}H_x$ (adapted from Ref. [53]).

result from a variety of scenarios: when a parent compound is doped with two different atomic species; when the dopant atom introduces additional charge density and is also appreciably different in size from the substituted species, thus introducing strain in the system; when pressure or electric field are externally applied in a chemically doped system; when a doped compound is grown on a substrate with different atomic spacing. It is possible to represent this situation in a phase diagram that takes into account each contribution on different, orthogonal axis, if it is possible to decouple them.
Notice that, as it is for cuprates, the introduction of impurities in the superconducting layers sharply affects the superconducting properties. However, in IBSCs, superconductivity seems to be more robust with respect to cuprates [53]. This fact, jointly with the high upper critical magnetic fields (as high as 50 T [53]), makes IBSCs good candidates for applications from wires and tapes to superconducting bulk magnets.

2.1.4 The Ba-122 family

Among the IBSC class, $BaFe_2As_2$ is one of the most studied family thanks to the purity of the fabricated samples and the ease of production reached for the fabrication process, both for single crystals and thin films.
Superconductivity can be induced by the substitution of either Ba, Fe or As atoms. The Ba layer does not contribute directly to the superconductivity, thus, replacing Ba atoms with species with different number of electrons in their external orbital

introduces a change in the charge density of the system. Indirect doping (i.e. substitution of atomic species that does not directly contribute to the superconductivity) can be holonic, i.e. with the substitution of Ba atoms with alkali metals, that means that holes are added to the charge density, or electronic, i.e. by the introduction of substitutional rare earths at the Ba sites, that increases the electronic charge density.
Direct doping is also possible. The aliovalent substitution of Fe atoms with Co atoms leads to a difference in the charge density. Substitution with Ru is instead isovalent. The substitution of As atoms with P atoms is an isovalent substitution, that leads to the shrinkage of the lattice structure introducing a chemical pressure doping.
An antiferromagnetic ordering, that gives rise to spin-density-waves, emerges at low temperatures in $BaFe_2As_2$. Differently from all the other crystallographic structures, the "122" structure presents an intersection between the magnetic phase and the superconducting dome, as shown in figure 2.5.

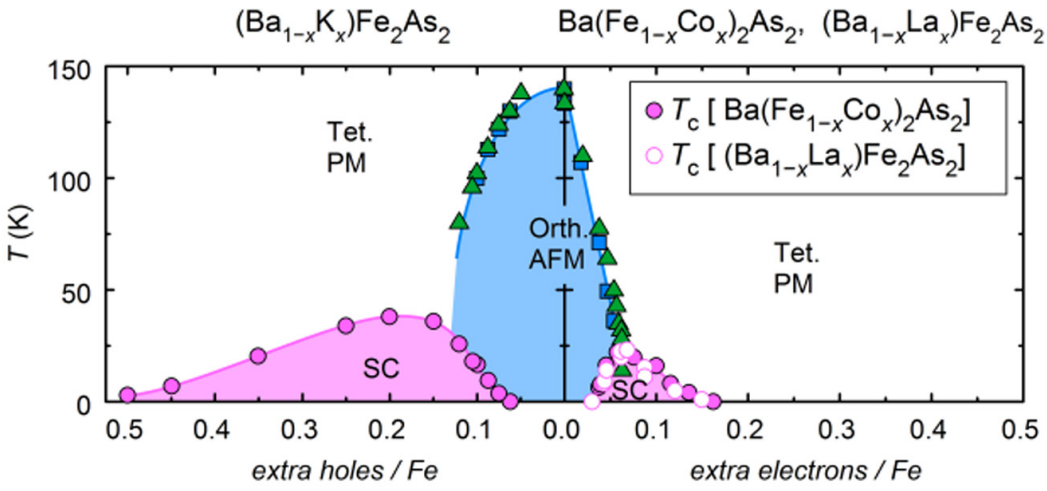

Figure 2.5: Phase diagram of Ba-122 for three different substitutional doping species: holonic- and electronic-doping phase diagrams show a clear asymmetry. (Adapted from Ref. [53]).

Also in this family it often happens that more than one doping methods are simultaneously combined, and frequently it is hard to decouple the effects. Indeed, in this family phase transitions are induced not only by the substitution of Ba, Fe or As with another atomic species, but also by external pressure or strain.
Figure 2.5 shows also that electron and hole doping in this family show significant differences. In fact, by means of hole doping, the maximum T_c reached in a Ba-122 system is 38 K, while with electron doping we cannot exceed $T_c \sim 25$ K. Moreover, the superconducting dome is significantly wider in hole-doped systems. This asymmetry has been attributed to an enhanced Fermi-surface nesting that verifies in the

hole-doped compounds [71]. In fact, nesting is strictly related to the appearance of the magnetic and superconducting phases, even though the reasons why this is true are still unclear [72].
Magnetic anomalies are present in the parent compound with the form of spin density waves. Differently from the other IBSCs structures, the SDW and the SC phases intersect close to the optimal doping value, as if to indicate that the magnetic order competes with superconductivity.

2.2 Fabrication and preliminary characterization of the sample

This chapter presents the electric field effect experiments of optimally doped $BaFe_2(As_{1-x}P_x)$ ultrathin films, which were published in Ref. [73]. We aimed at tuning the T_c of this compound by means of ionic gating. As we have mentioned, the substitution of As with P atoms results in an isovalent doping that induces an additional strain in the lattice but leaves the charge density unchanged. Oppositely, the ionic gating we realized changes the surface charge density but leaves the lattice structure mostly unaffected: the idea is to explore the SC dome by means of two orthogonal methods.
The sample we used to perform ionic-gating experiments were grown at Nagoya University, in Prof. Hiroshi Ikuta's group. The procedure to prepare the sample is well described in Ref. [74]: molecular beam epitaxy (MBE) was used to grow $BaFe_2(As_{1-x}P_x)_2$ films on MgO substrates at a temperature of 850°C and under ultrahigh vacuum conditions, with a base pressure of $\sim 10^{-9}$ mbar. The vapours of Ba, Fe and As were obtained from pure metal sources by means of Knudsen cells, while P vapours were sourced from a GaP cell equipped with a gallium trap that cleaned the flux in order to provide an almost pure P beam. The films were grown at a grow rate of $\simeq 1.67$ nm/min for an exposition time of 6 min, obtaining a final film thickness of $\simeq 10$ nm. The P content was adjusted by controlling the P vapour pressure.
Electron probe microanalysis (EPMA) guaranteed the absence of Ga atoms incorporated in the lattice structure, and the P content resulted in $x = 0.21$, as expected. The $BaFe_2As_2$ in-plane lattice constants slightly differ from the MgO ones; in ultrathin films, this lattice mismatch results in an additional strain of the iron-arsenide lattice structure and in a shift of the superconducting dome towards lower P contents. Thus, in ultrathin films, the optimal doping is exactly $x = 0.21$ [74] while in single crystals it is slightly higher [75].

The crystal structure was also investigated by x-ray diffraction (XRD) experiments (sourced by Cu Kα energy). The XRD pattern, shown in figure 2.6a, confirms that

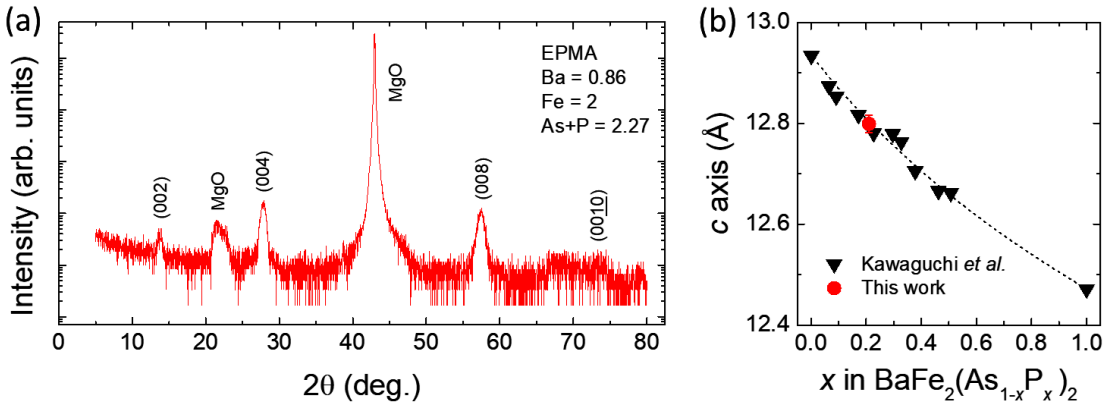

Figure 2.6: (a) the XRD pattern obtained from a Cu Kα energy source. The (002) and (00$\underline{1}$0) are associated to the c-axis oriented lattice constants. (b) the c-axis lattice constant obtained from the XRD pattern is plotted against the P content (red circle); black triangles represent the same quantity for 100 nm thick films grown with the same procedure in Ref. [74]. (Adapted from Ref. [73]).

the film is grown along the c-axis; the c-axis lattice constant is in excellent agreement with the results obtained for the same doping content in 100 nm thin films prepared via the same method [74]. We investigated the topography of the sample by AFM measurements using the tapping mode of a Bruker Innova® microscope. A small $3 \times 3\,\mu\text{m}^2$ region of the film surface is displayed in figure 2.7a. We measured the mean equivalent square size (S) of the grains of our films that results to be $S \simeq 0.1\,\mu$m. Analogous experiments on ~ 50 nm thick films prepared following the same procedures have shown higher values ($S \simeq 0.4\,\mu$m)[76]: this difference can be accounted to the merging of contiguous grains edges that gives rise to larger and smoother overlapping terraces. In fact, the edges of our samples are sharper and the surface roughness, obtained as the root mean square of the heights, is measured to be $S_q \simeq 1.5$ nm; still considerably smaller than the film thickness, ensuring the continuity of the film itself.
In order to measure the transport properties of the sample, we submitted the films to photolithography, and to Ar-milling (at a pressure of 10^{-3} mbar, with an extraction voltage of 400 V and an anode current density of 1.2 mA/cm^2), giving the conductive path the characteristic Hall-bar shape. After patterning the film, the sample presented a central and wider strip along which, perpendicular to it, voltage contacts are paired at both sides. Each channel between two adjacent voltage contacts is 1 mm long and 0.3 mm wide.

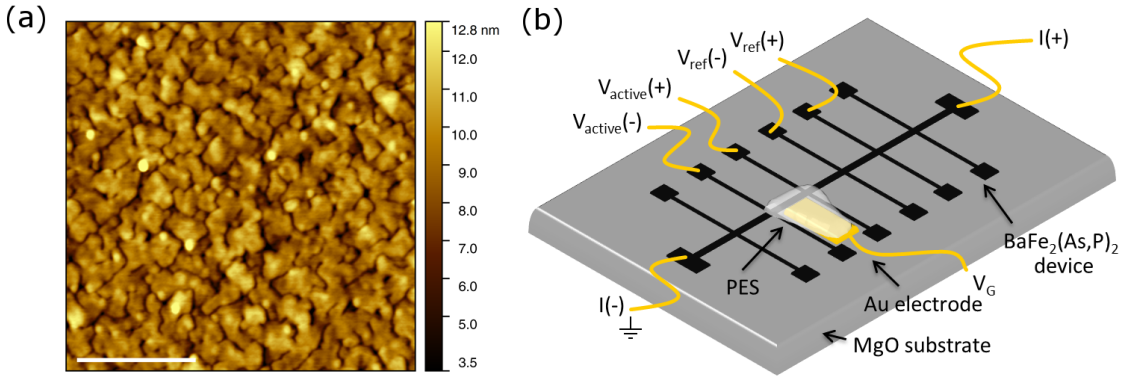

Figure 2.7: (a) AFM topographic image of a $3 \times 3\,\mu m^2$ area of a device surface acquired in the tapping mode: the colour scale shows the different height of the grains. The roughness, calculated as the root-mean-square height is $S_q \simeq 1.5$ nm, well below the film thickness. The scale bar represents 1 μm. (b) Sketch of a device ready to be measured: there are shown the electrical connections, that are required for the four-wire resistance measurements and the gating experiments as well as the PES droplet and the gold side-gate electrode. (Adapted from Ref. [73]).

2.3 The PES choice and the drop-casting of it

The choice of the suitable polymer electrolyte system (PES; see Chapter 1) resulted to be of fundamental importance in order to perform reliable ionic gating experiments.

The PES we used is composed by a soft, cross-linked polymeric matrix, made of a weighted mixture of BEMA dimethacrylate oligomer (i.e. bisphenol A ethoxylate-dimethacrylate; average $M_w \sim 1700$ daltons, Sigma Aldrich) and PEGMA mono methacrylate based reactive diluent (i.e. poly(ethylene glycol) monomethyl ether monomethacrylate; average $M_w \sim 500$ daltons, Sigma Aldrich) in 7:3 ratio along with 3 wt % of free radical photo initiator (Darocur 1173, Ciba Specialty Chemicals). Dissolved in this matrix, we added 10 wt% of lithium bis(oxalato)borate salt (LiBOB).

The PES, such made, shows a glass temperature around 240 K.

The advantage of the polymeric matrix used in our experiments is that the salt ions are not bounded to any specific molecule of the mixture, increasing the capacitance of the system, when polarized, with respect to other standard polymer electrolytes [9]. LiBOB has a superior chemical and electrochemical stability with respect to more standard salts, like lithium perchlorate (LiClO4) or lithium bis(trifluoromethanesulfonyl)imide (LiTFSI)[77–79] as well as higher thermal stability and less corrosive hydrolytic decomposition products. In addition, when the electrochemical cell is polarized, a solid electrolyte interface (SEI) forms at the interface with the electrodes[77]; thus, preventing chemical interactions between the

investigated material and the electrochemical cell. Finally, we tried to use different salts dissolved in the polymeric medium, but experiments resulted in deterioration of our sample: electrochemical modification induced permanently, or complete etching and dissolution of $BaFe_2(As_{1-x}P_x)_2$ films leaded to device failures in all the other cases.
In the following we are going to report the various trials we performed. Just before this, we want to stress that using LiBOB has also some drawbacks. In fact, the ion mobility is limited with respect to other ionic salts and the conductivity is lower [77]; moreover, it has poorer performances at low temperatures.
Finally, we drop-casted the liquid precursor to the PES on one channel of each device in the controlled atmosphere of a dry room and we UV-cured it. The geometry of the device allowed us to perform simultaneous measurements on the channel covered by the PES (the active channel) and on one of the ungated channels; the active channel, behaving as one electrode of the electrochemical cell, measures the effect of the electric field, while the other channel works as a reference for the measurements. The counter electrode is made of a gold leaf that is dipped into the PES.

2.4 The ionic gating experiments

After the preparation of the samples, the devices were transferred in the vacuum chamber of a Cryomech® pulse-tube cryocooler and subsequently they were left to degas, under high vacuum conditions ($\lesssim 10^{-5}$ mbar) for an appropriate time (at least 1 hour) to let the water evaporate out of the PES. Electric resistance was measured by sourcing a few μA current with a low-noise Keithley 6221 current source to the current contacts of the device, and the voltage drop was measured across the active and reference channels by means of a Keithley 2182 nanovoltmeter. The source-to-drain current was inverted at each measurement to remove the offset currents (e.g. the thermoelectric current).
We measured the four-wire resistance in the temperature range between 5 K and room temperature; measurements were performed during the slow heating process, allowing the sample to heat up uniformly with the whole system. A preliminary measurement was performed at each active channel before the drop-casting of the PES, in order to have a record of the films resistance before any changes due to the electrolyte application. One of these measurements is displayed in figure 2.8 (red line) and is compared to a 50-nm-thick sample with almost the same P content ($x = 0.19$; blue line): the red-line sample is way more resistive and this mainly stems from the difference of the residual resistivity ρ at low temperature; T_c is strongly reduced in the thinner sample and the transition is way broader. In particular, defining T_c^{90} (T_c^{10}) the temperature at which $\rho(T_c^{90})$ ($\rho(T_c^{10})$) equals the 90% (10%) of ρ(32 K), in the thinner sample T_c^{90} - T_c^{10} is 8.7 K compared with the 0.5 K

of the thicker sample. Notice that the 50-nm-thick sample T_c is in agreement with 100-nm-thick samples grown via the same method and with a comparable doping content [74]. This means that the suppression of superconductivity must be due to the film thickness reduction from 50 nm to 10 nm.

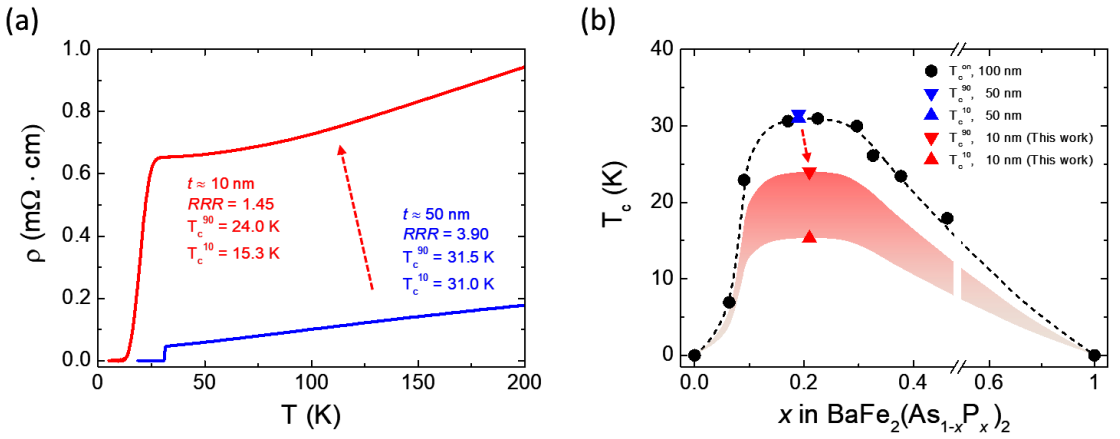

Figure 2.8: (a) Resistance as function of temperature for our 10-nm-thick film (red line) and for a 50-nm-thick film from Ref. [9]. Notice that the thinner sample is way more resistive and the superconductivity is suppressed. (b)The superconducting dome for 100-nm-thick films (Ref. [74]) is compared with the superconducting transition temperature of the 50-nm-thick sample in Ref. [9] and our 10-nm-thick sample; the red shadowed band is a guide for the eye and represents how could appear the superconducting dome of the thinner film. (Adapted from Ref. [73]).

There can be two different reasons why the reduction of the film thickness leads to a suppression of T_c and a broadening of the transition. The first reason that has to be taken into account is an intrinsic feature of the $BaFe_2As_2$ family when reduced in thin films: it is known that in $Ba(Fe,Co)_2As_2$/STO superlattices a suppression of superconductivity and a broadening of the transition have been observed when the Ba-122 layer thickness approaches $\sim$ 12 nm [80], and superconductivity disappears reaching $\sim$ 3 nm [81]. Even though we cannot exclude this interpretation, there is a second reason, that seems to better fit for the results we had. Indeed, the morphology of the film that we measured via AFM measurements shows a granular growth of the film that can both strongly affect the superconducting properties and increase the resistance at low temperature, especially when in-plane misalignment is present between the grains. The sharp edges of the grain, moreover, limit the superfluid connectivity of the superconducting state that shows a weak-link behaviour [82, 83]. It is also clear why in thicker samples the same behaviour is not present: as stressed before, AFM measurements on 50-nm-thick sample in Ref. [9] underlined that the grains are connected by the coalescence of themselves, forming quasi-continuous terraces. Moreover, the unavoidable oxidation of the exposed

surfaces [84], that happens when the sample is removed from high vacuum conditions, contributes to increase the sample resistance and the SC suppression, and it is surely more effective in the thinner film for the higher surface-to-volume ratio and for the rougher (and thus wider) exposed film area per device area unit.
Reducing the film thickness is a crucial requirement for electric field effect experiments on high carrier density systems, because, as we have seen in the previous chapter, in such systems, a few atomic layers are enough to screen out the external electric field even in the case of such high electric fields as those that can be induced by ionic gating [85]. Moreover, since only the first layers are affected by changes made by the external electric field, in superconducting systems reducing the thickness is crucial because of the proximity effect that dilutes the perturbation to the superconducting order parameter in the whole bulk, and the thicker the bulk is, the smaller is the effect of surface modification over the whole film thickness (that is what we can measure) [27, 86].
After the drop-casting of the PES, we measured the behaviour of our samples under gating. We used two different samples, prepared in the same way and grown in the same batch in order to have consistency of the measurements. By means of a Keithley 2410 source measure unit (SMU), the gate voltage (V_G) was applied between the negative current terminal and the gate counter electrode, and simultaneously the gate current (I_G) was measured. We decided to perform the application of V_G at a temperature of 290 K, not too high in order to reduce the possibility of electrochemical interactions, and not too low in order to not to reduce excessively the ionic conductivity, that is well known to be very low in LiBOB-based electrolytes.
The induced charge density has been measured via the double-step chronocoulometry (DSCC) method that we introduced in the previous chapter. Figure 2.9b shows the measured I_G (solid black line) and the fitting curve (red dashed line).

2.4.1 The electrostatic charging of LiBOB-based PES

The considerable induced charge density ($\Delta n_{2D} \sim 10^{14}\,\mathrm{cm}^{-2}$), combined with very long transient times observed in figure 2.9 could lead to think that the system had gone beyond the electrostatic limit. However, we will show in the following that the measured quantities are in line with a purely electrostatic regime.

The specific capacitance of the sample/PES interface Supposing that the charge accumulation occurred electrostatically, from the measured Δn_{2D} values, we obtain the effective gate capacitance per unit area as:

$$C_G = \frac{e \cdot \Delta n_{2D}}{V_G} \tag{2.1}$$

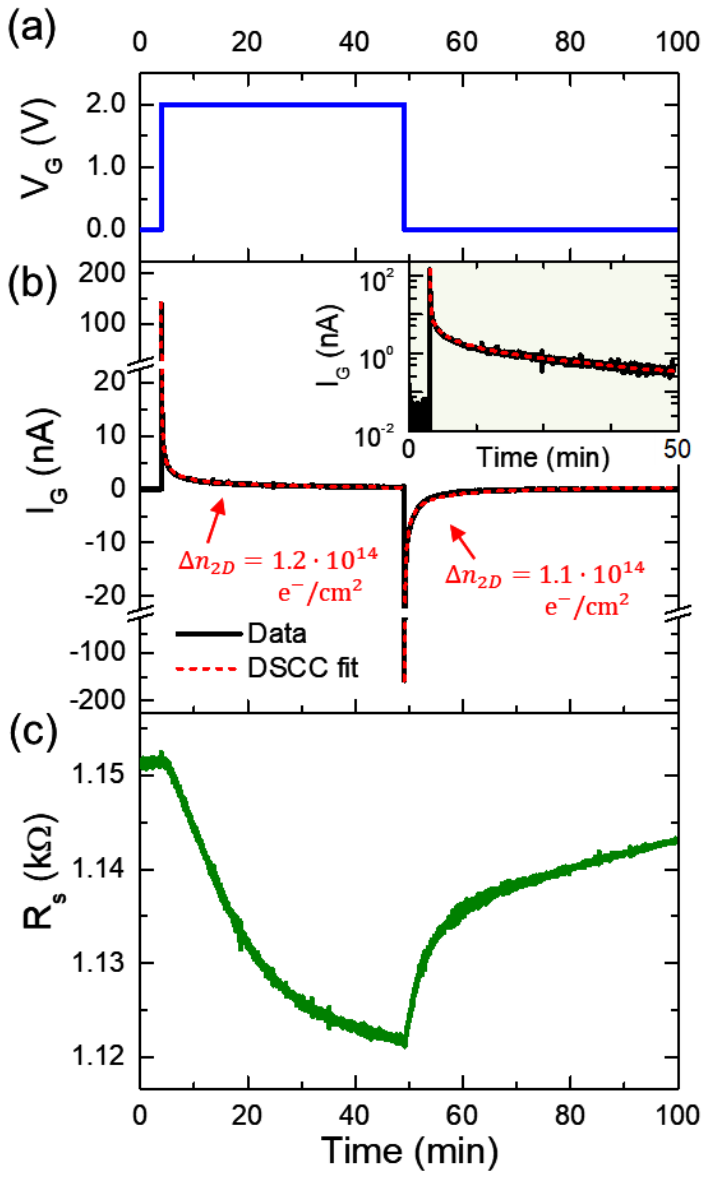

Figure 2.9: The DSCC process for the active channel of a 10-nm-thick film of $BaFe_2(As_{0.81}P_{0.19})_2$. The figure is divided in three panels: the step-like application of V_G (a), the gate current I_G (b), and the sheet resistance modulation (c) are represented as function of time. In the inset of (b), the I_G is shown in semi-logarithmic scale. (Adapted from Ref. [73]).

where e is the electron charge.
In order to check whether such high Δn_{2D} values can be reached via purely electrostatic doping in our setup, we need to check if C_G is comparable with the specific

capacitance we expect from the PES we employed (C_{PES}).
The specific capacitance of an EDL can be roughly estimated as the effective capacitance of a parallel plate capacitor which distance between the armatures is the sum of the Helmholtz layer thickness d_H and the Debye length λ_D [87]; thus, it can be expressed as:

$$C_{PES} = \frac{\epsilon_r \epsilon_0}{d_H + \lambda_D} \tag{2.2}$$

where ϵ_r is the dielectric constant of the ionic medium and ϵ_0 is the vacuum permittivity. Indeed, C_{PES} depends on quantities that are specific of the PES composition: d_H, λ_D and ϵ_r.
We assume that the dielectric constant of our BEMA-PEGMA mixture is comparable to that of PEG, which means $\epsilon_r \approx 4 - 6$ [88].
Then, as far as λ_D is concerned, Ref. [87] and Ref. [89] point out that it can be expressed as:

$$\lambda_D = \sqrt{\frac{\epsilon_r \epsilon_0 k_B T}{2e^2 N_A I}} \tag{2.3}$$

where k_B is the Boltzmann constant, T is the temperature, N_A is the Avogadro number and I is the ionic strength of the electrolyte which results $\simeq 1.1$ g mL^{-1} considering our PES composition. This, in turn, results in $\lambda_D \approx 0.9 - 1.1$ Å at $T \sim 290$ K.
Finally, we consider the Helmholtz layer thickness. Typical values of d_H result in few Å: in other words, the Debye length λ_D, estimated for our PES composition is smaller than d_H, confirming that the EDL is a compact layer at the interface with the sample. Thus, the specific capacitance C_{PES} is dominated by the contribution of the Helmholtz layer. In addition, we stress the fact that, for a correct estimation of d_H, its potential-dependency should be taken into account. Concluding, since our rough estimation is meant to return an order of magnitude of the specific capacitance we are expecting in our experiments, we choose a total effective EDL thickness ~ 3 Å. Figure 2.10a shows the results for C_G and C_{PES}: the two quantities values are of the same order of magnitude.

Characteristic times of the LiBOB-based PES gating We can determine the transient times of the gating process by assuming the following prepositions: (i) the total capacitance associated with the gold counter electrode is far higher than that related to the working electrode due to the larger area of the former compared with the latter; (ii) the current flux in the PES bulk is dominated by the contribution due to the motion of the ions (with resistance R_b), rather than to the bulk dielectric charging (with specific capacitance C_b), since the measured transient times are significantly long; (iii) waiting for longer times the gate current becomes immeasurably small, meaning that the resistance across the EDL is immeasurably

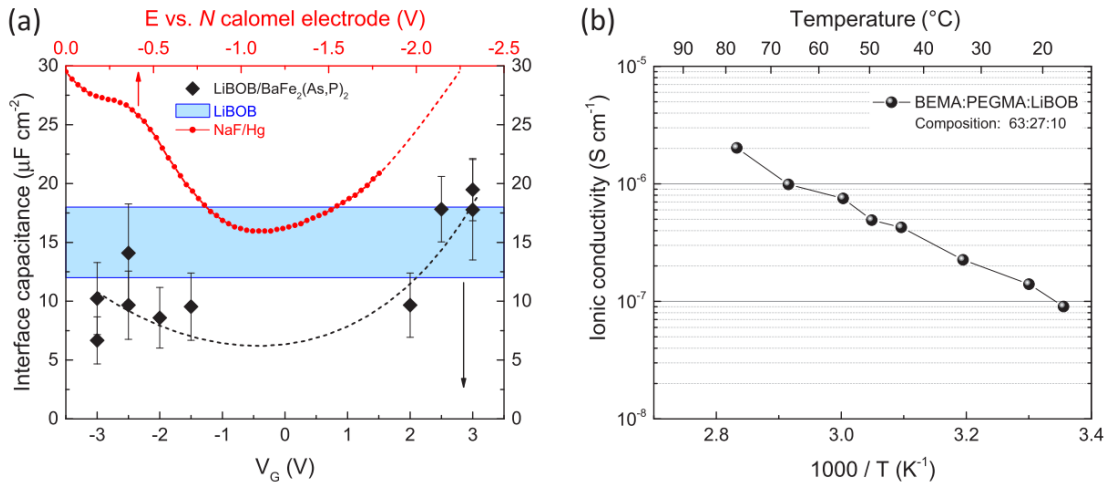

Figure 2.10: (a) The specific capacitance of three different electrode/liquid interfaces are compared. The black diamonds represent the values obtained with eq. 2.1 from DSCC measurements of Δn_{2D} for different V_G applications in our LiBOB-based PES/$BaFe_2(As,P)_2$ system. The shaded light blue band shows the values obtained with eq. 2.3 for our PES composition. Red circles are reported for comparison: they show the specific capacitance of a standard NaF/Hg interface system (adapted from [87]). (b) LiBOB-based PES ionic conductivity vs. T^{-1}. (Adapted from Ref. [33])

large; (iv) oppositely, the resistance associated to the $BaFe_2(As,P)_2$ electrode is negligible.
With these simplifications, we can approximate the gate circuit to a RC circuit, and its characteristic time is defined as:

$$\tau_G = R_b \times C_{EDL} \tag{2.4}$$

being C_{EDL} the double-layer capacitance.
Apart from geometrical considerations about the PES drop, R_b can be determined by experimentally measuring the ionic conductivity σ_{ionic}. To do so, we performed electrochemical impedance spectroscopy (EIS) analysis and the results are shown in figure 2.10b: the value at $T \sim 290$ K is $\sim 9 \cdot 10^{-8}$ S cm^{-1}.
Finally, R_b is obtained as:

$$R_b = \frac{l_{G-Ch}}{\sigma_{ionic} \cdot w_{drop} \cdot t_{drop}} \tag{2.5}$$

where l_{G-Ch} is the distance between the gold counter electrode and the gated channel in the side gate configuration and w_{drop} and t_{drop} are respectively the drop width and thickness.

The resulting $\tau_G \approx 5 - 10$ min is perfectly in accordance with the transient times that our devices exhibited. In conclusion, as far as the electrochemical cell is concerned, the measured induced charge densities and the transient times are likely in accordance with a purely electrostatic behaviour; other contributions, if present, beyond the electrostatic regime, are of secondary importance and below our detection limit.

2.4.2 Gate-induced modulation of the resistance

As we have already seen in figure 2.9, the application of the gate voltage leads to a modulation of the sheet resistance R_s: the investigation of the device response to V_G, and, in particular, to the induced charge densities Δn_{2D} is shown in figure 2.11 and it exhibit a linear dependence of ΔR_s as function of Δn_{2D}. A simple, free-electron model of a single-band metallic film of thickness t and carrier density per unit volume $n_{3D,0}$, within the assumption that the effective mass and the scattering lifetime are not affected by the gating, gives that [9, 90]:

$$\frac{\Delta R}{R'} = \frac{R(\Delta n_{2D}) - R(0)}{R(\Delta n_{2D})} = -\frac{\Delta n_{2D}}{n_{3D,0} \cdot t} \tag{2.6}$$

This relation tells us that, in the case in which the only effect of the doping is to change the charge density of the system, the relation between R_s and Δn_{2D} is consistent with a linear dependence, where the slope sign depends on whether the charge carriers are electrons or holes. For our multiband system, we expect that the contributions to ΔR coming from the electronic and holonic charge carriers should partially cancel out; however, we have an overall negative slope, concluding that the conductivity is dominated by negative charge carriers. The inset of figure 2.11 shows that the $\Delta R/R'$ vs. Δn_{2D} behaviour is consistent with the results obtained on different metallic thin films under electrostatic gating [9, 26, 27, 90, 91], but, in our case, there is a clear difference in slope between electron accumulation and depletion that was not observed in the other metals. A similar asymmetry has however been observed in ion gating experiments on very surface-sensitive materials (like black phosphorus [92], and single-layer [93] and few-layer [94, 95] graphene) and was due to the introduction of scattering centres at the interface between the material and the electrolyte with different efficiency between cations and anions. Consequently, the scattering time is affected by the gating in an asymmetric way, and, relaxing this hypothesis, eq. 2.6 can be rewritten as:

$$\frac{\Delta R}{R'} = -\frac{\Delta n_{2D}}{n_{3D,0} \cdot t} \cdot \frac{\tau(\Delta n_{2D})}{\tau(0)} \tag{2.7}$$

considering now that doping-dependent quasiparticle scattering lifetime ($\tau(\Delta n_{2D})$) and unperturbed one ($\tau(0)$) are different. In our case, it comes out that $\tau|_{\Delta n_{2D}<0} <$

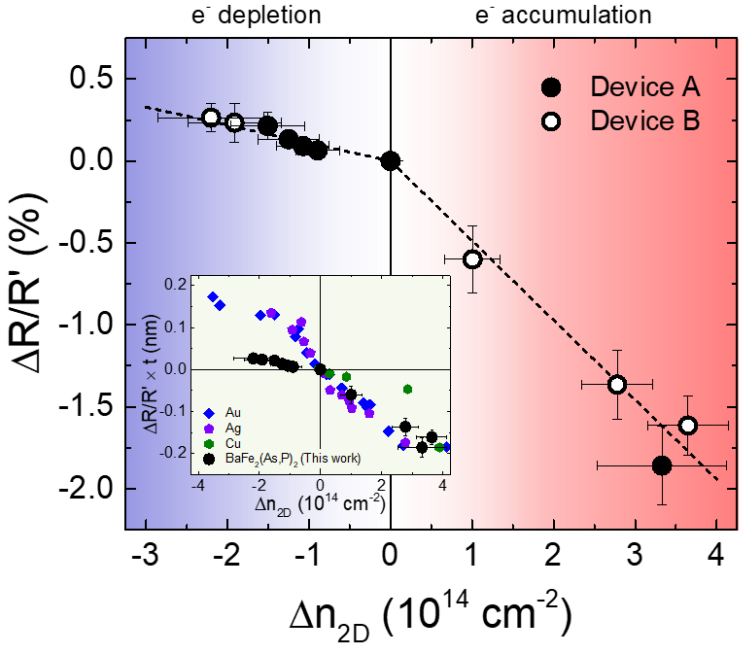

Figure 2.11: The resistance modulation $\Delta R/R'$ as function of the induced charge density Δn_{2D}, at the V_G application temperature $T = 290$ K. Measurements on the two different samples grown on the same batch are reported with filled and hollow circles. Error bars are calculated by comparing the ΔR and Δn_{2D} obtained for the application and for the removal of V_G. The linear fit of the experimental data (dashed line) is obtained with the fit function eq. 2.7. In the inset is reported the dependence of $\Delta R/R' \times t$ vs. Δn_{2D} for our $BaFe_2(As,P)_2$ sample compared with Au (blue diamonds; adapted from Ref.[9]), Ag (violet pentagons; adapted from Ref.[90]) and Cu (green hexagons; adapted from Ref.[90]) thin films. (Adapted from Ref. [73]).

$\tau|_{\Delta n_{2D}>0}$; more explicitly, the application of $V_G < 0$, that brings the BOB^- anions at the interface with the material (and the formation of the SEI) is more effective in introducing extra scattering centres than $V_G > 0$, where the Li+ cations face the surface of our devices.

2.4.3 Possible doping beyond the electrostatic regime

The observation of the asymmetry shown in figure 2.11 brings us to investigate deeper the presence of other kind of doping, beyond the electrostatic one.
First of all, ions can exit from their solvation shell and be adsorbed on the electrode interface [87].

We performed linear sweep voltammetry (LSV) at $T \sim 295$ K to evaluate the electrochemical stability window of the LiBOB-based PES. Cu and Al foils were used as the cathodic and the anodic working electrodes, while Li was used as the counter electrode of the three-electrodes electrochemical cell; the voltage was applied with a constant sweep rate of 0.1 mV/s. Figure 2.12a shows the current response to the application of the electric potential: a flat plateau extends up to the breakdown voltage, confirming that the high purity of the PES is preserved and its contamination with moisture is prevented (since there is no water-decomposition peak, which should appear at ~ 4.0 V). Definitely, the electrochemical stability window extends up to a threshold voltage of ~ 4.6 V, well beyond our range of V_G application (that is $\leq \pm 3$ V).
Figure 2.12b shows the cyclic voltammetry performed in a two-electrodes electrochemical cell where one of the electrodes is made of $BaFe_2(As,P)_2$ ~ 100 nm thick unpatterned films with stoichiometry comparable to our samples (P content $x = 0.2$), and the electrolyte is the LiBOB-based PES. The symmetric V_G sweeps up to the application of $V_G = \pm 3$ V always show a correspondent current density reasonably small and well below (~ 100 times smaller) the values reached exceeding the LSV threshold voltage even with a voltage application rate of 1 mV s^{-1} (10 times faster than in LSV): even at the highest applied V_G, our experimental regime remains within the electrochemical stability window of the of LiBOB-based PES/$BaFe_2(As,P)_2$ interface.
A second possible cause of gating beyond the electrostatic regime is intercalation. As we have seen, intercalation is encouraged by the layered structure of Ba-122. The large size BOB^- anions intercalation would delaminate the layered structure [16], and thus it is easily excluded. Li^+ cations are smaller in size, and Li^+ intercalation is possible. However, in order to activate bulk intercalation a gate electric field higher than a certain threshold is required followed by a relevant increase of the disorder [16, 96, 97], that does not match with the linear dependence of $\Delta R/R'$ vs. Δn_{2D} that we observed (figure 2.11). Moreover, the 122 family is known to be resistant to positively charged ions intercalation because of the repulsing alkaline-earth charge reservoirs, with the exception of the Sr-122 parent compound, that, we have seen, is spontaneously subjected to water intercalation [53]. Finally, we do not reveal significant Li^+ content in the XPS analysis that we carried out after the experiments - and that we will present in a while -, neither at the surface nor in the bulk of the material. We can thus conclude that intercalation is very unlikely to occur.
Crystal lattice distortions can represent a possible third cause of non-electrostatic doping. It raises when the field application leads to displacements of the charge reservoir atoms from their equilibrium position; this mechanism has been recently proposed to justify the long relaxation times in ZrNCl ionic gating experiments [98]. To demonstrate that the Ba^{2+} atoms are not subjected to permanent deintercalation, we performed XPS measurements. We will show that the Ba $3d_{3/5}$ spectrum

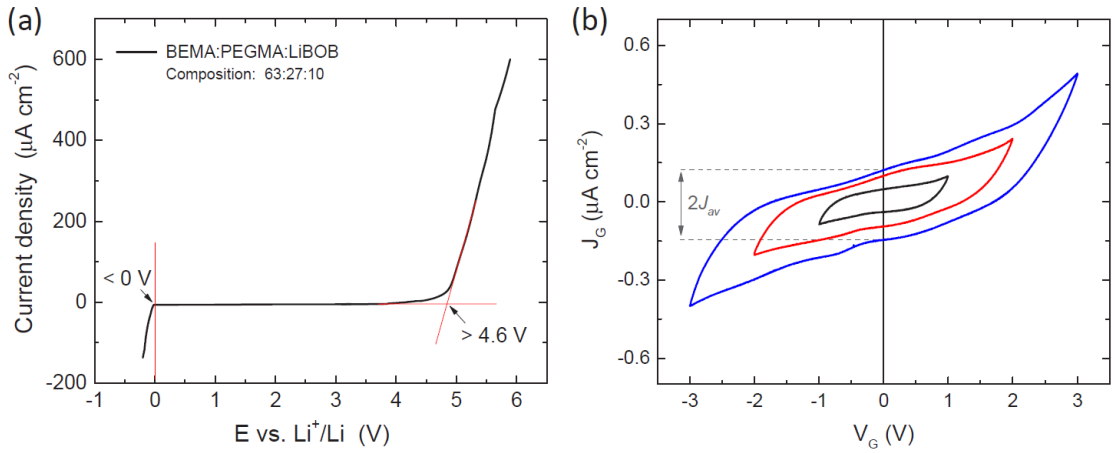

Figure 2.12: (a) Linear sweep voltammetry of the LiBOB-based PES. A three-electrodes electrochemical cell equipped with a Cu foil cathode, an Al foil anode and a Li metal counter electrode was used, by sweeping the electric potential at a constant rate of 0.1 mV s^{-1}. (b) Cyclic voltammetry of the LiBOB-based PES. The electrochemical cell is equipped with one of the two electrodes made of $BaFe_2(As,P)_2$ thin film, analogous to the patterned samples, with larger exposition area, very similar stoichiometry and ~ 100 nm thick. Blue line, red line and black line correspond to cyclic voltammetry with different V_G range of application: respectively, $|V_G| < 3$ V, $|V_G| < 2$ V and $|V_G| < 1$ V. The V_G application rate is 1 mv s^{-1} (Adapted from Ref. [33]).

is insensitive to the gating process.
XPS measurements are also intended to give a deeper insight on possible irreversible electrochemical interactions at the PES/sample interface. To do so, we performed XPS measurements before and after the application of the gate voltage.
To acquire the different XPS spectra we used one of the unpatterned $BaFe_2(As,P)_2$ films exploited in the cyclic voltammetry measurements. The sample was preliminary left degassing overnight to reach a pressure below $\sim 5 \cdot 10^{-8}$ mBar. A built-in Ar-ion gun allowed to perform an optional cleaning of the surface by etching the first atomic layers of the sample.
Figure 2.13 shows the spectra we acquired for this sample: we performed four XPS measurements on the same sample (i) before gating (solid black line), (ii) after the exposure to air and chemicals (solid red line), (iii) after gating (solid blue line), (iv) and, finally, after cleaning the sample (solid green line). For each of these measurements, we acquired a full survey scan up to 1200 eV (see figure 2.13a) and three high-resolution scans to zoom in the energy ranges close to where expected the Ba $3d_{3/5}$, Fe 2p, and Li 1s peaks (which are respectively shown in figures 2.13b, 2.13c, and 2.13d).

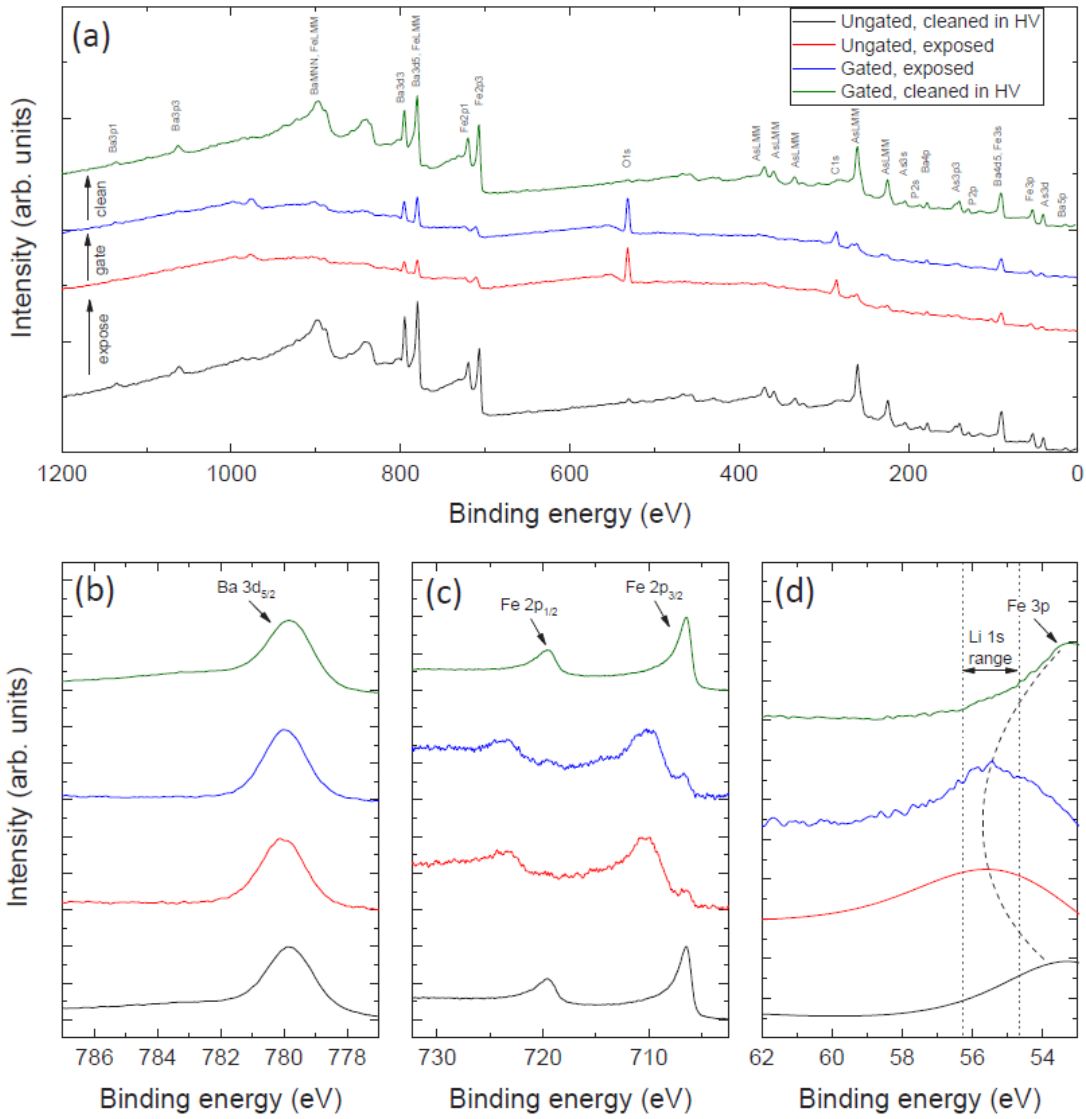

Figure 2.13: XPS spectra acquired on a $BaFe_2(As,P)_2$ $\sim$ 100 nm thick film. The spectra are acquired at four different stages: (i) after cleaning the pristine sample via Ar-ion etching (solid black line); (ii) after exposure to LiBOB-based PES, air and moisture (solid red line); (iii) after the proper gating process (solid blue line); (iv) after a further Ar-ion sputtering (solid green line). Panel (a) shows the full survey scan up to 1200 eV. The peaks are analysed with Multi Pak Software. Panels (b), (c) and (d) show respectively the high-resolution spectra of the Ba $3d_{3/5}$, Fe 2p, and Li 1s regions. (Adapted from Ref. [33]).

The first XPS set of spectra was acquired on the pristine film, after sonication in acetone, ethanol and 2-propanol, and after the cleaning of its surface by Ar-ion

sputtering. The so-acquired spectrum is consistent with Ba-122 crystals cleaved *in situ* under high vacuum conditions [84, 99, 100]. The low intensity of the O 1s and C 1s spectra is a sign of the low degree of contamination of the surface (figure 2.13a); the absence of satellites of the Fe 2p spectrum confirm a negligible Fe oxidization. We can conclude that the pristine sample shows ideal conditions as far as the surface chemistry.
After having characterised the surface of the film at ideal conditions, we exposed the sample to air and to the LiBOB-based PES for a controlled time, but without performing proper gating; then we sonicated the sample in order to remove the electrolyte. What we expect is to find considerable traces of oxygen and carbon contamination coming from the PES residuals, and also traces of Fe oxidation as well as signs of degradation due to the sample exposure to air and moisture. Indeed, the set of spectra acquired at this stage clearly show what expected (see solid red line in figure 2.13): O 1s and C 1s peaks are present in the survey scan; the peaks associated to Fe 2p are now noisy and surrounded by a lot of satellite peaks; also the Fe 3p peak is shifted at higher energies. However, the Ba $3d_{3/5}$ peak does not show any change, suggesting that the Ba layer is inert to PES and air. It is reasonable to conclude that the exposure of the sample to LiBOB-based PES and ambient conditions lead to a mild surface contamination.
The third set of spectra (solid blue line in figure 2.13) is acquired after the cyclic voltammetry measurements. In order to test the system in conditions similar to the actual field effect gating experiments, we additionally applied step-like $V_G = \pm 3$ V application for more than 30 min. The sample was sonicated and then measured. The spectra acquired are closely similar to that at the previous stage. We can conclude that no permanent modification due to the application of V_G is present. We also notice the absence of the Li 1s peak, which should appear in the energy range 55 – 56 eV, meaning that no Li^+ ion remains adherent to the sample.
Finally, the fourth and last set of spectra (solid green line in figure 2.13) is acquired by performing Ar-ion sputtering to clean the surface and to remove the very first atomic layers: the accordance with the first data collected on the pristine sample is really high.
We can finally conclude that the gating process does not lead to changes of the sample surface chemistry. Indeed, the main changes that XPS measurements highlighted stems from the surface exposition to PES and air conditions, while the gating process does not add further changes. Moreover, the Ar-ion etching of few atomic layers restores the surface chemistry of the pristine sample: thus, possible effects that go beyond our detection limit are, in any case, confined at the surface of the film. Finally, field-assisted protonation of the lattice could represent a fourth source, as it was reported in the cases of $SrCoO_3$ [101] and $SrTiO_3$ [102]. It is due to the presence of residual water in the gate electrolyte that undergoes electrolysis. In our voltammetry measurements, no clear peaks referring to water hydrolysis are present, qualitatively confirming the absence of water hydrolysis. A quantitative

analysis would require XRD characterization of the film concurrently with the electric field application; a requirement that cannot be fulfilled by our experimental setup.
Concluding, it is reasonable to say that the electrostatic doping is largely dominant with respect to the other contributions.

2.5 Tuning of the superconducting transition

We performed several thermal cycles on different channels of both the samples, and for different applied V_G (i.e. different charge doping). At each cycle, the R-T curve has been recorded for the active channel and the reference channel, and T_c^{10}, T_c^{50}, and T_c^{90} have been measured for both, so that the broadening of the transition could be taken into account. In order to detect the T_c shift of the active channel due to the electric field with a resolution of some mK, we define the difference between the active and reference channel T_c as:

$$\delta T_c(\Delta n_{2D})|_i = T_{c,act}(\Delta n_{2D})|_i - T_{c,ref}|_i. \tag{2.8}$$

Notice that $\delta T_c(\Delta n_{2D} = 0) \neq 0$ because the sample is not perfectly homogeneous; furthermore, within two different cycles i and j, $T_{c,ref}|_i \neq T_{c,ref}|_j$ because of slight differences in the thermal contacts or in the heating rate. Both these issues are sidestepped by the following differential method used to calculate the doping-dependent T_c shift ($\Delta T_c(\Delta n_{2D})$). In this method, $\Delta T_c(\Delta n_{2D})$ is defined as:

$$\Delta T_c(\Delta n_{2D}) = \delta T_c(\Delta n_{2D}) - \delta T_c(0). \tag{2.9}$$

In figure 2.14a we report the effect of different values of Δn_{2D} on the $R-T$ curve close to T_c^{50}. The recorded T_c shifts as function of the charge doping result in a suppression of superconductivity for both electron depletion and accumulation, with a stronger effect in the case of electron accumulation. Moreover, the T_c shifts are mostly reversible, since the original T_c value is restored once the gate voltage is removed, the device is heated up to 290 K and after waiting for several tens of minutes (that are required because the ion dynamics of LiBOB-based PES are very slow, as we have seen). In very few cases where the aforementioned procedure did not work, we removed the PES and rinsed the device in ethanol in order to completely restore the original T_c, that could anyway be recovered. The reversibility of the process is another evidence that T_c is mainly tuned via electrostatic charge doping [9, 27]: if any electrochemical reaction occur, however they do not modify permanently the superconducting properties of the films. Support to this is also given by the XPS analysis of the gated film surface [33]. It is likely that the not-completely-reversible behaviour can be ascribed to charged ions trapped for long

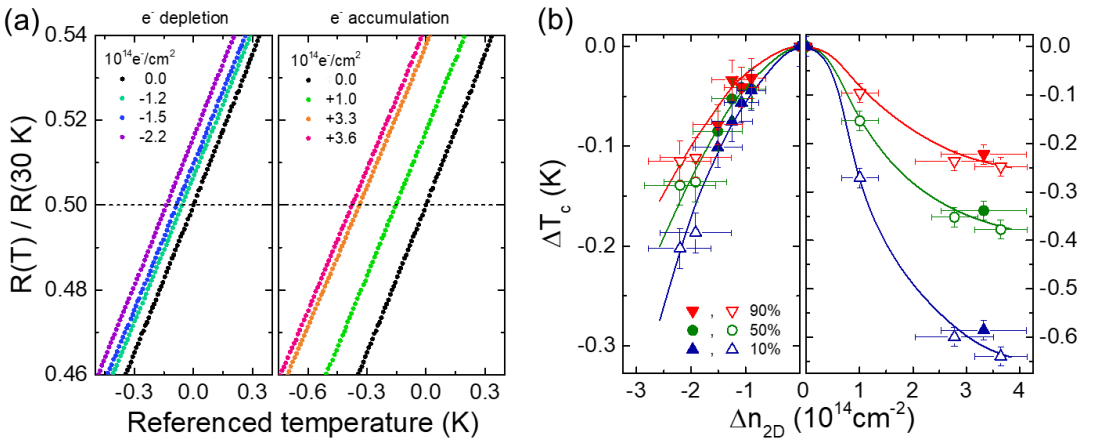

Figure 2.14: (a) R vs. T curves for values close to T_c^{50} for different values of Δn_{2D}. The resistance is normalized by its value at 30 K (i.e. $R(T)/R(30\,\mathrm{K})$; the temperature is referenced to $T_c^{50}|_{\Delta n_{2D}=0}$; on the left, electron depletion (hole doping); on the right, electron accumulation (electron doping). (b) The shifts in T_c^{10} (blue up triangles), T_c^{50} (green circles) and T_c^{90} (red down triangles) are represented as function of the induced charge density Δn_{2D}. Hollow and filled symbols represent the data obtained on the two different samples from the same growth batch. (Adapted from Ref. [73]).

time in the SEI that forms when the electrolyte is polarized [77], or to a crystal lattice distortion, induced by the gating [98]. All the reversible ΔT_c values as a function of Δn_{2D} are summarized in figure 2.14, reporting the T_c^{90}, T_c^{50} and T_c^{10} values. Notice that the tail of the superconducting transition (T_c^{10}) experience a higher variation upon charge doping than the onset (T_c^{90}); a broadening of the transition is realized for increasing charge doping. Considering what is reported in Ref. [26, 27] about ionic gating on NbN, a standard, metallic, electron-phonon superconductor and on Ref. [103] about $YBa_2Cu_3O_{7-\delta}$, a high-T_c superconductor, we notice a starkly different behaviour of the SC transition changes: in those cases, the changes in the transition result in a rigid shift of T_c without any broadening. It was there demonstrated that such behaviour stems from the homogeneous modification of the SC order parameter over the whole bulk of the film; oppositely, broadening can arise from a spatially-dependent change in the SC state [104]. Therefore, we are led to think that the SC order parameter is perturbed not homogeneously by the induced charge density across the film thickness: this is in agreement with the very small out-of-plane coherence length of $BaFe_2(As,P)_2$ ($\xi_c(0) \simeq 11 \div 15$ Å) [105]. Moreover, the more pronounced broadening for electron doping (w.r.t. hole doping) for comparable doping values, suggests that there are different length scales of the SC order parameter perturbation in the two cases. Considering that $\xi_c(0)$

is small, we can imagine that the perturbation of the SC order parameter occurs on a similar length scale as the charge density changes; this suggests that electron accumulation and depletion spread differently in the out-of-plane direction. In the case of electrostatic regime, we can ascribe the asymmetry shown in figure 2.14 as a different electrostatic screening length for electrons and holes, as it is in the case of gated MoS_2 [106]. But broadening of the transition can occur also in the case that the polarization of the electrolyte induce an increase of the disorder in the material. As an example, the introduction of impurities and scattering centres at the surface is a well-documented cause of this behaviour in several different materials [92–95, 107–111]. However, we know that the SC transition in $BaFe_2(As,P)_2$ is resistant to external sources of disorder [76, 112, 113], and thus, we consider this contribution to be negligible. Moreover, as we have seen in the scaling of $\Delta R/R'$ as function of Δn_{2D} in the normal state, our PES introduces disorder more efficiently by hole doping with respect to electron doping, while we have a larger broadening upon electron doping. We conclude that the broadening is mostly likely introduced by electrostatic effects rather than the introduction of disorder.

2.6 Discussion and conclusion

The results presented in this chapter show that the ion-gate-induced charge doping is detrimental to the SC properties of an optimally P-doped system.
The combined effects of chemical substitution and external pressure application have been deeply investigated in order to control the SC state. In many previous works, given a fixed quantity of substitutional doping per each sample, the external pressure was quasi-continuously tuned externally showing that SC was boosted only in the cases where the substitutional doping contribution is lower than the optimal value (see Ref.[114] for Co-doped, Ref. [115, 116] for K-doped and Ref.[117] for P-doped Ba-122). Optimally and over-doped samples resulted in a suppression of superconductivity under external pressure application. Moreover, also the chemical pressure doping shows the same behaviour when combined with substitutional charge doping in $Ba(Fe_{1-y}Co_y)_2(As_{1-x}P_x)_2$ samples [118]. A different behaviour was observed in the aliovalent La-doped Ba-122 with an enhancement of T_c under the application of external pressure [119].
Having these considerations as prerequisites, in principle, the change in the charge density via electrostatic gating could lead to both a SC enhancement (like in the case of La substitution) or suppression (like in the other mentioned cases of optimally doped systems). In fact, electrostatic gating can be considered like a change in the charge density of the Ba layer, since it does not change the composition of the FeAs layer that directly contributes to the conduction. However, we stress that physical and chemical pressure affect the system very differently, even though they both show similar effects on the SC properties. Differences arise primarily from the

fact that P doping and external pressure in Ba-122 affect the Fe-As bond length in a starkly different manner [117, 118].
For all these reasons, the results we obtained were, in any case, not obvious. In fact, from our observation we can conclude that the combined effect of the substitutional doping and the lattice strain - induced by the mismatch of the lattice constants of the film and the substrate -, for a P content of $\simeq 0.2$ in a Ba-122 ultrathin film acts as an optimization of the system for any further changes in the charge density. In other words: the chosen system is already optimized also in the charge density as far as the SC properties are concerned, and behaving qualitatively like those systems where superconductivity was already optimized by substitutional electron doping and subjected to further (chemical or physical) pressure doping. Figure 2.15 gives the figurative idea of this concept. For this reason, further ionic gating experiments on the under-doped and over-doped regions are required to better conclude on the effects of electrostatic gating on SC properties of such systems: in particular, it is reasonable to expect a different behaviour on the under-doped samples that may show an enhancement of the SC properties.
In conclusion, we note that our finding confirms that modifications of the lattice structure are much more effective than the electrostatic charge density modulation induced via ionic gating - coherently with what literature reports about the Ba-122 family [118, 120]. More generally, only in the case of FeSe and $FeSe_{1-x}Te_x$ the external charge doping affects T_c comparably to the substitutional doping [22, 56, 57, 59, 121]. However, notice that, since the perturbation of the charge density is screened by the high native carrier density, the field effect is limited to the surface of the film - even at the highest possible electric field application [85] - and, as we have seen, the modulation of the SC properties spread along all the thickness of the film, and the SC order parameter modification is diluted in the bulk of the sample [27, 86]; thus, the real effectiveness of the ionic gating on the SC properties of such conductive systems could be underestimated, with respect to other methods in which the charge modulation penetrates uniformly on the whole bulk of the system film. Therefore, similar experiments on thinner samples – i.e. one or two unit cells thick – or a theoretical treatment involving the proximity effect are required to finally determine the real possibilities of ionic gating on this system.

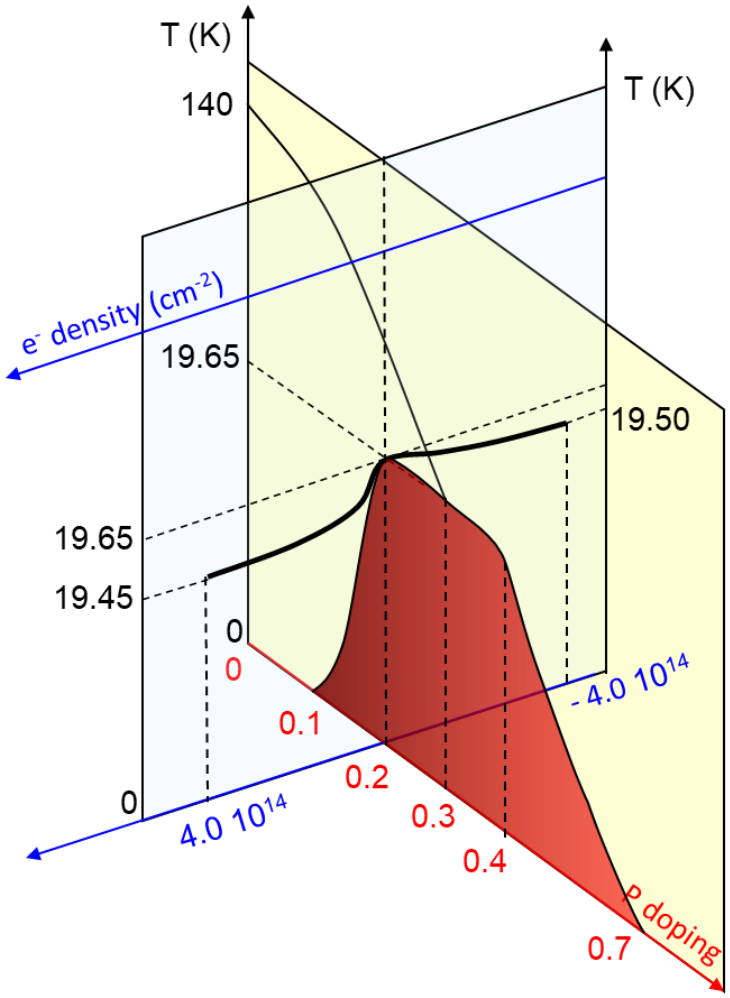

Figure 2.15: The representation of the two orthogonal way of doping the optimally P-doped Ba-122 10-nm-thick film.

Chapter 3

Ionic gating in nanocrystalline Diamond thin films

The interest in fundamental and applicative studies about diamond arises from the fact that intrinsic diamond features significant properties: ultrahigh thermal conductivity, large intrinsic charge carriers mobility, an high breakdown electric field, excellent electrochemical stability, and biocompatibility [122]. Interesting applications can also arise from the use of diamond-based materials for electronic devices. The main challenge, towards this development, consists in turning the diamond into a conductor without degrading its excellent properties. So far, the main way to let diamond to become a conductor, is via the substitution of some carbon atoms in the crystal lattice with boron (B) atoms: this leads to an insulator-to-metal transition and, with further increasing the B content, to superconductivity [123–125]. However, in order to reach good conductivity – and superconductivity -, we need to introduce very large dopant concentrations ($> 10^{20}$ B atoms/cm^3) that are detrimental for the transport properties of pure diamond, both as far as the normal and superconductive states are concerned, because of the introduction of disorder in the crystal lattice [126–129]. Moreover, diamond is also expected to be suitable for high temperature superconductivity, because of its large Debye temperature ($\simeq$ 2000 K); but disorder, combined with the limited solubility of B atoms in carbon atoms, frustrates the SC critical temperature [130–133].
On the other side, it is well known that diamond can show hole-type conductivity at its surface also in other conditions: the cleaved surface of a diamond crystal presents dangling bonds that can be functionalized by hydrogen which, in turn, can form bonds with electron-attracting molecules diffused in the surrounding environment; that could be the case of moisture, when the sample is exposed for several minutes [134–136]. In such cases, the electrons in the diamond valence band move to the bonded molecules, leaving behind a hole-like gas at the diamond surface layer [135, 136]. So far, a lot of fundamental studies [134–141] and applications [142–145] of this surface conducting layer – like high-performance transistors and biosensors –

have come to light.
In this framework, the charge doping induced by the proximity of electron-attracting molecules to the surface of pure diamond is still higher than, or, at least, comparable to what can be obtained by the standard solid gating techniques (both are $\lesssim 10^{13}$ e^+/cm^2). But, as shown in Chapter 1, it is possible to exceed these values when the ionic gating technique is exploited.
For this reason, EDL gating architecture has been extensively exploited on diamond based devices. In particular, insulating systems (single crystals and epitaxial thin films) have been investigated, but neither good metallic behaviour nor superconductivity has been induced [146–149]; most likely because of the rather-low values reached for the induced charge densities in these insulating systems ($\lesssim 7 \cdot 10^{13}$ cm^{-2}). We attribute the poor performances of the ionic gating on these systems to the complete absence of an intrinsic charge density.
For this reason, we designed ionic gating experiments on B-doped nano-crystalline diamond films aiming to exploit the natively present hole-density to reach higher values of charge modulation. Our results were published in Ref. [150].

3.1 Device fabrication

The samples exploited in our experiments were grown by our collaborators at Ulm University.
The growth process of our films is reported in Ref. [151]. In order to grow nanocrystalline diamond (NCD) films, two steps of chemical vapour deposition (CVD) were performed on AF32eco (Schott, Mainz, Germany) high temperature glass substrates. The chosen substrates guarantee that no delamination or fracture occur to the diamond thin films for the thermal expansions that the devices undergo during the procedure [152]. The substrates were sonicated in acetone and ethanol for 5 min; subsequently, they were submerged in "piranha" solution (H_2SO_4 and H_2O_2 in 2:1 ratio) for 10 min to make the surface highly hydrophilic due to the presence of hydroxyl groups. Then the substrates were seeded with a dense layer of diamond nanocrystals by dipping them into a nano-diamond (4–6 nm) suspension, and exposed to a Micro Wave (MW) CVD treatment (1.3% CH_4 in H_2 atmosphere, under a pressure of 1.4 kPa, substrate temperature of 610°C, exposure time 10 min) to improve the adhesion of the nanocrystals to the substrate. Then, the first CVD step was performed in a Hot Filament reactor (chamber pressure 2 kPa) to obtain a $\simeq 1\mu m$ intrinsic NCD (iNCD) layer. This layer serves as a bases for the second CVDstep where the B-doped NCD film is grown. In fact, the relatively big diamond crystallites (few hundreds of nm sized) present in the first iNCD allow the B-doped layer to grow in a more orderly fashion, reducing the number of defects and enhancing the carrier mobility [151]. The second CVD step grows a $\simeq 300$ nm layer of B-doped NCD on top of the iNCD. It is performed in a dedicated MW

reactor (Astex AX3120) at a pressure of 30 Torr, using a MW power of 600 W and setting the H_2 and the CH_4 fluxes at 200 and 3 sccm respectively, for an exposition time of 60 min; an 8 cm wide boron ring is placed into the plasma as a solid source of boron-doping.
As-grown NCD samples were characterized by atomic force microscopy (AFM), X-ray diffraction (XRD), Raman spectroscopy, and Hall effect.
Contact mode AFM experiments were performed to have information about the morphology of the sample surface. Figure 3.1 shows a 5 μm $\times$ 5 μm area of the sample: it is polycrystalline; the grains have an average lateral size of 222 ± 15 nm and the largest grains appear to have a rectangular or triangular shapes, that are associated in the literature to the [100] and [111] –oriented facets of the of the diamond crystal structure [153]. From the topography map analysis we obtained the

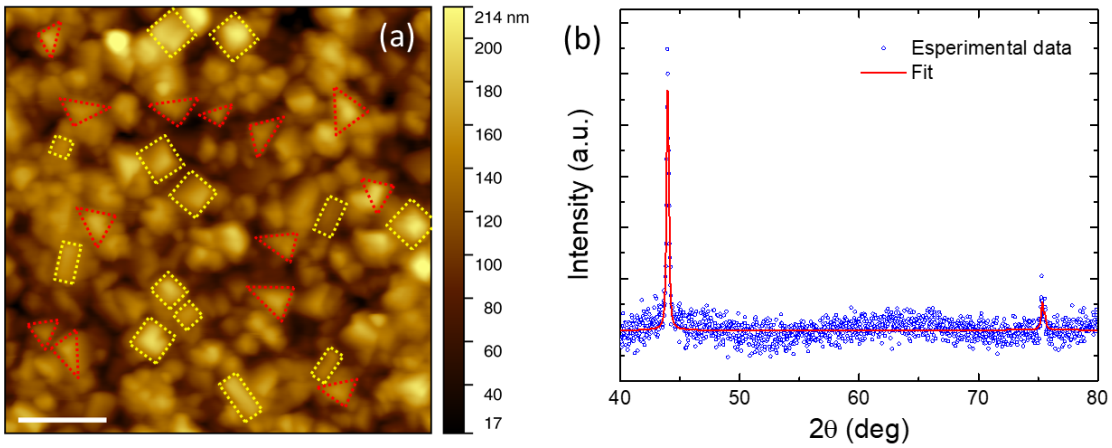

Figure 3.1: (a) AFM topography map of a $5\mu m \cdot 5\mu m$ area of the Boron-doped layer acquired in contact mode. Rectangular shapes (dashed yellow lines) suggest the presence of [100]-oriented facets; triangular shapes (dashed red lines) suggest the presence of [111]-oriented facets (see Ref. [153]). The white scale bar is $1\mu m$. (b) XRD spectrum (blue hollow dots) and fit to the data performed using MAUD [154] (solid red line). (Panel (a) is adapted from Ref. [150]).

average mean square roughness of the sample surface ($S_q = 32.3 \pm 0.5$ nm) and the rugosity - i.e. the surface real area of the sample divided by the surface projected area – ($f_r = 1.08 \pm 0.02$).
XRD spectra were measured using a Panalytical X'Pert Pro Diffractometer in Bragg-Brentano configuration (Cu Kα X-Ray source). Figure 3.1.b shows the XRD spectrum of a sample after subtraction of the polynomial background mostly due to the amorphous substrate. The spectrum shows the two expected peaks

at $2\Theta = 43.96°$ and $2\Theta = 75.35°$, corresponding to the [111] and [220] crystallographic orientations of the diamond lattice respectively [155], with a clear predominance of a preferred orientation along the [111] crystallographic direction. We can have an estimate of the grains size from a quantitative analysis of the spectrum by the Schrerrer's equation [156]: the result is an average crystallite size $S_q \simeq 38.3 \pm 4.3$ nm that is in accordance with the AFM analysis. Micro-Raman measurements were performed with a Horiba Jobin Yvon HR800 spectrometer at 532 nm, with a 1800 lines/mm grating and a spectral resolution ~ 2 cm^{-1}, coupled to the 100x objective of an Olympus BX41 confocal optical microscope. We acquired a Raman spectrum for three different points of our sample surface: each spectrum results from the averaging of 5 different acquisitions with an integration time of 1 s. As shown in figure 3.2, the spectrum after background subtraction shows

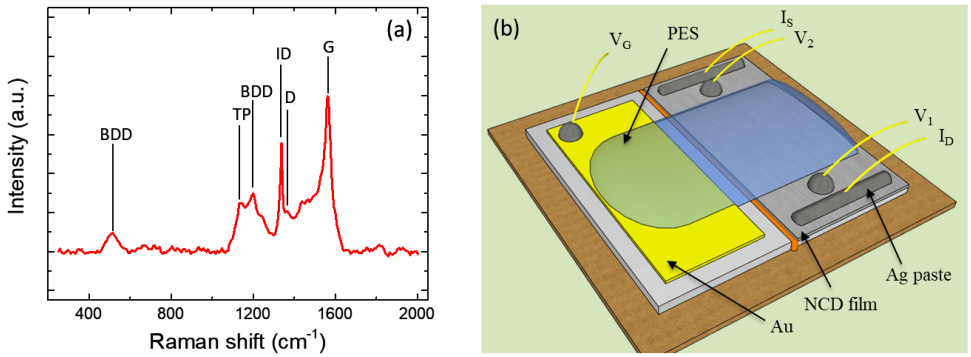

Figure 3.2: (a) A representative Raman spectrum at 532 nm of a B-doped NCD film. The two BDD peaks (at ~ 500 cm^{-1} and at ~ 1200 cm^{-1} stem from the boron-doped diamond phase; the ID peak (at ~ 1337 cm^{-1}) is associated to the first-order intrinsic diamond Raman peak; the G peak (at ~ 1565 cm^{-1}) and the D peak (at ~ 1360 cm^{-1}) arise from graphitic phases; the TP peak (at ~ 1135 cm^{-1}) is associated to the presence of trans-polyacetylene. (b) The complete device for EDL experiments is sketched: notice that the silver paste is strictly kept away from the PES in order to avoid electrochemical interactions between them. (Panel (b) is adapted from Ref. [150]).

a series of peaks and bands associated to polycrystalline diamond, boron inclusion, and non-diamond carbon phases arising from grain boundaries and interfaces [151]. Specifically, the peak at ~ 1337 cm^{-1} corresponds to the first-order Stokes peak related to the intrinsic diamond phase [157]; it arises from the undoped diamond layer. Boron doping itself results in the bands observed around $\sim$500 cm^{-1} and $\sim$1200 cm^{-1} [158]. Defective graphitic phases give rise to the broadened G band at ~ 1565 cm^{-1}, as well as the D peak at $\sim$1360 cm^{-1} [151]. Finally, the peak around ~ 1135 cm^{-1} is due to the presence of trans-polyacetylene at grain boundaries and

interfaces [159].
Hall effect experiments were performed to estimate the B content: with applying a magnetic field up to B = ±0.7 T at room temperature, we measured the Hall resistance in the Van der Pauw configuration. The resulting positive carrier density was calculated in $n_h = 3.2 \pm 0.5 \cdot 10^{20}$ e^+/cm^3, that corresponds to a Boron concentration of $0.36 \pm 0.06\%$, that is consistent with what expected from the growth process [151]. After this preliminary characterization, the diamond film was diced into smaller rectangles ($\sim$ 0.7 cm long, 0.3 cm wide) with a diamond blade, which were then individually fixed on the sample holder for low-temperature transport measurements (see figure 3.2b). A microscope glass of the same thickness of the substrate (200 μm) was placed on the side, and the small gap between the two was sealed by applying and UV-curing a small amount of liquid polyimide. Electrical contacts for source (S), drain (D), and four-wire voltage probes (V_1 and V_2) were realized by drop-casting a small amount of conductive silver paste. A thin gold leaf was placed on the glass slide on the side of the device to act as a counter electrode for gate voltage (V_G) application.
Finally, the liquid precursor of the PES was drop-casted, covering the sample area between V_1 and V_2 - i.e. the active channel of our device - and the gold leaf on top of the side glass. Since our B-doped NCD films showed a strong resistance to chemical agents, we choose a well-established ionic medium for the gating: the PES we used consisted of a mixture of BEMA dimethacrylate oligomer (bisphenol A ethoxylatedimethacrylate, average $M_w \sim 1700$ Da, Sigma Aldrich) and EMIM-TFSI ionic liquid (1-Ethyl-3-methylimidazolium bis(triuoromethylsulfonyl)imide, Sigma Aldrich) in 2:8 ratio along with 3 wt% of free radical photo initiator (DAROCUR 1173). After drop-casting, the liquid precursor was subsequently UV-cured; both the PES drop-casting and the UV exposure were carried out in the controlled atmosphere of a dry room. The complete device was then rapidly installed on the cold finger of a Cryomech® pulsetube cryocooler for electrical measurements, where it was left to degas in high vacuum (base pressure $\lesssim 10^{-5}$ mbar) for at least 1 hour to remove residual water molecules absorbed by the PES.

3.2 EDL gating experiments

We performed four-wire resistance (R) measurements by sourcing a DC current of the order of few μA with an Agilent B2912 source measure unit (SMU) and by measuring the voltage drop with an Agilent 34420 nano-voltmeter. We operated an inversion of the current sign at each step - and then we averaged the two resistance values obtained - in order to remove the common mode signals: such as the thermoelectric force and the parasitic currents. Referring to figure 3.2, we used the side gate configuration by applying negative V_G down to -15 V, with the second channel

of the same Agilent B2912 SMU at 240 K; this specific temperature is the working temperature of the PES we used, that is defined as the lowest temperature before the ion mobility starts decreasing and the PES freezes (see the inset in figure 3.2); the PES is polarized at the lowest possible temperature to reduce the probability of electrochemical interactions. For each V_G value, we measured the resistance in the temperature range between the PES working point (i.e. 240 K) and the base temperature of the cryocooler (i.e. 2.9 K).
We performed a step-like application and removal of V_G, followed by the fitting of the experimental gate current (I_G) - according to double step chronocoulometry (DSCC) models we presented in Chapter 1 - to obtain the total charge Q_{EDL} accumulated on the film surface due to the EDL formation; the surface induced charge density is then obtained as $\Delta n_{2D} = Q_{EDL}/(f_r \cdot S)$, being S the film area covered by the PES and f_r the rugosity of the film, that we obtained by AFM analysis.

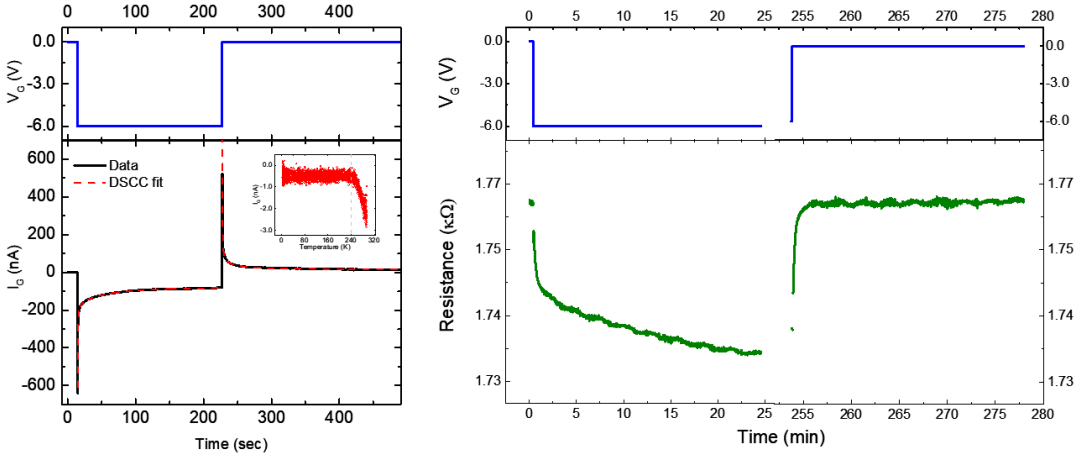

Figure 3.3: (a) The DSCC analysis in the case of $V_G = -6$ V applied. In the inset: I_G as function of temperature: the glass temperature of the PES is highlighted by the diminishing of I_G down to 240 K. (b) Modulation of the resistance at the application and removal of $V_G = -6$ V.

Our system is likely to be electrochemically stable. Indeed, boron-doped diamonds are currently used as inert electrodes in electrochemical cells for voltammetry measurements [160]. However, the electrochemical stability window reduces with increasing the boron content of the doped diamond crystals [160].
In our setup, due to the rather significant B content of our samples, we expect the electrochemical stability window of the PES/sample interface to be around $V_G \approx 5.0 - 7.0$ V [161]. These expected values are in good agreement with our experimental results which shows no sign of electrochemical reactions down to V_G = -6 V, but it gives some hint of PES degradation when applying V_G = -15 V.

In any case, the sample integrity is always preserved, and the initial performances can be restored by simply rinsing the sample in acetone and ethanol to remove the residual PES.
Other sources of doping, e.g. intercalation or constant lattice modifications, are extremely unlikely to occur, since the robustness of the sp^3 diamond bonds.
The electrostatic nature of the process is thus guaranteed by the reversibility of the effects on the resistance (as shown in figure 3.3), by simply removing the applied V_G at 240 K; thus, we can assure that the gating effect is electrostatic.
We studied the resistance modulation as function of Δn_{2D}. Figure 3.4.a presents the normalized resistance variation, defined as $\Delta R/R' = [R(V_G) - R(0)]/R(V_G)$, as function of Δn_{2D}; notice that the values obtained for Δn_{2D} are more than three times higher than what reported in the literature so far [146–149, 162, 163]; the negative slope indicates that the conductivity occurs via hole carriers, as expected, since the application of $V_G > 0$ suppresses the conductivity, while $V_G < 0$ enhances it. The linearity instead confirms that the doping is dominated by electrostatic charge accumulation (non-linear terms are often associated with effects that go beyond the electrostatic ones). We thus concentrate on negative V_G values.
We notice that for $\Delta n_{2D} \gtrsim 2 \cdot 10^{14}$ e^+ cm^{-2} we lose the linear dependence of $\Delta R/R'$. This can be explained by considering that those points correspond to the application of $V_G > 10$ V: for such high values, in order to not to induce electrochemical reactions, we rapidly cooled down the system after the application of the gate voltage (as described in [164]); consider that in the other cases we waited a time of $\sim$ 10 minutes needed for the resistance modulation to stabilize (see figure 3.3).
The resistivity increases with decreasing the temperature (see figure 3.4). Moreover, the effect of the hole accumulation due to ionic gating slightly reduces its value in the whole temperature range, while it is not strong enough to drastically change its behaviour. At a first glance, the resistivity behaviour can be associated to a semiconducting regime, but a zoom in the low temperature range of the conductivity $\sigma(T)$ (see the inset of figure 3.4) shows that, at $T \sim 8K$, it tends to saturate to a finite value: that is the fingerprint of a granular metallic regime [165–167]. More specifically, we notice that in the log-log scale, at high temperatures, $\sigma(T)$ follows a well-defined power law $\propto T^{\beta}$ with $\beta \simeq 0.25 \pm 0.10$, that can be associated to a quantum critical (QC) metallic regime on the metallic side of the metal-insulator-transition (MIT) in granular systems [165–167]. Actually, this behaviour is consistent with what we could expect from the native carrier concentrations determined by the Hall effect: in fact, in NCD systems the MIT is reported to occur at a doping level of $\approx 2 \cdot 10^{20}$ e^+/cm^2 [151, 168], while, our Hall measurements stated a native hole concentration of $n_h \simeq 3.2 \cdot 10^{20}$ e^+/cm^2, i.e. slightly above the MIT.
Thus, we can conclude that the bulk conductivity is decreasing with temperature with a well-defined power law, and, even the at highest levels of doping we could reach, the T-dependence of σ remains unaffected. However, it is possible to focus

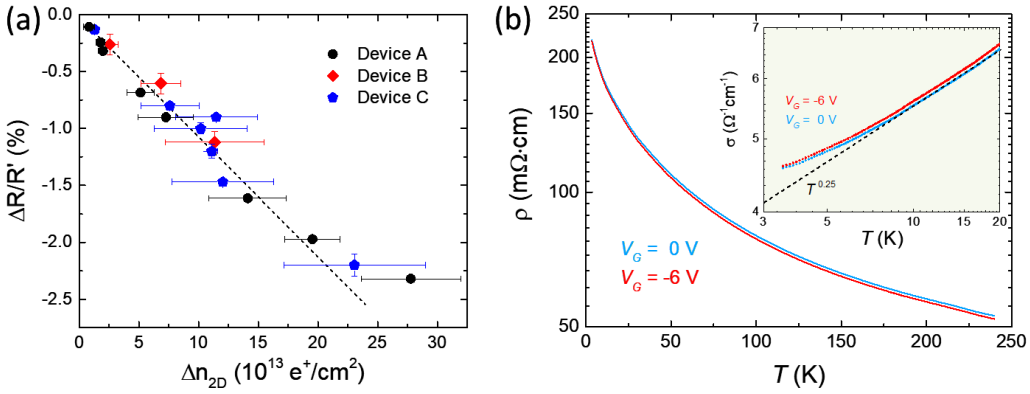

Figure 3.4: (a) $\Delta R/R'$ for three different samples as function of the surface induced charge density Δn_{2D}. The error bars take into account the difference in the values obtained for ΔR and Δn_{2D} during the application and removal processes. The dashed line is a guide to the eye. (b) The bulk resistivity ρ of the sample for two different values of V_G. In the inset: the same data are shown as conductivity σ versus temperature; a zoom for low temperatures shows the saturating behaviour of σ. (Adapted from Ref. [150]).

on the effects on the surface conductivity by exploiting the method reported in Ref. [59]. We define the differential sheet conductance of the accumulation layer (AL) at the interface with the PES as:

$$\sigma_{AL}(T)|_{V_G} = \sigma_s(T)|_{V_G} - \sigma_s(T)|_{V_G=0} \tag{3.1}$$

Where $\sigma_s(T)|_{V_G}$ and $\sigma_s(T)|_{V_G=0}$ are the sheet conductance of the film at finite V_G and $V_G = 0$ applied, respectively.
Since σ_{AL} is the difference between the modulated and the native conductances, it will be small (because, as we have seen the modulation of the resistance is small with respect to the resistance value). This means that even the tiniest differences in the thermal link between one measurement and another will bring to high noise in σ_{AL}; to overcome this issue, for each thermal cycle with a finite V_G applied, we performed two another cycles with $V_G = 0$ before and after it; we then averaged these last two obtained signals before subtracting them to the $\sigma_s(T)|_{V_G}$. Mathematically speaking, σ_{AL} is better defined as:

$$\sigma_{AL}(T)|_{V_G} = \sigma_s(T)|_{V_G} - \frac{\sigma_s(T)|^{before}_{V_G=0} + \sigma_s(T)|^{after}_{V_G=0}}{2} \tag{3.2}$$

Figure 3.5 presents the differential conductance at the AL, σ_{AL}, for different values

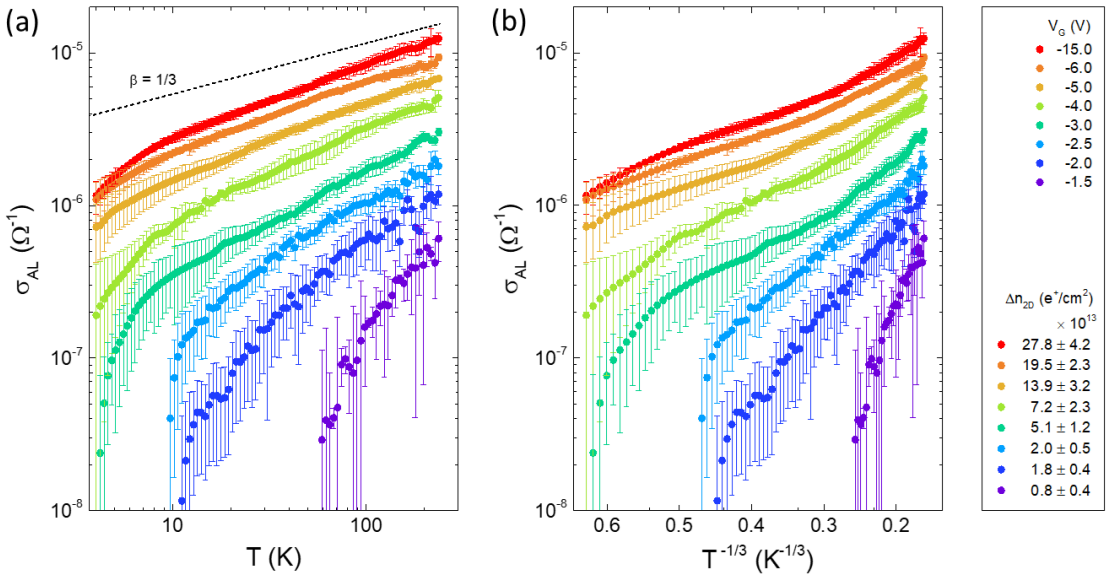

Figure 3.5: (a) The differential sheet conductance σ_{AL} as function of temperature in the double logarithmic scale (a) and in a semi-log scale plotted vs. $T^{-1/3}$ (b). The left panel highlights that the conductance remains below the MIT transition (black dashed line; $\beta = 1/3$); the right panel shows the linearity of the curves with $\Delta n_{2D} \lesssim 2.0 \pm 0.5$ e$^+$/cm^2 in the semi-log scale plotted vs. $T^{-1/3}$. (Adapted from Ref. [150]).

of V_G and, hence, Δn_{2D}. Notice that σ_{AL} drops to zero in the three lowermost curves, that correspond to the lowest doping levels and a $\Delta n_{2D} \lesssim 2.0 \pm 0.5$ e$^+$ cm^{-2}; for higher Δn_{2D} values, σ_{AL} approaches a finite value even in the limit of $T \to 0$. Moreover, the scaling behaviour is noticeably different in the two groups: the red-to-green curves scales well with a power law behaviour, for $T \gtrsim 8$ K:

$$\sigma_{AL} \propto T^{\beta} \tag{3.3}$$

with $\beta > 1/3$ (i.e. the curves are below the one with $\beta = 1/3$; see figure 3.5.a); while the light-blue-to-violet curves, instead, follows an exponential behaviour of the form:

$$\sigma_{AL} \propto exp(-B/T^{1/x}) \tag{3.4}$$

with $x = 3$ (i.e. they are linear in a semi-log plot vs. $T^{1/3}$; see figure 3.5.b).
The two dependences stand for two different conducting mechanisms. As a matter of facts, the power-law dependence indicates that the NCD film at the AL is not insulating. However, differently from the bulk conductivity, in this case σ_{AL} drops to zero for $T \lesssim 8$ K, and β is always larger than 1/3 ($\beta = 1/3$ is observed at the

quantum-critical-point of the MIT [165–167]). Thus, we can conclude that the AL is, for the highest doping values, in the quantum critical regime – as in the case of the bulk conductance – but slightly on the insulating side of the transition.
The other group of curves instead, namely, for a surface charge doping of $\Delta n_{2D} \lesssim 2.0 \pm 0.5$ e^+ cm^{-2}; for higher Δn_{2D}, drop to zero faster than any power law. We are thus far from the QC regime, well inside the insulating side of the MIT, and the conductance occurs via a Mott variable range hopping (VRH) in 2D, whose hallmark is exactly an exponential behaviour of the form of equation 3.4 with $x = 3$ [167, 169, 170].
These results are reasonable, since we expect that the induced charge density is confined within few atomic layers and such hole-doped layer is most likely to behave as a quasi-2D system; at the same time Coulomb interactions are not expected to be significantly involved in the conduction mechanism [128]. Moreover, the data greatly deviate from a possible Mott VRH in 3D (that would scale with $x = 4$) as well as from an Efros-Shklovskii VRH in presence of a Coulomb gap (that would scale with $x = 2$).

3.3 Discussion and conclusion

We have shown that the B-doping in NCD films let us reach values for the induced charge density at the surface that are ∼3 times higher than the maximum achieved in the literature for undoped diamond [146–149, 162, 163]. This result arises from the increased EDL capacitance of the material thanks to the presence of a native concentration of hole carriers that provides an easier modulation of the charge density. However, even at the highest surface induced-charge modulations, we could not detect any sign of superconductivity down to $\sim$ 3 K; and the sheet conductance in the surface accumulation layer remains far below (more than $\sim$ 10 times smaller) than what reported in non-granular diamond systems like undoped epitaxial films or single crystals [146–149]. Finally, we have seen that the AL is led from a VRH insulating behaviour to a QC regime, but it never crosses the MIT, while the bulk of the system lies on the metallic side of the MIT and shows a QC regime for granular metallic systems.
Thus, the behaviour of the AL conductance cannot be explained by only considering the presence of grain boundaries. In fact, it is well known that the effect of the ionic gating on diamond is strictly confined within a surface layer that can penetrate only a few atomic layers on the bulk [27, 103, 171, 172]; on the other side, we have seen from the AFM topography that the roughness of the film surface is $\gtrsim$ 30 nm, well beyond the thickness of the AL, with local valleys that can even reach $\gtrsim$ 100 nm in depth. Thus, the effect of the ionic layer is to form a pattern of islands with an enhanced carrier density, on top of the film surface, that are not necessarily connected one to the other – except the connection between them that occurs via

percolation through the conductive bulk underneath. Thus, the disorder at the surface is greatly enhanced with respect to the bulk, and thus the doping needed to cross the MIT at the surface is strongly shifted to higher levels, with respect to the ones we reached.
It is possible to investigate more deeply the conducting mechanism by exploring the β and B parameters that appear in equations 3.3 and 3.4 as function of Δn_{2D} - those results are graphically presented in figure 3.6.

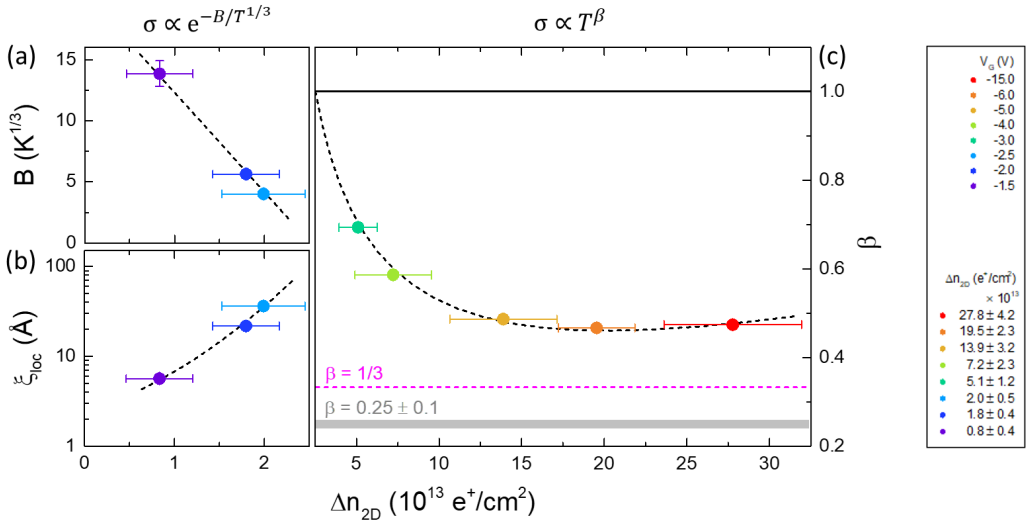

Figure 3.6: The dependence of the B parameter (a), the localization length (b) and the β parameter (c) that appear in equations 3.4, 3.3 and3.5, as function of Δn_{2D}. The black dashed lines are guide to the eye; the magenta dashed line and the black solid line represents the β values at which the MIT and the Mott-VRH-to-QC-regime transition respectively occur; the gray band represents the β value for the bulk conductivity. (Adapted from Ref. [150]).

The B parameter that appears in equation 3.4, refers to the behaviour of the σ_{AL} in the Mott VRH regime. It is explicitly expressed as:

$$B = 3/k_B N(E_F)\xi_{loc}^2 \tag{3.5}$$

and it depends on the 2D-DOS of the system and on the localization length ξ_{loc}; while k_B is the Boltzmann constant. In order to have information about ξ_{loc}, we considered that the 2D-DOS for a parabolic band at the Fermi level is $N(E_F) = m^* m_0/\pi\hbar^2$, where $\hbar$ is the reduced Plank constant and m_0 the electron mass. We assumed the effective mass m^* of diamond to be $\simeq 0.8$ with a good degree of approximation, according to Ref. [173–175]. The results we obtained for ξ_{loc} are

plotted vs. Δn_{2D} in figure 3.6.b: notice that, for the lowest level of doping, ξ_{loc} is reasonably close to the B-doped Diamond Bohr radius (i.e. 3.5 Å), as we could expect from Ref. [128]. We can also linearly extend the black dashed line in figure 3.6.b to higher doping values in order to intercept the first doping concentration that leads to a QC behaviour (namely, the green point in figure 3.6.c, which corresponds to a $\Delta n_{2D} = 5.1 \pm 1.2\ e^+/cm^2$: doing so, we obtain a localization length $\xi_{loc} = 30 \pm 20$ nm. This suggests that the system exits from the Mott VRH insulating regime when the localization length approaches the surface roughness of the film. In other words, the AL conductance approaches the QC regime when the ξ_{loc} exceeds the length scale that describes the disconnections due to the disordered nature of the film surface.
The analysis of the β parameter that appears in equation 3.3 leads to interesting conclusions as far as the QC regime is concerned. The β scaling factor is well studied in the literature, and its value strictly describes the transport mechanism of a disordered system close to the MIT transition. Referring to [165–167], the VRH-to-QC regime transition occur for $\beta = 1$; for higher values we are deeply in the VRH regime, while diminishing β we approach the MIT transition. This last is reached at $\beta = 1/3$: in this case the conductance maintains the power-law dependence even for $T \to 0$ without dropping to zero – like in the insulating side of the MIT – or saturating – as it is in the metallic side of the MIT. Figure 3.6.c illustrates the values of β for each measurement at different V_G: as we have seen, the surface conductance remains in the QC regime even at the highest values of V_G, additionally, here it is possible to appreciate that β decreases, with increasing Δn_{2D}, down to $\simeq 0.44$, then it saturates, suggesting that even a further increase in the Δn_{2D} would not lead to the crossing of the MIT. This behaviour can be ascribed to the introduction of additional scattering centres at the interface with the electrolyte due to the gating process itself [92, 94–96, 176]: such an increase in the surface disorder is known to induce a re-entrant MIT at the surface of extremely-sensitive systems [108, 110]. The result is that the MIT transition is shifted to higher values of doping, and any further increase of V_G does not reach the aim of crossing the Anderson transition.

Chapter 4

Field effect gating in ink-jet printed graphene and MXene films

4.1 Introdution

Flexible electronics is an ever-growing field in the last decades, mostly fuelled by the unceasing demand of the technological needs of our everyday life: from energy storage to internet of things, through wearable and futuristic devices.
Flexible devices can operate passively, in sensing the environment, actively, as actuators, or by integrating the two functionalities in adapting their response to the external conditions.
In order to realize flexible devices for the most diverse tasks, researchers elaborated several methods: in some cases, the material of interest is reduced to yarns or fibres and is weaved into the frame of the desired cloth, in other cases the designed material is directly printed on the supporting stretchable substrate [177].
Nowadays, printing processes have been extensively developed and are currently exploited to fabricate reliable devices in the widest range of electronics: thin-film-transistors, photovoltaic cells, micro-supercapacitors and different optical devices are only few of them [178–180].
A very convenient way to produce wearable electronics is the inkjet printing of proper inks, thanks to the ease of designing, the reduction of fabrication steps, the cheaper costs and the scalability of production of the printed devices.
Research efforts are, thus, focusing on the production of suitable inks, depending on the specific demand, that could show the necessary fluidic properties along with the required electronic performances.
In parallel, in recent years, an increasing number of studies about 2D and quasi-2D materials have came to light. These relatively-new advanced materials are characterized by interplanar Van Der Waals forces: the breaking of these bonds leads

to the exfoliation of the material itself. This property is particularly suitable for producing thin film inkjet printed devices [179].
Among 2D materials, the first, and most studied material is by far graphene: the allotropic form of carbon that presents the sp^2 hybridization and shows a planar, hexagonal geometry. The interest in graphene inkjet printed circuits arises primarily from the possibility of exploiting the exceptionally high electron mobility (up to 10^6 cm^2 V^{-1} s^{-1}) of graphene in the making of electronic devices like thin-film-transistors (TFT) [181]. Moreover, its mechanical stability and bendability along with the exceptional optoelectronic properties extends the range of possible applications of graphene inks [179].

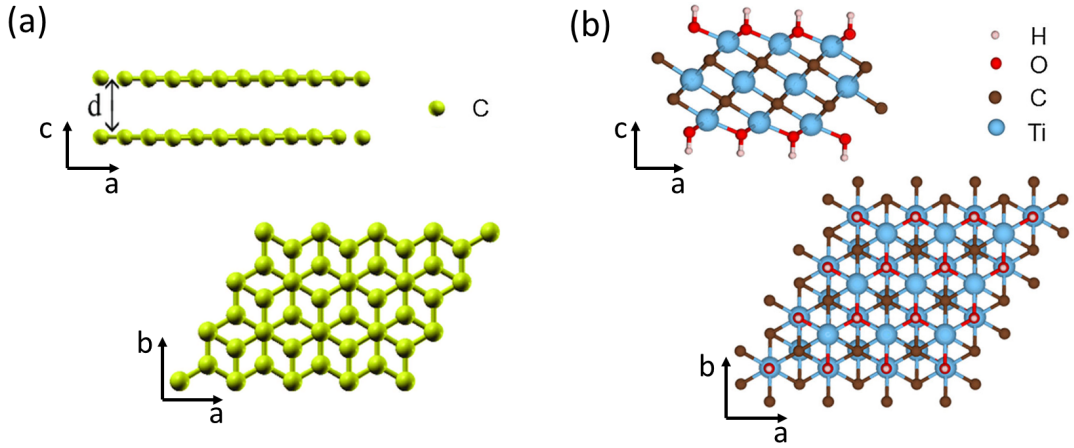

Figure 4.1: Crystallographic structures of a Bernal stacked bi-layer graphene (a) and a $Ti_2C_3T_x$ terminated with OH functional groups (b). Figures are adapted from Ref. [182] and Ref. [183].

Furthermore, graphene inks paved the way to other 2D materials to be used as inks for printing. Hexagonal boron nitride (hBN) inks have been used to build printed heterostructures: Carey *et al.* presented all-inkjet-printed graphene TFTs on polyethylene terephthalate (PET) where an hBN layer is stacked on the graphene ink channel acting as a dielectric between the channel and the silver ink counter-electrode [181]. Inkjet printed devices using transition metal dichalcogenide (TMD) inks – namely: MoS_2, WS_2, $MoSe_2$ and WSe_2 - have been studied to demonstrate the modulation of their conductivity upon ionic gating [184]. Finally, micro-supercapacitors made of metallic MXene inks – MXenes are layered structures consisting of a transition metal (M) and carbon or nitrogen (X) - were demonstrated by Zhang *et al.* [180].
However, for most of these printable inks, we noticed the lack of a complete characterization of their transport properties.
This chapter is aimed at exploring the transport properties of two different inks:

liquid phase exfoliated (LPE) graphene and LPE MXene – specifically Ti_3C_2 - printed on Si/SiO_2 substrate. While measuring the temperature dependence of the conductivity, we exploited the substrate configuration to perform solid-gate field effect experiments; thus, we obtained the mobility and the charge density for both, the graphene- and MXene-ink films. In both cases we unveiled a characteristic disordered behaviour. Magnetoresistance measurements confirmed the as-obtained results and helped giving a mesoscopic characterization of transport in these systems.

4.2 Inks preparation

The samples were prepared in the Cambridge Graphene Centre (University of Cambridge, UK) by Dr. Adrees Arbab. The preparation process for the graphene inks is described in Ref. [181], while for the MXene inks is reported in Ref. [180]. To print the devices, we used a drop-on-demand (DoD) Fujifilm Dimatrix DMP-2800 inkjet printer equipped with a Fujifilm DMC-11610 nozzle ($\oslash = 21\ \mu$m); the single droplet volume reaches ~ 10 pl; the maximum ejecting frequency used is 2 kHz; the printing process always occurred at room conditions.
In the formulation of the ink, there are four parameters to control: the diameter a of the nozzle installed in the printer (in our case $a = 21\ \mu$m), the density of the suspension ρ (g/cm^3), its viscosity η (mPa s), and its surface tension γ (mN/m). All those values go into the definition of some dimensionless numbers that are reported to be good parameters establishing the printability of a suspension. The most used ones are: the Reynolds number ($\mathrm{Re} = v\rho a/\eta$), the Weber number ($\mathrm{We} = v^2\rho a/\gamma$), the Ohnesorge number ($\mathrm{Oh} = -\eta/(\gamma\rho a)^{1/2}$ and, its inverse, Z ($Z = 1/\mathrm{Oh}$). These numbers are referred to as figures of merit (FOM). In the literature, a good value for Z is $2 < Z < 24$ [181]. Often, in DoD printers, $Z > 2$ is required in order to obtain single-drop casting [178]. Exceptions are common occurrences, depending on the solution formulation and on the used solvents [178].
The inks used in the work presented here are obtained by liquid phase exfoliation (LPE) of graphite flakes (10 mg/ml, Sigma-Aldrich No. 332461, $< 100\ \mu$m size) and Ti_3AlC_s MAX phase crystals.
The choice of the solvent is of utmost importance both for the printability of the ink and the electrical properties of the printed circuit. Often, the rheological properties of the solution are optimized for the jettability of the ink by the use of additive surfactants/polymer stabilizers; however, these agents contaminate the material hampering its performances. N-Methyl-2-Pyrrolidone (NMP) do not need to be stabilized, however its toxicity and its high boiling point (>100° C) render it difficult to get rid of the remaining solvent on the printed circuit. Thus, a common choice is a mixture of two different low boiling point (<100° C) solvents; but, again,

the difference in the evaporation rate between the two solvents can lead to rheological instabilities. Depending on the cases, a smart solution has to be found.
In the case of graphene exfoliation, we followed a double step process: the desired solubility of the graphene flakes was reached in a NMP solution by sonication for 9 h (Fisherbrand FB15069, Max power 800W); then the NMP was exchanged with ethanol, to guarantee no solvent left after the printing and evaporation processes. Finally, to remove the thickest graphene grains, the ethanol suspension was ultra-centrifuged (in a Sorvall WX100 centrifuge equipped with a TH-641 swinging-bucket rotor) for 1 hour at 10000 rpm; we then collected the top 70% of the suspension, and wasted the rest. The resulting graphene ink has rheological parameters that are comparable with what reported in Ref. [181]; namely, a density $\rho_{GR} \sim 0.8$ g/cm^3, a viscosity $\eta_{GR} \sim 1$ mPa s, and a surface tension $\gamma_{GR} \sim 30$ mN/m that results in $Z \sim 22$, in the range of optimal jettability [181].
We also expect a logarithmic distribution of the grains size ($S = \sqrt{xy}$, with x and y being the average length and width of the flakes) and thickness (t_f) [181]. AFM

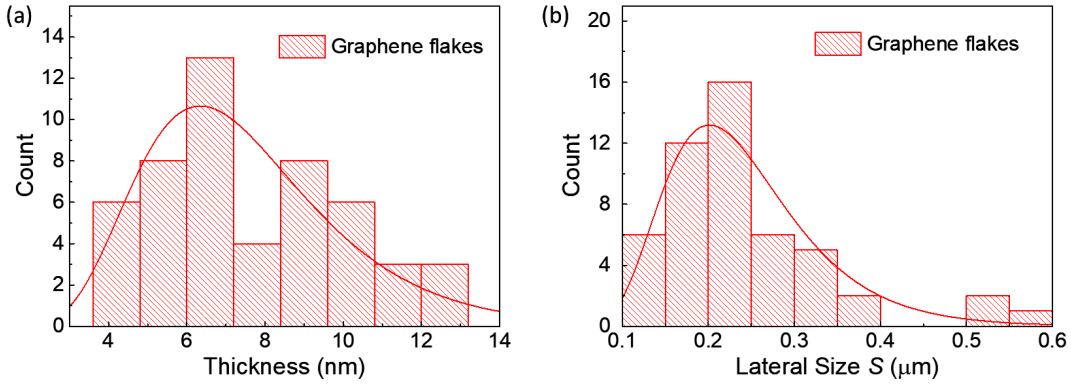

Figure 4.2: Graphene flakes distribution with respect to the thickness (a) and the lateral size (b) of our inkjet-printed devices.

measurements reports an average lateral size $S \simeq 0.21$ μm and an average thickness per single flake $t_f \simeq 6.2$ nm respectively that, in turn, means the graphene flakes are far from being single- or few-layer but, in fact, they are ~ 15 layers thick.
To prepare the MXene inks, we started from Ti_3AlC_3 MAX phase bulk crystals. A first minimally intensive layer delamination (MILD) process – a process that comprises the hand shaking of pristine MAX bulks in weakly acid solution [185] – is used to exfoliate the MXene nanosheets: this process guarantees the low content of defects and the high quality of the flakes. Water swells the multi-layered structures and a following vigorous shaking of the solution delaminates the grains into single- or few-layer flakes.

This first step is followed by several washing steps. To do so, the so-obtained aqueous solution is centrifuged and the sediments are collected for further dispersion in water. This process is repeated for up to three times in order to remove any trace of acid in the solution.
Then we transferred the MXene nano-sheets in NMP solvent. The solvent transfer is obtained by centrifuging the aqueous solution for 1 h at 10000 rpm and then decanting the aqueous solvent; NMP is subsequently added and the as-made solution is sonicated in order to further delaminate and disperse again the flakes uniformly. Then, the solution is centrifuged again for 30 minutes at 5000 rpm in order to precipitate the thicker grains; subsequently the supernatant solution is collected before undergoing sonication again.
In the choice of the solvent to use in the ink we considered that a high polarity solvent is needed to delaminate the material and to guarantee a good stability of the MXene dispersion that, otherwise, undergoes spontaneous reassembling. However, due to the fact that annealing at high temperatures to remove the residual solvent is not permitted since the ease of the MXene sheets to oxidize, we had to choose a low-boiling-point (often with low-medium polarity) organic solvent to form the ink. Thus, we transferred the exfoliated MXene from NMP to ethanol. The transfer is performed in a similar fashion as the former one. Finally, the concentration of the dispersion is controlled by adding solvent.
The as-obtained inks are ready to be printed. The MXene flakes are predominantly single or few layered.
After the ink production, we realized several devices by directly printing the desired pattern on a Si/SiO_2 substrate. The desired Hall-bar geometry resulted from the printing of the central channel followed by the printing of the perpendicular paths dedicated to the connection with the voltage contacts.
Figure 4.3a shows the Raman spectrum for the as-printed graphene-ink device measured with a Renishaw 1000 InVia micro-Raman spectrometer.
The D ($\sim$ 1350 cm^{-1}), D' ($\sim$ 1610 cm^{-1}) and D+D' ($\sim$ 2955 cm^{-1}) peaks indicate the presence of disordered graphene: this result is highly expected since the ink-jet printed film itself is made of a disordered cluster of graphene flakes. Indeed, disorder can arise from the presence of impurities, defects, edges and amorphous carbon.
The D, G, and 2D peaks are associated to in-plane vibrational modes. The G peak ($\sim$ 1580 cm^{-1}) is associated with the bulk-graphene in-plane longitudinal optical (LO) mode. The 2D peak ($\sim$ 2695 cm^{-1}) is a peculiar feature of the graphene Raman spectrum. Even though it is associated with an in-plane vibrational mode, it depends on the number of graphene layers N, since it is strictly connected with the electronic structure of graphene, which depends on N [186]. The D, G and 2D peaks in our spectrum indicates that graphene grains are made of electronically decoupled layers [181].

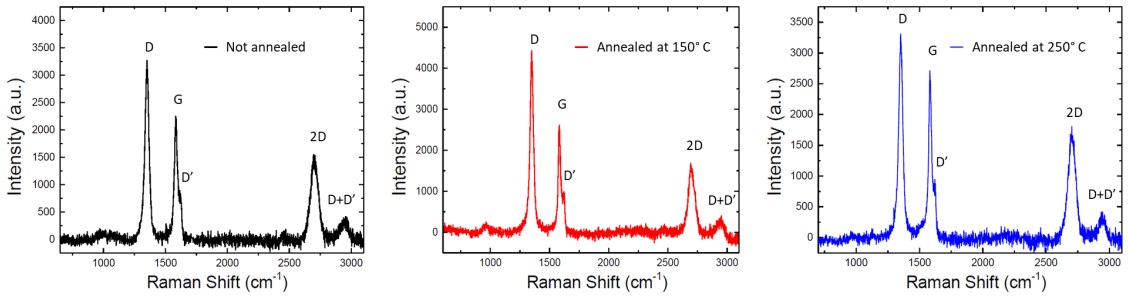

Figure 4.3: Raman spectroscopy analysis on three different graphene-ink samples: a not annealed sample (a), a 150° C-annealed sample (b), and a 250° C-annealed sample (c). Peaks location: D peak at $\sim$ 1350 cm^{-1}; G peak at $\sim$ 1580 cm^{-1}; 2D peak at $\sim$ 2695 cm^{-1}; D' peak at $\sim$ 1610 cm^{-1}; D+D' peak at $\sim$ 2955 cm^{-1}.

4.3 The graphene-ink annealing

Now, we need to do a digression because the as-printed graphene samples showed a very low conductivity.
In fact, by preliminary resistance measurements, we measured a sheet resistance of the order of $\sim$ 100 MΩ. Such high value of the resistance causes the presence of a great noise in the measurements; moreover, these resistance values, coupled with the parasitic capacitances of our setup wiring, give raise to not negligible parasitic currents with characteristic decay times of $\sim 1 \div 10$ sec for every tiniest change in the sourced current or the applied gate voltage.
To overcome this issue, we developed an annealing process that obtained a big enhancement of the conductivity up to $\sim$ 3 orders of magnitude.
Figure 4.4 a_1 shows a particular of a graphene inkjet-printed device and how it appears after the printing process with the characteristic Hall bar geometry.
We performed several different annealing processes on an equal number of samples in order to optimize the parameters and the conditions of the annealing process. We have investigated each sample by optical imaging, AFM characterization and resistivity measurements. Figure 4.4 shows, at a glance, the difference in the imaging and the AFM characterization for five different samples differently processed.
The first sample (figure 4.4 a_{1-3}) is not annealed: it shows a dominating brown colour at the optical microscope with a clear anisotropy in the direction of the printing process. The AFM characterization provides an average height $\bar{H} \simeq 460$ nm with a root mean squared roughness $R_Q \simeq 140$ nm. The phase contrast exhibits a very clear delineation of grains with average lateral size of $100 \div 200$ nm. The film appears to be continuous overall. However, as previously mentioned, the film resistance is extremely high ($\sim$ 100 MΩ).
The samples in figure 4.4 b_{1-3} and 4.4 c_{1-3} are annealed at $T = 150°$ C, the first

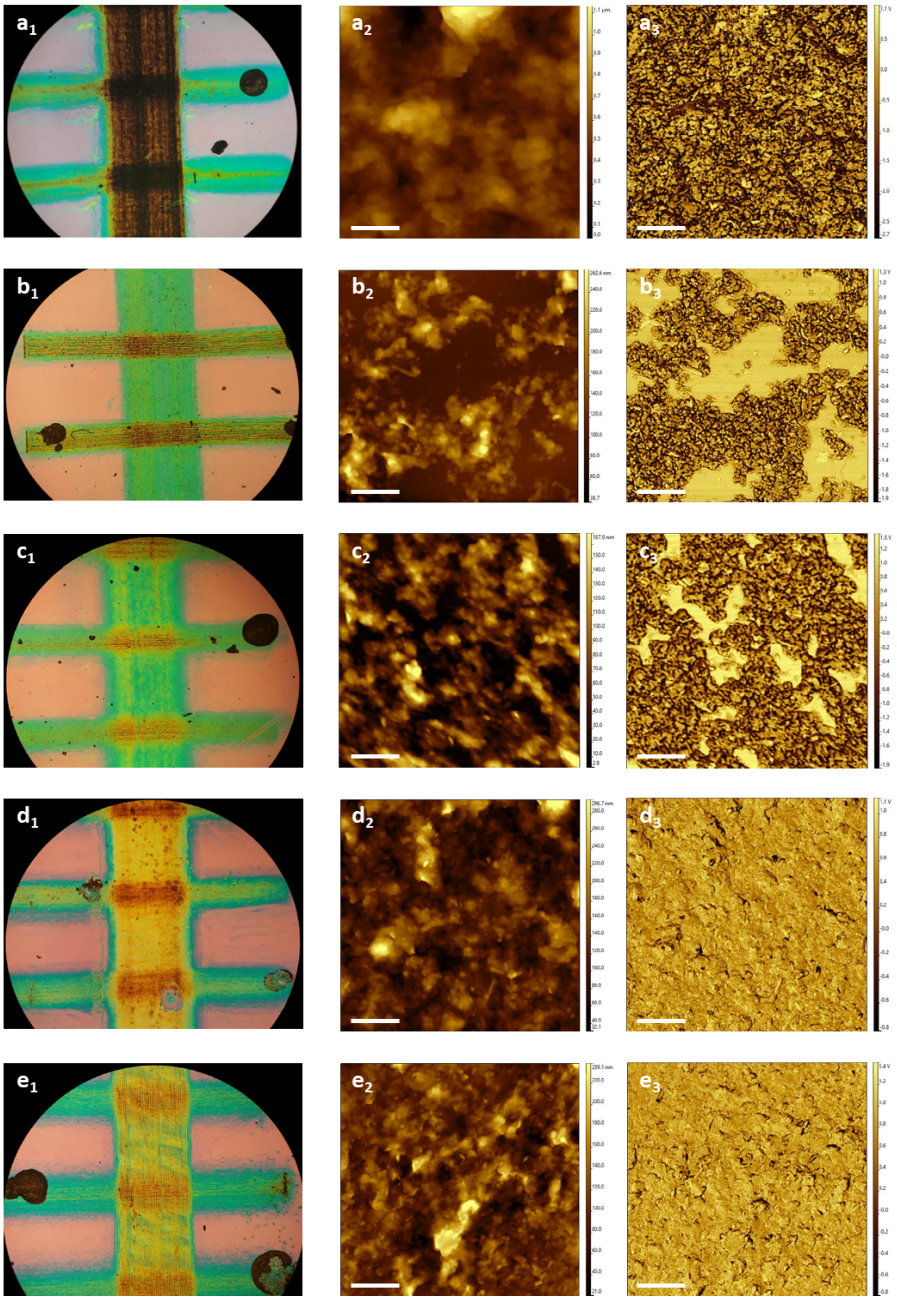

Figure 4.4: Analysis of different annealing parameters on five different samples: (a), (b), (c), (d), and (e). (a_1-e_1) is the optical image at 5× magnification; (a_2-e_2) is the topography, while (a_3-e_3) is the phase obtained by AFM measurements in tapping mode. Sample (a) is not annealed; sample (b) is annealed in air at $T = 150°$ C; sample (c) is annealed in argon at $T = 150°$ C; sample (d) is annealed in air at $T = 250°$ C; sample (e) is annealed in argon at $T = 250°$ C.

in air and the second in argon atmosphere, for 45 sec. A green-blue colour dominates the optical images, meaning that a deep change occurred to both the samples during the annealing process. The AFM analysis reveals that the samples are now extremely discontinuous with a clear separation between granular and flat regions; within the granular region, the average height $\bar{H}$ and root mean square roughness R_Q are both extremely reduced ($\bar{H} \simeq 140$ nm and $R_Q \simeq 36$ nm for the sample annealed in air; $\bar{H} \simeq 70$ nm and $R_Q \simeq 32$ nm for the sample annealed in argon) and the phase contrast is almost identical to the not-annealed sample; outside the granular regions, a flat, featureless region indicates that the surface is uniform and, thus, the substrate is exposed. Finally, both of the films are still extremely resistive, similarly to the not-annealed one.
The last two samples of figure 4.4 are annealed at $T = 250°$ C for 45 sec, the first in air (figure 4.4 d_{1-3}) and the second in argon (figure 4.4 e_{1-3}). The measured resistance in these samples is ~ 3 orders of magnitude lower than the others ($R_S \sim 10 \div 100$ kΩ). The optical images show that the dominating colour is now yellow. The AFM images now present a uniform surface with no exposed substrate areas, $\bar{H} \simeq 100$ nm and $R_Q \simeq 35 \pm 5$ nm for both the samples; moreover, the large phase contrast separating the grains is gone and the sample appears much more uniform.
The meanings of the observed changes are now briefly discussed.
The not-annealed sample shows larger roughness and average height with respect to the other samples: we suggest that the film still retains a significant amount of ethanol solvent trapped between the grains, which is released upon annealing. The evaporation of the ethanol may lead to the crumpling of the graphene sheets [187]. Indeed, the large phase contrast for the grains that is displayed in the first three samples can be addressed to the presence of crumpled graphene sheets that result to be badly connected one to the other. On the other side, thermal annealing in a temperature range between 200° C and 300° C can result in a stretching of the wrinkled sheets [188], thus leading to a better connection between the graphene flakes: this is most likely what happens in the two samples annealed at $T = 250°$ C, independently from the ambient or argon conditions. We attribute to these changes the extremely high change in the conductivity.
We are also confident to exclude a chemical change in the graphene inks because the annealing process in argon atmosphere obtains the same results as in air.
The reduction of possible graphene oxide deserves a particular mention. Indeed, the annealing of graphene at relatively high temperatures both under inert and ambient conditions enhances the C/O ratio and, thus, could lead to a relatively small increase in the conductivity [189]. However, such an eventuality is extremely unlikely here since (a) we used not-oxidised pristine graphite crystals and (b) no clear sign of graphene-oxide contribution is present at all in the Raman spectra [190] (and neither any significant change of the Raman spectrum in that direction after the annealing process; see figure 4.3).

The annealing process can also be repeated several times. However, an excessive number of annealing steps on the same sample, and/or the exposition for too long to high temperatures can result in the formation of conductive pin holes across the SiO_2 layer. This precludes the application of a gate voltage across the oxide and, thus, this leads to the failure of the device.

4.4 Transport characterization of graphene-ink films

The printed films on the SiO_2 substrate are then mounted on a copper holder and the contacts are realized via micrometric gold wires and silver paste. Temperature-dependent electric transport measurements were performed in the high-vacuum chamber of the Cryomech® pulse-tube cryocooler reaching a base temperature of 2.8 K.
The conductivity of the samples was measured in the four-probe configuration by supplying a small constant current $I_{DS} \sim 1\mu$A between the outer drain (D) and source (S) contacts with a two-channel Agilent B2912 source-measure unit (SMU), and measuring the longitudinal (V_{xx}) and transverse (V_{xy}) voltage drops between the inner voltage contacts with an Agilent 34420 nano-voltmeter. As in the previous chapters, common-mode offsets were removed by the current reversal method. The gate voltage V_G was applied between the S contact and the Si^{++} back-gate with the same two-channel SMU.

4.4.1 σ_{2D} in graphene-ink films

Figure 4.5 shows the sheet resistance (R_s) and the sheet conductivity (σ_{2D}) of the same graphene sample upon four different annealing steps: the conductivity slightly increases for each of the first three steps and then it saturates with no further changes. The resistance increases with decreasing T (figure 4.5a) suggesting, at a first glance, a semiconducting behaviour. By plotting $\log(\sigma_{2D})$ as function of $T^{-1/4}$ (see figure 4.5b) we notice a good linear dependence: it is the hallmark of a variable range hopping regime in a 3-dimensional network.
We performed AFM measurements on this sample to obtain its thickness: after the first annealing step the ink film is $t \simeq 100$ nm thick, without any significant change for further annealing steps.
Then we investigate the electric transport mechanism in this printed graphene-ink thin film by exploiting the solid-gate voltage configuration. We measured σ_{2D} as a function of the back-gate voltage (V_G) at several different temperatures T (see figure 4.6).
As expected, the curves are vertically shifted since σ_{2D} logarithmically increases

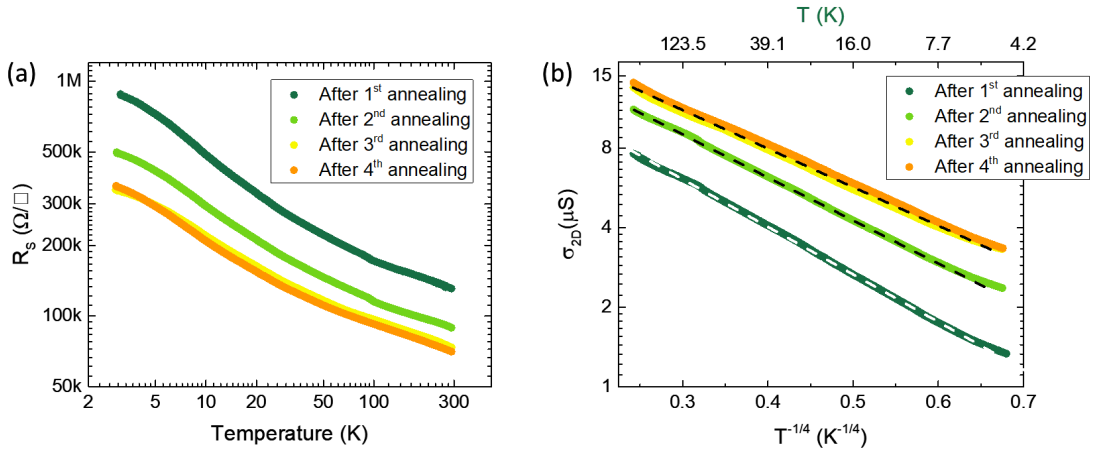

Figure 4.5: Sheet resistance (a) and sheet conductivity (b) of the same sample after four consecutive annealing steps. The annealing steps were performed at ambient conditions and at $T = 250°$ for an annealing time of $\sim$ 15 s (1^{st} step), 10 s (2^{nd} step), $\sim$ 15 s (3^{rd} step) and 30 s (4^{th} step).

with increasing T, while its behaviour in the electric field shows a monotonic decrease with increasing V_G, which is a signature of p-type conduction. This behaviour indicates that the graphene flakes are intrinsically hole doped, likely due to solvent residuals [191] and/or oxygen adsorption enhanced by the presence of moisture [192]. Due to the relatively large thickness of the films, the V_G-induced modulation of σ_{2D} is small and the channel can never be switched off. However, σ_{2D} shows a good linear scaling with V_G for $|V_G| \leq 40$ V at any T, allowing to determine the corresponding field-effect mobility μ_{FE}:

$$\mu_{\mathrm{FE}} = \frac{1}{C_{\mathrm{G}}} \left| \frac{\partial \sigma_{\mathrm{2D}}}{\partial V_{\mathrm{G}}} \right| \tag{4.1}$$

and the free carrier density of the graphene-ink film n_{3D}:

$$n_{\mathrm{3D}} = \frac{\sigma_{\mathrm{2D}}(V_{\mathrm{G}} = 0)}{e \cdot t \cdot \mu_{\mathrm{FE}}} \tag{4.2}$$

where $C_G = \epsilon_{ox}\epsilon_0/t_{ox} = 11.5$ nF/cm^2 is the gate capacitance per unit area, ϵ_0 is the vacuum permittivity, $\epsilon_{ox} = 3.9$ is the dielectric constant of SiO_2, $t_{ox} = 300$ nm is the thickness of the SiO_2 insulating layer, $t \simeq$100 nm is the film thickness and e is the elementary charge. Figure 4.7 shows the resulting T-dependences of μ_{FE} (black circles) and n_{3D} (blue diamonds). For $T \lesssim 200$ K, μ_{FE} increases with increasing T, which is typical of disordered systems where conduction occurs by carrier hopping between localized states. For $T \gtrsim 200$ K, on the other hand, μ_{FE} saturates and eventually starts to decrease, suggesting an incipient limitation by

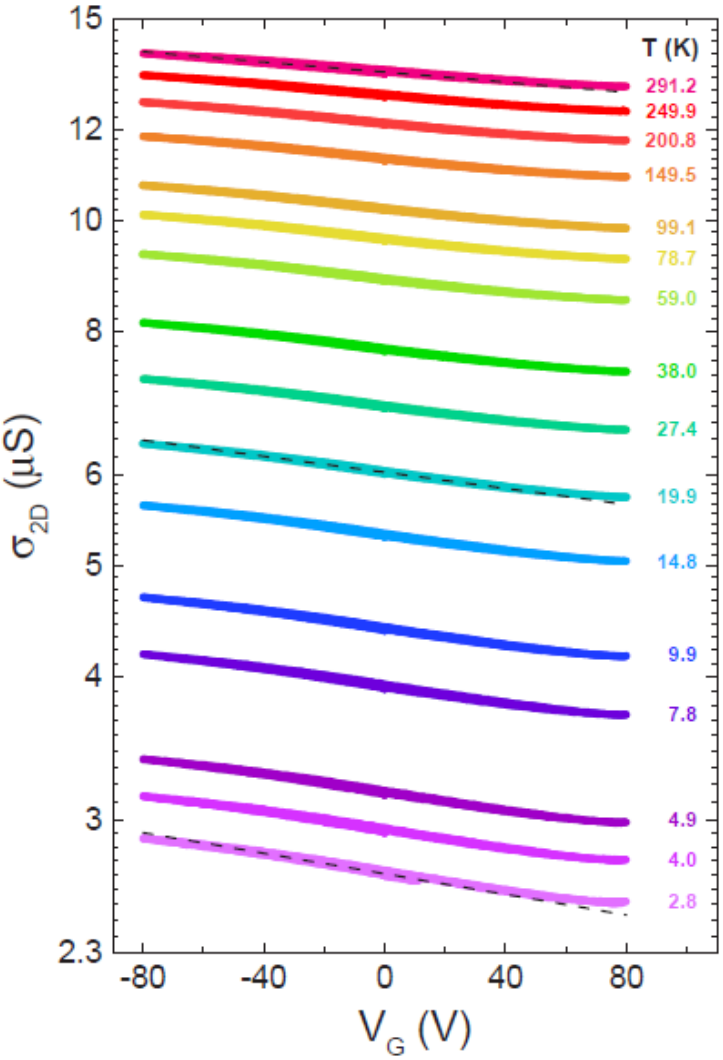

Figure 4.6: Sheet conductivity σ_{2D} vs. gate voltage V_G curves for a graphene-ink thin film on a Si/SiO_2 substrate for increasing temperature T. Dashed lines are linear fits to the data at $T = 2.8$ K, $T = 19.9$K and $T = 291$K in the linear region between $-40V \leq V_G \leq +40V$

phonon scattering close to room temperature [193]. The insulating behaviour of the graphene film is also reflected in the T-dependence of $n_{2D,0}$, which monotonically decreases with decreasing T.
Figure 4.8 shows a log plot of σ_{2D} as a function of $T^{-1/4}$, at $V_G = -80$ V (hollow red squares), $V_G = 0$ V (hollow green circles), and $V_G = +80$ V (hollow blue triangles). For all values of V_G, $\log(\sigma_{2D})$ exhibits an excellent linear scaling with $T^{-1/4}$, meaning that the application of high V_G, both positive and negative, does

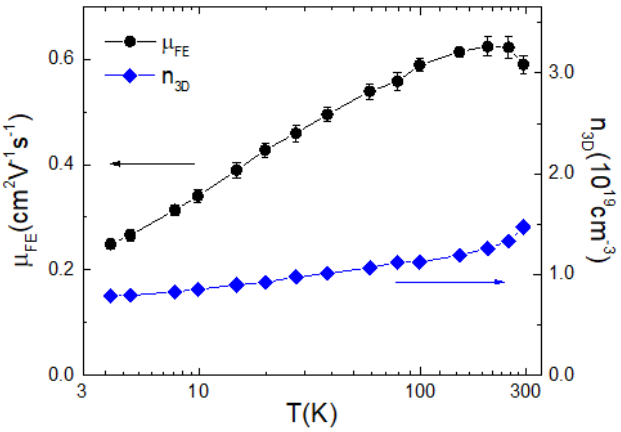

Figure 4.7: Field-effect mobility (left scale) and the free carrier density of the graphene-ink film (right scale) vs. T in semilogarithmic scale. Solid lines are guides to the eye.

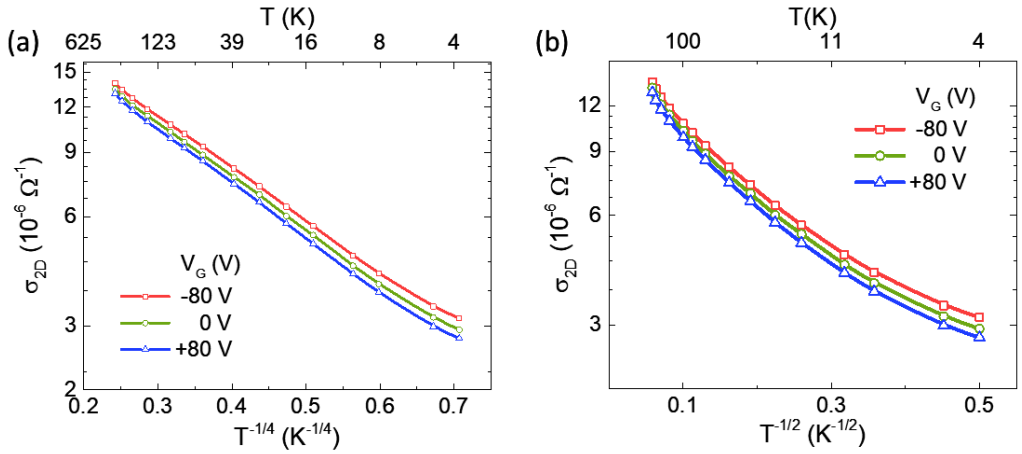

Figure 4.8: (a) σ_{2D} vs. $T^{-1/4}$ curves for V_G = -80 V, V_G = 0V and V_G = +80V. Solid lines are guides to the eye. Only a subset of the data at V_G = 0 V is shown for clarity. (b) The same data plotted vs. $T^{-1/2}$

not change the conductive bulk mechanism.
We double checked that any other scaling of σ_{2D} vs. T does not fit the data as good as the above mentioned. Generally speaking, the electrical conductivity in the VRH regime can show a T dependence of the form [169, 170, 193, 194]:

$$\sigma_{2D} = \sigma_0 exp\left(-\frac{T_p}{T}\right)^p \tag{4.3}$$

where T_p is a characteristic temperature, σ_0 is the conductivity at $T \to \infty$ and p is an exponent which depends on the specific VRH mechanism.
Non-interacting systems with a finite density of states (DOS) at the Fermi level can be described by the Mott-VRH mechanism with $p = 1/(d+1)$, where d is the dimensionality of the system [169, 170]. Conversely, interacting systems where the DOS at the Fermi level is suppressed by electron-electron interactions can be described by the Efros-Shklovskii mechanism (ES-VRH) with $p = 1/2$ regardless of the dimensionality [169, 170].
The good scaling of our data with $p = 1/4$ thus points to electric transport occurring via 3D Mott VRH in our graphene-ink films in the entire T range. We observe no evidence for the opening of a Coulomb gap, as demonstrated by the complete loss of linear scaling when the same $log(\sigma_{2D})$ data are plotted vs. $T^{-1/2}$ (see figure 4.8b). Moreover, also the linearity of the I-V curves at high and low temperatures discourages the interpretation of a Coulomb gap opening (see figure 4.9a).

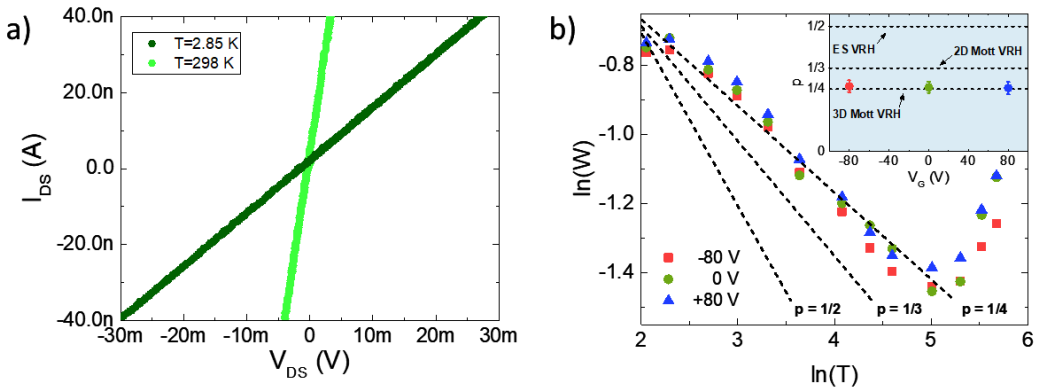

Figure 4.9: (a) Characteristic I-V measurements at room temperature and at base temperature. The linearity shown discourage the interpretation of the presence of a Coulomb gap opening. (b) $ln(W)$ as function of $ln(T)$ extracted by applying eq. 4.4 to the data in figure 4.8. Dashed lines are linear fits to the data in the region between $2 \leq ln(T) \leq 5$.

We further confirm that charge transport occurs through 3D Mott-VRH by introducing the reduced activation energy W, defined as [194, 195]:

$$W(T) = \frac{\partial(\ln(\sigma_{2D}))}{\partial(\ln(T))} \tag{4.4}$$

which allows to more accurately determine the scaling factor p as the slope of the linear fit to $ln(W)$ vs. $ln(T)$ [195]. As we show in figure 4.9b, at all values of V_G we find that the experimental data match well the expected scaling for $p = 1/4$

(3D Mott-VRH), while they deviate substantially from both $p = 1/3$ (2D Mott-VRH) and $p = 1/2$ (ES-VRH). Furthermore, linearly fitting $ln(W)$ vs. $ln(T)$ in the range $2 \leq ln(T) \leq 5$ (which corresponds to $7K \lesssim T \lesssim 150K$) gives a quantitative estimation of $p = 0.26 \pm 0.01$ (see inset to figure 4.9b), in excellent agreement with the 3D Mott-VRH value $p = 1/4$, thus ruling out both ES-VRH and a possible 2D Mott-VRH. The analysis of the reduced activation energy highlights another feature of the conduction mechanism in the graphene-ink films, which is not apparent from the simple T-dependence of σ_{2D}: for $ln(T) \geq 5$ ($T \gtrsim 150$ K) W increases with increasing T. This indicates that charge transport ceases to follow the expected scaling for pure VRH. As shown in figure 4.7a, this is the same T range where μ_{FE} starts to decrease with increasing T: as such, we identify this as the range of T where the conductivity is no longer limited purely by the carrier hopping probability and a non-negligible contribution from electron-phonon scattering emerges in the system. Finally, the good scaling of our data with $p = 1/4$ allows us to determine the characteristic temperature T_p that appears in eq. 4.3 that results $T_{1/4} = 138 \pm 11$ K.

4.4.2 Magnetotransport in graphene-ink films

A deeper insight on the microscopic conduction mechanism can be gained with exploring the resistance response upon the application of an external magnetic field. Magnetotransport measurements were performed in He atmosphere in the variable-temperature insert of a Oxford Instruments ^{4}He cryostat equipped with a 9 T superconducting magnet.

In figure 4.10 we plot as filled dots the magnetoresistance ratio MR $= [R(B) - R(0)]/R(0)$ vs. the intensity of the magnetic field B, for different values of T between 4.2 K and 40.1 K.

The magnetic field is applied in the out-of-plane direction. The MR is always negative, quasi-linear at low B, and shows incipient saturation at high B for $T \lesssim 20$ K. Such a behaviour is typical of the magnetotransport in the VRH regime, which is usually determined by the sum of two contributions [196–198]. The first contribution arises from the quantum interference of different hopping paths, which results in a linear, negative magnetoresistance and is described by the forward-interference model [199]. The second contribution is due to the magnetic-field-induced contraction of the charge-carrier wavefunction at defect sites, which results in a quadratic, positive magnetoresistance and is described by the wavefunction-shrinkage model [200]. In the case of 3D Mott-VRH and in the low-field limit ($B \ll B_{sat}, B_c$), these two contributions are [196–198]:

$$\mathrm{MR} = -C_{sat}\frac{B}{B_{sat}} + t^2\frac{B^2}{B_c^2}\left(\frac{T_{1/4}}{T}\right)^{\frac{1}{4}} \tag{4.5}$$

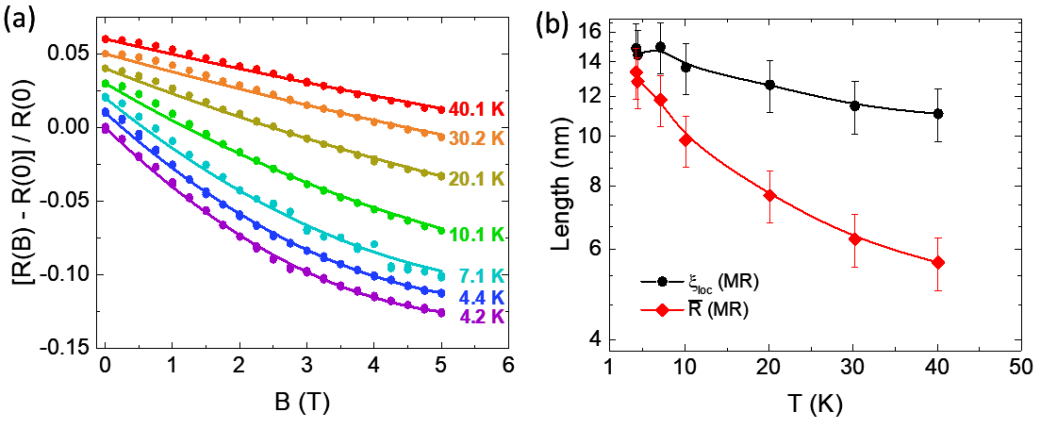

Figure 4.10: (a) Magnetoresistance ratio $[R(B) - R(0)]/R(0)$ vs. magnetic field B for increasing temperature T. Filled circles are the experimental data, solid lines are the fits according to Eq.4.5. Curves at different T are shifted by 0.01 for clarity. (b) Localization length ξ_{loc} (circles) and average hopping distance $\bar{R}$ (diamonds) as a function of T. The lengths are obtained combining the T-dependence of σ_{2D} with the MR fits.

with

$$B_{sat} = 0.7 \left(\frac{8}{3}\right)^{\frac{3}{2}} \left(\frac{2\pi\hbar}{e\xi_{loc}^2}\right) \left(\frac{T}{T_{1/4}}\right)^{\frac{3}{8}} \tag{4.6}$$

and

$$B_c = \frac{6\hbar}{e\xi_{loc}^2} \left(\frac{T}{T_{1/4}}\right)^{\frac{1}{4}} \tag{4.7}$$

where C_{sat} is a positive constant of order unity, $t^2 = 0.0893$ is a numerical constant, and $\hbar$ is the reduced Planck constant. We fit our experimental MR data to eq. 4.5 and plot the resulting best fits as the solid lines in figure 4.10. The fits show an excellent agreement with the experimental data, and the corresponding values of B_{sat} and B_c are always larger than 17 T and 8 T respectively, and the choice of the low-field limit is still valid, even though they are not much bigger than the applied magnetic field. Overall, we conclude that the electric transport in our graphene-ink films as a function of both T and B can be fully described in terms of 3D Mott-VRH conduction.

Having firmly established the conduction mechanism in our graphene-ink films, we can extract the associated hopping parameters, namely the localization length ξ_{loc} and the average hopping distance $\bar{R}$. The former can be extracted directly from

the best fits to the magnetoresistance data, and the latter is simply [169, 198]:

$$\bar{R} = \frac{3}{8}\left(\frac{T_{1/4}}{T}\right)^{\frac{1}{4}} \xi_{loc} \tag{4.8}$$

We plot the values of ξ_{loc} and $\bar{R}$ obtained from the MR fits in figure 4.10 as filled circles and diamonds respectively. Both quantities are of the order of $\sim$ 15 nm at 4.2 K and are suppressed upon increasing T. With increasing T, $\bar{R}$ decreases much more strongly than ξ_{loc}, and, at $T \simeq 40$ K, $\bar{R}$ is comparable to the average flake thickness; however, the transport properties continue to scale well with the 3D model, still supporting a picture where charge carriers hop between different flakes in the 3D network.

4.5 Transport characterization of MXene-ink films

4.5.1 σ_{2D} in MXene-ink films

We then performed similar measurements on the MXene-ink films.
As presented in figure 4.11, the MXene-ink-films $\sigma_{2\mathrm{D}}$ first increases and then decreases upon increasing T, suggesting a crossover from metallic-like transport at high T to some kind of localized behaviour at low T. Notably, the $\sigma_{2\mathrm{D}}$ of the MXene-ink films is about two orders of magnitude larger than that of the graphene-ink films in the entire T range, making the electric field effect significantly harder to detect. Nevertheless, we were able to observe a small modulation of $\sigma_{2\mathrm{D}}$ with V_G also in the MXene-ink films (see figure 4.11). Here, $\sigma_{2\mathrm{D}}$ slightly increases upon increasing V_G, indicating n-type behaviour. We note that the V_G-modulation of $\sigma_{2\mathrm{D}}$ in MXene-ink films could be observed only at small channel thickness and became immeasurably small in thicker devices.
Also in this case, σ_{2d} shows a good linear scaling with V_G for $|V_G| \leq 40$ V at any T; thus, we can determine the corresponding μ_{FE}.
A complete characterization of the film thickness, as well as the average flake thickness is ongoing. As far as the flakes lengths are concerned, referring to Ref. [180], we expect an average flake thickness of $t_f \sim$1.8 nm and a lateral size of $S \approx 2.1\mu$m. Furthermore, since the modulation of the conductivity requires the film to be extremely thin, we do the hypothesis that the total film thickness is made of a stacking of at most 50 flakes ($t \approx 90$ nm).
Under these hypothesis, we can define the average density of free carriers per graphene flake at $V_G = 0$, $n_{2D,0}$:

$$n_{2\mathrm{D},0} = \frac{t_f}{t}\frac{\sigma_{2\mathrm{D}}(V_\mathrm{G}=0)}{e\mu_{\mathrm{FE}}} \tag{4.9}$$

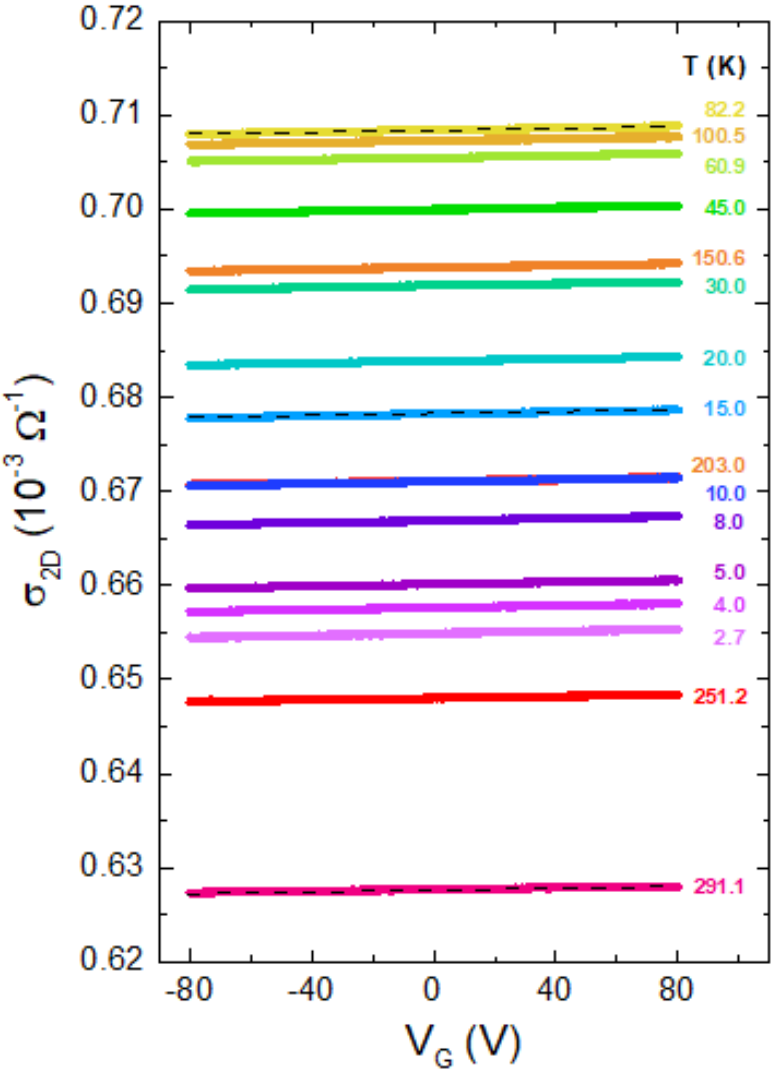

Figure 4.11: Transfer curves for a MXene-ink TFT for increasing temperature T. Dashed lines are linear fits to the data at $T = 15.0\,\mathrm{K}$, $T = 82.2\,\mathrm{K}$ and $T = 291\,\mathrm{K}$ in the full V_G range.

Figure 4.12 shows the resulting T-dependences of μ_{FE}, and of $n_{\mathrm{2D},0}$ in the case of the MXene-ink films. μ_{FE} slightly increases upon decreasing T and saturates for

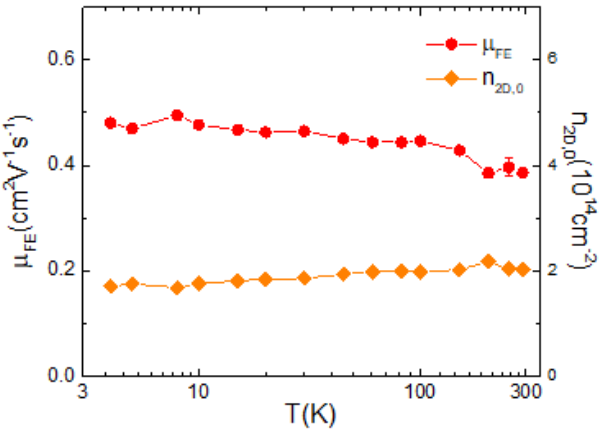

Figure 4.12: MXene-ink film field effect mobility μ_{FE} and average density of free carriers per graphene flake at $V_G = 0$, $n_{2D,0}$.

$T \to 0$. This very weak sensitivity of the mobility to the increase of T is typical of disordered metallic systems where the main source of charge-carrier scattering is that coming from defects. The free carrier density in the system is even less sensitive to changes in T, and remains almost constant all the way from $T = 2.7\,\mathrm{K}$ to $T \simeq 290\,\mathrm{K}$. Note that both behaviours are observed also at $T \lesssim 80\,\mathrm{K}$, where σ_{2D} increases upon increasing T: this indicates that, even if some degree of carrier localization is taking place at low T, it does not disrupt the metallic character of the electric transport. Thus, MXene-ink films retain metallic conductivity in the entire T range.
We can also compare the values obtained for MXenes-inks with those obtained for graphene-inks. To do so, we calculate $n_{2D,0}$ also for graphene, by considering that the average flake thickness t_f in graphene-ink films is more than 3 times higher with respect to t_f in MXene-ink films, and that graphene flakes are almost 15 layers thick.
The magnitude of the mobility is comparable in the two materials (see figure 4.13a): μ_{FE} in the MXene-ink is about $\sim 50\%$ lower than μ_{FE} in the G-ink at $T \simeq 290$ K, but nearly $\sim 150\%$ larger at $T = 2.7$ K. Conversely, $n_{2D,0}$ in the MXene-ink is nearly two orders of magnitude larger than $n_{2D,0}$ in the G-ink in the entire T range. This large difference in free carrier density has a profound impact on the relative gate-tunability of σ_{2D} in the two inks: If we consider $T \simeq 30\,\mathrm{K}$, where the mobilities of the two materials are nearly equal ($\mu_{FE} \simeq 0.48\,\mathrm{cm^2V^{-1}s^{-1}}$), σ_{2D} in the G-ink can be tuned by nearly $\sim 10\%$ of its value, while in the same scale σ_{2D} in the MXene-ink is basically V_G-independent.

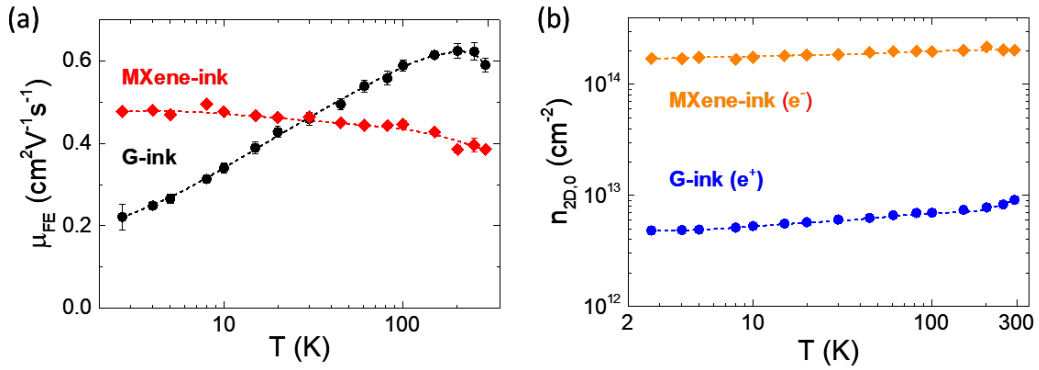

Figure 4.13: (a) Field-effect mobility μ_{FE} vs. T in semilogarithmic scale for a G-ink films (black dots) and MXene-ink films (red diamonds). Dashed lines are guides to the eye. (b) Intrinsic carrier density per flake $n_{2D,0}$ vs. T in semilogarithmic scale for a G-ink film (blue dots) and a MXene-ink film (orange diamonds). Dashed lines are guides to the eye.

We can further investigate the electric transport mechanism in the printed MXene-ink films by coming back to the T-dependence of the sheet resistance R_s shown in figure 4.14a (solid green line). The R_s of a 28nm-thick MXene film epitaxially grown on sapphire, as reported in Ref.[201], is also shown for comparison (filled black diamonds).
We have already seen that the MXene-ink films conduction mechanism strongly points to a metallic-like transport with some degree of carrier localization at low T. More in detail, for $T \gtrsim 100\,\mathrm{K}$, R_s increases with increasing T, which is the hallmark of conduction occurring over extended states with electron-phonon (e-ph) scattering as the main source of inelastic scattering. For $T \lesssim 100\,\mathrm{K}$, on the other hand, R_s weakly increases with decreasing T, a typical feature of disordered metallic systems with 2D character [202].
Interestingly, the same qualitative behaviour is observed in both epitaxial films and the printed films, with three notable differences. The first difference is the much smaller resistivity of the epitaxial film ($\rho \simeq 5.2\,\mu\Omega\,\mathrm{m}$ at $T = 100\,\mathrm{K}$; Ref. [201]) with respect to the printed TFT ($\rho \simeq 126\,\mu\Omega\,\mathrm{m}$ at $T = 100$ K, with the hypothetical film thickness $t \approx 90$ nm, as mentioned before), which is obviously due to the granular nature of the latter. The second difference is the larger magnitude of the low-T upturn relative to the room-T value of R_s in the epitaxial film, and the different T where the R_s minimum is observed ($T \simeq 80$ K in the printed TFT, vs. $T \simeq 90$ K in the epitaxial film). The third difference is the slight superlinear scaling of R_s vs. T at high T in the printed TFT, which is not observed in the epitaxial film and may be due to increased inhomogeneity or a stronger coupling to carrier scattering

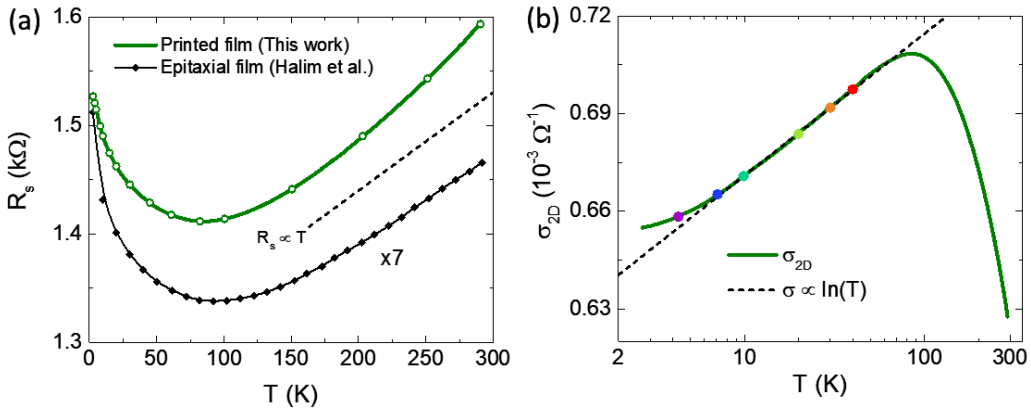

Figure 4.14: (a) Sheet resistance R_s vs. temperature T for a MXene-ink TFT (solid green line), with hollow circles marking the values of T where the V_G sweeps shown in figure 4.11 were acquired). The R_s of a MXene epitaxial film from Ref. [201] is shown for comparison (filled black diamonds and solid black line, data are multiplied by 7 for clarity). Dashed line is the linear scaling expected at high T for carrier scattering with acoustic phonons only. (b) Same data of panel (a) for the MXene-ink TFT, plotted as σ_{2D} vs. T in semilogarithmic scale (solid green line). Dashed black line is a linear fit to the data. Filled circles mark the values of T where the B sweeps shown in figure 4.15 were acquired.

channels other than with simple acoustic phonons [97, 203, 204].
We now focus on the low-T upturn. As we show in figure 4.14b, for $T \lesssim 70\,\mathrm{K}$ the sheet conductivity scales well as $\sigma_{2D} \propto \log(T)$. Such a logarithmic dependence is typically exhibited by 2D metallic systems in the presence of weak localization (WL), which is a phenomenon that occurs at low T due to suppressed inelastic scattering. In these conditions, charge carriers become able to retain their phase coherence over a length L_ϕ which is larger than the elastic scattering length L_e, leading to coherent backscattering with a probability that increases logarithmically with decreasing T [202]. Indeed, WL has been shown to be responsible for the upturn occurring in the epitaxial MXene thin films and shown in figure 4.14a [201]. However, note that the logarithmic scaling (black dashed line in figure 4.14b) describes well the experimental T-dependence of σ_{2D} in our printed MXene-ink TFTs only in the range $7\,\mathrm{K} \lesssim T \lesssim 70\,\mathrm{K}$. For $T \lesssim 7\,\mathrm{K}$, σ_{2D} starts to deviate from the expected scaling law and shows an incipient saturation below $\simeq 4\,\mathrm{K}$. This latter feature can occur in granular media when L_ϕ approaches the lateral size d_f of the metallic grains in the network [205, 206]. Above this crossover T only intragrain coherent backscattering is possible, and if intragrain carrier transport is diffusive ($L_e \ll d_f$) the WL correction has the same form as that of a homogeneous medium.

On top of the logarithmic correction to the T-dependence of R_s and σ_{2D}, the signature of WL in the low-T transport properties of a 2D system is a positive magnetoconductance.

4.5.2 Magnetotransport in MXene-ink films

Therefore, we now consider the low-T magnetotransport properties of our MXene-ink TFTs, and show that they can be well described in terms of WL in presence of a finite spin-orbit interaction (SOI). We will thus focus on $T \gtrsim 4\,\mathrm{K}$ where the coherent transport occurs within each single grain and the standard models for WL are applicable to our system.
In figure 4.15 we plot the magnetoconductance $\Delta\sigma(B,T) = \sigma_{2D}(B,T) - \sigma_{2D}(0,T)$ as a function of the out-of-plane magnetic field B for different values of T between 4.3 K and 40 K. At any T, $\Delta\sigma$ is positive and its magnitude at a given B decreases

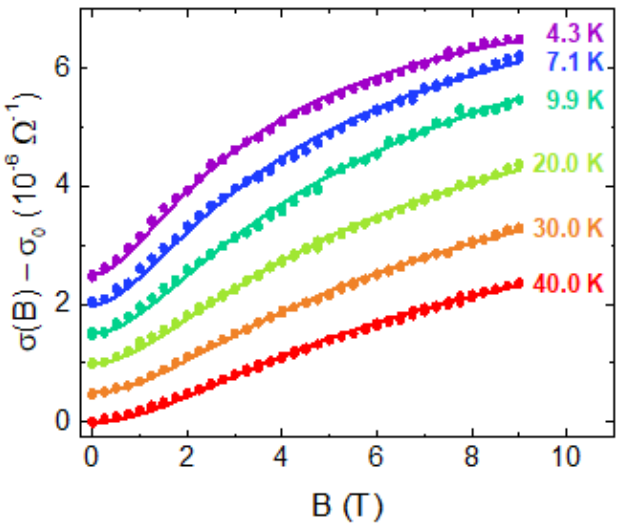

Figure 4.15: Magnetoconductance $\sigma_{2D}(B)$ - $\sigma_{2D}(0)$ vs. out-of-plane magnetic field B for increasing temperature T. Filled circles are the experimental data. Solid lines are the fits according to Eq.4.10. Curves at different T are shifted by $5 \cdot 10^{-7}\,\Omega^{-1}$ for clarity.

upon increasing T, as expected for WL behavior. Since MXenes can feature an intrinsic SOI arising from the transition-metal atoms [207], we analyze quantitatively our data employing the Hikami-Larkin-Nagaoka (HLN) model [208, 209], which describes the magnetoconductance of 2D metallic systems in presence of finite intrinsic SOI (Dresselhaus mechanism) [141]. According to this model $\Delta\sigma(B)$ is given

by:

$$\Delta\sigma(B) = \frac{e^2}{2\pi^2\hbar}\left[F\left(\frac{B_\phi}{B}\right)\right] + \frac{e^2}{2\pi^2\hbar}\left[F\left(\frac{B_{so}+B_e}{B}\right)\right] - \frac{3e^2}{2\pi^2\hbar}\left[F\left(\frac{(4/3)B_{so}+B_\phi}{B}\right)\right] \tag{4.10}$$

with

$$F(z) = \ln(z) - \psi(1/2+z) \tag{4.11}$$

and

$$B_{\phi,so,e} = \hbar/4eL^2_{\phi,so,e} \tag{4.12}$$

where ψ is the digamma function and L_{so} is the spin-coherence length that represents the minimum distance travelled by a charge carrier before its phase is significantly affected by SOI.
As shown in figure 4.15, the fits according to eq. 4.10 (solid lines) show excellent agreement with the experimental values of $\Delta\sigma(B)$ at all values of T, including at 4.3 K where $\sigma_{2D}(T)$ starts to deviate from the logarithmic scaling and the validity of the HLN model is only marginal.
We plot the characteristic lengths extracted from the fits in figure 4.16. The spin-coherence length L_{so} (red diamonds) is found to be constant with T, as is to be expected [141], and larger than both L_ϕ and L_e in the entire T range. This indicates that the SOI in the system is too weak to force the spin of the charge carriers to complete a full precession as they undergo coherent backscattering, which would destroy the constructive interference responsible for WL and lead to the emergence of weak anti-localization (WAL) instead: No WAL-induced "cusp" close to $B = 0$ is observed in the experimental data. On the other hand, L_ϕ is significantly suppressed upon increasing T, consistently with the fact that inelastic scattering processes, which are responsible for the loss of phase coherence, become more effective upon increasing T. Specifically, we find that L_ϕ scales well as $T^{-1/2}$ (see the inset to figure 4.16), which identifies electron-electron collisions with small energy transfer (Nyquist scattering) as the main source of dephasing in the system [95, 210]. L_e is found to be nearly T-independent for $T \lesssim 10$ K, as expected for elastic scattering with defects at low T, and weakly decreasing at larger T. Even at $T = 40$ K, L_e remains smaller than L_ϕ, consistently with the observation of a clear WL downturn in $\sigma_{2D}(T)$ all the way up to $T \sim 80$ K. Finally, note that all three characteristic lengths remain much smaller than $S \simeq 2.1\mu$m down to 4.3 K, confirming that, in the considered T range, the WL behavior is fully determined by phase-coherent diffusive transport within each MXene flake.

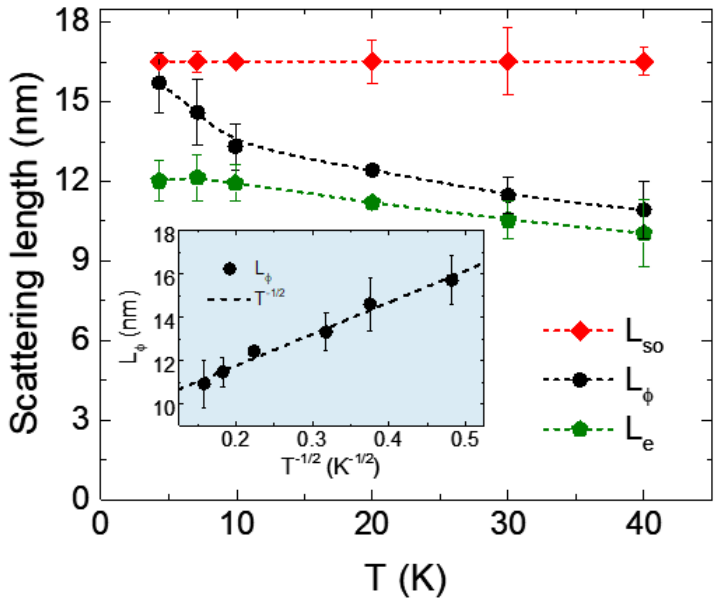

Figure 4.16: Spin-coherence length L_{so} (red diamonds), phase-coherence length L_ϕ (black circles) and elastic scattering length L_e (green pentagons) vs. T, as determined from the fits shown in figure 4.15. Dashed lines are guides to the eye. Inset shows L_ϕ as a function of $T^{-1/2}$ and a linear fit to the data.

4.6 Conclusions

Concluding, the electrical characterization of graphene-ink and MXene-ink thin films unveiled very interesting aspects of the macroscopic and mesoscopic transport mechanism in these systems.
Graphene and MXene are both 2D materials; thus, we prepared the inks via liquid phase exfoliation (LPE) of their precursors (graphite for graphene and MAX phase for MXene), following two different processes already present in the literature [180, 181]. The graphene grains are quite thick ($\sim$ 15 layers on average). The MXene grains are mostly single- or few layers thick.
Graphene-ink devices were annealed to improve their transport properties. Indeed, the as-printed devices before the annealing showed a huge resistance ($\sim$ 100 MΩ) which precluded the field-effect characterisation. An annealing process at controlled conditions allowed us to increase the conductivity of more than 3 orders of magnitude. The annealing step is found to operate in two ways: first, the heating of the sample helps evaporating the solvent trapped between the grains; second, the annealing at 250°C flattens the crumpled flakes that experiments a better intergrain connection.

We then measured the temperature dependence of the sheet conductivity σ_{2D}, the field-effect mobility μ_{FE} and the carrier density n_{3D}, and, finally, we characterized the films as far as the magnetotransport properties are concerned.
The temperature dependence of the conductivity demonstrates that graphene-ink films are dominated by a 3D variable range hopping (VRH) transport mechanism. The study of the field effect mobility (μ_{FE}) and of the carrier density (n_{3D}) confirm the disordered and insulating nature of the system. The magnetoresistance ratio (MR) is thus studied under the VRH regime hypothesis, and the fitting curves are in excellent agreement with the experimental data. Moreover, the hopping parameters (the localization length ξ_{loc} and the hopping length $\bar{R}$) are obtained from the magnetoresistance measurements. In particular, $\bar{R}$ is always higher than the average flake thickness, confirming that the carrier hopping primarily occurs between different grains.
Concluding, as far as the graphene-based ink is concerned, we notice that the disordered cluster of graphene flakes behaves extremely differently from what expected from each single flake. Indeed, the overall conduction mechanism of the ink is 3D-like, despite the 2D nature of its components. Moreover, the ink loses the extremely high carrier mobility that is a distinguishing feature of graphene. It is now limited to be always $\lesssim 0.6$ cm^{2}V^{-1}s^{-1}.
Conversely, MXene-ink thin films do maintain the qualitative behaviour of epitaxially-grown MXene thin films. They both show a metallic-like T-dependence of the conductivity for high temperatures and an upturn at low temperatures that is the sign of 2D weak localization (WL). Field-effect characterization of the MXene-ink films shows that the conduction mechanism is in agreement with what expected in a disordered metallic system. In particular, as expected in metals, the system shows a high negative carrier density ($\sim 2{\cdot}10^{14}$ e$^-$/cm^{-2}) that is invariant with temperature, while, as expected in disordered systems, the carrier mobility is limited by defects at low temperatures.
We finally studied the magnetoresistance of MXene-ink films within the Hikami-Larkin-Nagaoka model which takes into account the spin-orbit interaction (SOI) of 2D metallic materials. We show that the WL behaviour is not affected by the SOI, and the temperature dependence of the resistance upturn is exclusively related to the phase coherence length.

Chapter 5

Ferroelectric gating in gold and preliminary ionic gating in ultra-thin NbN films

As we have seen in Chapter 1, another way to perform field effect experiments is to use the ferroelectric gating technique. This technique is basically a solid gating technique, where a ferroelectric material is sandwiched between a metallic electrode and the material under study, being the ferroelectric itself an insulator. This technique has the advantage of reaching higher surface induced charge densities with respect to standard MOSFET structures. Moreover, it allows to switch the polarization of the ferroelectric material generating, de facto, a device that is able to remain in two different states even at low temperatures.
In this chapter we aim at exploiting the ferroelectric properties of PZT (lead zirconate titanate) to modulate the properties of a gold thin film evaporated on top of the PZT layer. This experiment is preliminary and it is aimed at the characterization of the PZT layer itself.
In the second part of this chapter we perform ionic gating experiments on ultra-thin NbN films: we show that the maximum induced charge density is comparable to the values that can be reached by ferroelectric gating, leaving to the future the possibility to apply ferroelectric gating on this system.
Our aim is thus to apply the ferroelectric gating to superconducting materials (like NbN), in order to switch the superconductivity at low temperatures by modulating the gate voltage and hence creating very fast superconducting switches that could have important technological applications.

5.1 Ferroelectric gating in gold thin films

5.1.1 Preparation of the device

In order to perform ferroelectric gating experiments in gold, we evaporated a thin layer of gold on top of PZT/Pt/SiO_2 commercial substrates.
The substrates for the devices we used were purchased from Silicon Sensing®. They are made of a layered structure: the background is made of a Si/SiO_2 substrate; on top of it, there is a 100 nm Platinum layer which serves as counter electrode in the polarization of the piezoelectric; finally, a ~ 1 μm thick PZT layer obtained by sputtering is present on the top (see figure 5.1).

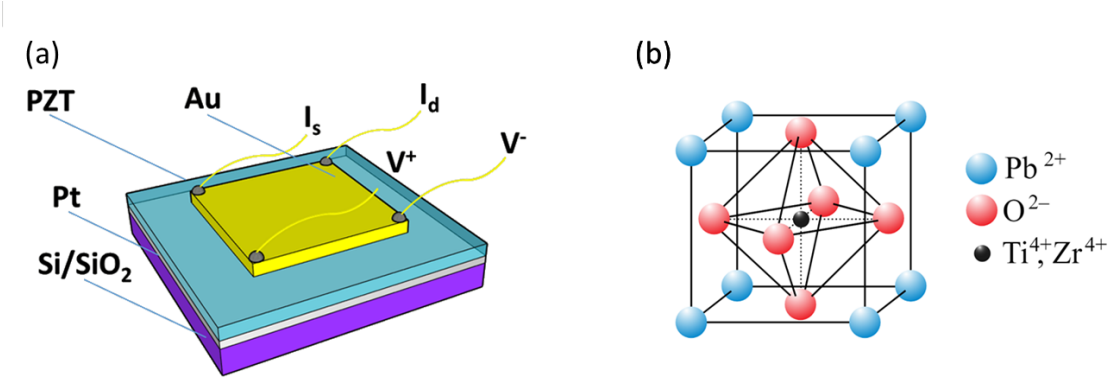

Figure 5.1: (a) Sketch of the device used for preliminary ferroelectric gating experiments: the electrical contacts are disposed following the configuration for the resistivity measurements with the Van der Pauw technique. The Au ($\sim$ 38 nm measured by AFM) film is evaporated on top of the PZT ($\sim 1\mu$m) layer. The Platimun (Pt) layer is $\sim$ 100 nm thick. (b) PZT crystallographic structure. It shows the characteristic perovskite structure.

Lead zirconate titanate (PZT; $Pb(Zn_xTi_{1-x})O_3$) is a polycrystalline ceramic material that shows a perovskite-like crystallographic structure (see figure 5.1b). Thanks to its physical and chemical robustness and its tailorability, as well as the higher working temperatures with respect to other piezoelectric materials, it is widely used for several applications like: accelerometers, inkjet heads, MEMS microphones, micropumps, gyros, ultrasonic sensors and energy harvester, mostly exploiting its piezoelectricity.
Our aim, in the first part of this study, is to characterize the material at our disposal as far as the piezoelectric and ferroelectric effects are concerned. Then, we will be able to exploit the ferroelectric and piezoelectric effects to tune the superconducting properties of NbN ultrathin films.

We realized a metal-ferroelectric-metal structure to characterize the PZT properties. As already said, we deposited via physical vapour deposition a $\sim$ 38 nm thick Au layer as top electrode; we realized a simple square geometry with 1.3 mm side length by means of a square shadow mask. The evaporation process was held in a high-vacuum chamber at $4 \cdot 10^{-6}$ mBar for 100 s. We used the intrinsic Pt layer as the bottom electrode.
Some devices showed randomly distributed pinholes in the PZT layer, shortcutting the two plates of the capacitors. To reduce this occurrence, we limited the dimensions of the Au square to the aforementioned ones. We observed that treatments in acetone and ethanol, like sonication, strongly increases the possibility of finding pinholes and, as a consequence, we limited as much as possible these standard cleaning procedures.
The as-prepared devices are stable in air.

5.1.2 Polarization of the PZT

We are interested in the characterization of the devices in the temperature range between room temperature and $\sim$ 2.8 K. We, thus, placed the samples in the vacuum chamber of a Cryomech® cryocooler. Four-wire resistivity measurements were performed by supplying a current of $\sim$ 10 mA with an Agilent B2912 source measure unit (SMU) and measuring the voltage drop with an Agilent 34420A. The gate voltage across the PZT was supplied by the second channel of the Agilent B2912.
As already said and referring to figure 5.1a, we exploited a Van der Pauw configuration to measure the resistivity of the sample under gating. This technique is a very useful method to determine the resistivity in a sample with a planar configuration and a regular geometry [211]. In the simplest geometry, the square, two consecutive contacts are used to supply the current while the other two are used to measure the voltage drop. If the material is perfectly uniform and with a perfectly squared geometry, it is possible to obtain the sheet resistance (R_S) with the following equation:

$$R_S = \frac{-\pi R}{\ln \frac{1}{2}} \tag{5.1}$$

being $R = \Delta V / I$. However, the same technique allows to obtain the resistivity also in samples which geometry is not perfectly regular. In these cases, it is necessary to measure R for each possible configuration made by the four contacts: i.e. we rotate the current and voltage contacts and we measure every time R and invert the current. Finally, we average the R values obtained in the longitudinal (R_L) and transverse (R_T) direction and R_S can be obtained by solving numerically the following equation:

$$e^{-\frac{\pi R_L}{R_S}} + e^{-\frac{\pi R_T}{R_S}} = 1 \tag{5.2}$$

(that reduces to eq. 5.1 if $R_L = R_T$).
With this setup we could measure the resistance while polarizing the PZT.
We measured the gate current I_G upon the application of V_G across the parallel plate capacitor. The I_G vs. V_G curves are shown in figure 5.2.
To polarize the ferroelectric, it should be convenient to use a triangular waveform as input gate voltage. However, the wiring system of the cryocooler is not designed to supply alternating voltages for studying the response in frequency of the experiments; i.e. the wires are not fully screened and they give raise to parasitic capacitances. Thus, we opted to apply the electric field by linearly increasing (and then decreasing) V_G with very small discrete steps of 0.1 V per second. Considering that V_G spans in a maximum range between - 28 V and + 38 V (at least $-7V \leq V_G \leq 7V$), a constant rate of 0.1 V/s corresponds to very low frequencies (always $\lesssim 0.07$ Hz); with this expedient, we could dramatically reduce the parasitic capacitances contribution.
The maximum V_G application is limited by the formation of percolative paths through the PZT that are evidenced by an abrupt increase in I_G; once the percolative path is formed, I_G remains at the compliance value even reducing V_G; however, it is often possible to restore the insulating behaviour of the PZT layer by operating an inverse polarization. After that, the device returns to its regular behaviour. Incidentally, the V_G limit that induces the formation of these percolative paths is higher at the decrease of temperature.
We measured the polarization of the PZT at different temperatures and with several cycles per each temperature. The I_G peaks, which correspond to the switch of the ferroelectric domains, are easily recognizable in figure 5.2. At room temperature the two peaks reach $I_G \simeq 33 \pm 2$ nA; with decreasing temperature the peaks reduce their maximum I_G: this is due to the lower mobility of the ferroelectric domains with decreasing temperature. Notice that the I_G peak magnitude depends also on how fast we increase and decrease V_G: the faster the electric field is applied, the higher the I_G peaks are. Thus, one may suggest to increase the V_G application rate; however, apart from the aforementioned issue with the parasitic capacitances, we noticed a considerable time delay of the domain switching after the application of the coercive field that results in a shift in the measured E_c towards higher values. Thus, again, a lower V_G rate is preferable. Finally, we notice also that the I_G peaks shift towards higher V_G values with decreasing T and that there is a small asymmetry between positive and negative applied V_G.
By integrating I_G with respect to time, we recover the D-E loops. However, in our measurements it is often present a constant off-set current that has to be subtracted from the I_G. Moreover, the wiring system of the cryocooler is not designed for the response in frequency of the experiments, thus, it is necessary to remove from the signal the parasitic contributions that arise from the parasitic capacitances.
By plotting the integrated I_G as function of the electric field E, we obtain the D-E loops (see figure 5.3.a).

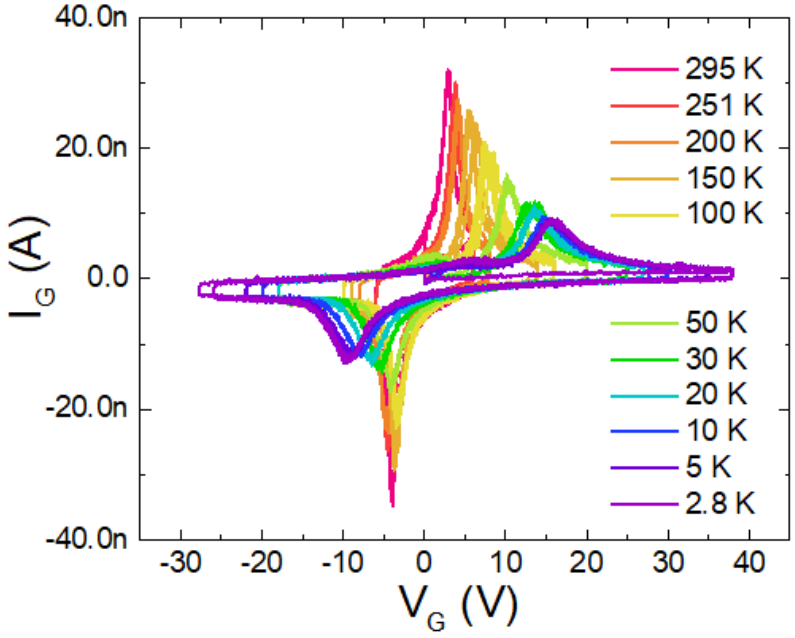

Figure 5.2: I_G vs. V_G for different temperature values. The V_G application range increases with decreasing temperature. The two peaks are not symmetric with respect to $V_G = 0$ V.

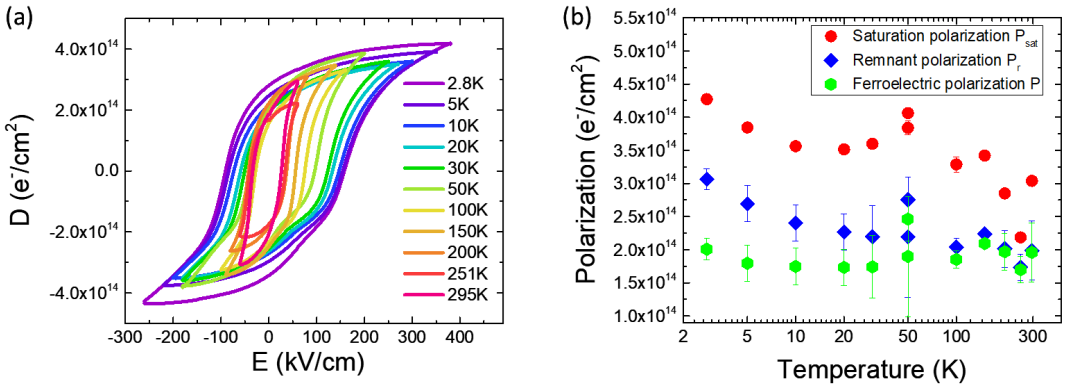

Figure 5.3: (a) The $D - E$ loops for different T. (b) The remnant polarization P_r, the saturation polarization P_{sat} and the pure ferroelectric polarization P as function of temperature.

The remnant polarization P_r is obtained as $D(E = 0$ kV/cm), while the saturation polarization P_{sat} is obtained as the maximum D value per each temperature.

The error bars are defined by considering the difference between the direct and inverse polarizations and the filled points represent the average of the two (see figure 5.3.b).
Referring to eq.1.28, we notice that the capacitive contribution to D at $E = 0$ kV/cm is null. However, the contribution due to the (very small) conductivity of PZT is not negligible. Thus, to obtain the contribution due to the pure ferroelectric polarization P, we need to subtract the third term in eq. 1.27. The conductance of the PZT layer is obtained as the overall slope of I_G vs. V_G curves (we consider only I_G vs. V_G for corresponding electric fields beyond E_c) and it turns to be $\sim 4 \cdot 10^{-11}$ S. Even if this value is particularly small, however the contribution to D due to the conductive current is the time integral of σE. However, since the V_G rate is low, the corresponding times are long, and, thus, the contribution of the conductance to D is considerable. Moreover, this contribution is considerably higher for low temperatures, since the V_G range is extended. All these considerations bring us to plot in figure 5.3 the values of the ferroelectric polarization P obtained by subtracting the resistive contribution from the remnant polarization P_r: this plot shows that the ferroelectric polarization is almost constant in the whole temperature range and its value is $\sim 2 \cdot 10^{14}$ e^-/cm^2. This is a very promising value in view of the possible application of this technique for inducing phase transitions in superconducting materials.
Despite such huge values reached by the ferroelectric polarization, the resistance modulation of gold films is always $\lesssim 0.5$ %, much lower than what we expect from a ~ 38 nm thick Au film for the same applied field [24]. Moreover, $\Delta R/R'$ is even smaller at low temperatures (see figure 5.4.b). Furthermore, at room temperature, we can easily recognize a hysteretic behaviour: this is expected, since the modulation of the resistance must follow the ferroelectric polarization.

5.1.3 The piezoelectric effect

When we apply very high gate voltages V_G, two main effects occur.
In one case, mostly seen at room temperature, a conducting current starts to flow through the dielectric medium. This phenomenon is reported as resistive switching: it stems from the presence of oxygen vacancies in the ferroelectric material which can move through the system forming conducting paths [212]. In this case, it is possible to return to the previous resistance values upon the removal of the V_G. It is also reasonable that we detected this phenomenon mostly at room temperature, where the atomic mobility in the PZT sample is higher. Such possibility is also at the basis of studies about using ferroelectric materials to fabricate memristors [213]. However, this effect is detrimental as far as our purpose is concerned. Thus, we limited the application of the V_G, avoiding to reach such high values.

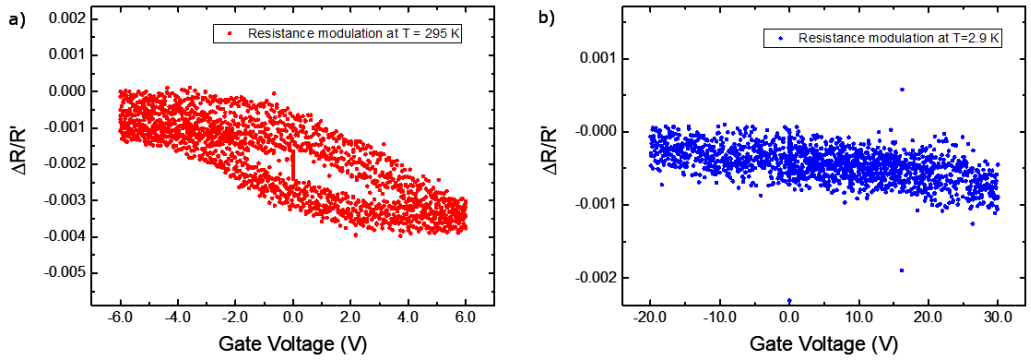

Figure 5.4: The resistance modulation of gold thin films at $T = 295$ K (a) and $T = 2.9$ K (b). It is extremely tiny with respect to the expected values. At lower temperatures, the resistance modulation is lower and we cannot recognize the domain switching.

On the other hand, we can explore wider V_G ranges going down in temperature. In this case, the effect of very high applied V_Gs is to activate the piezoelectric effect.

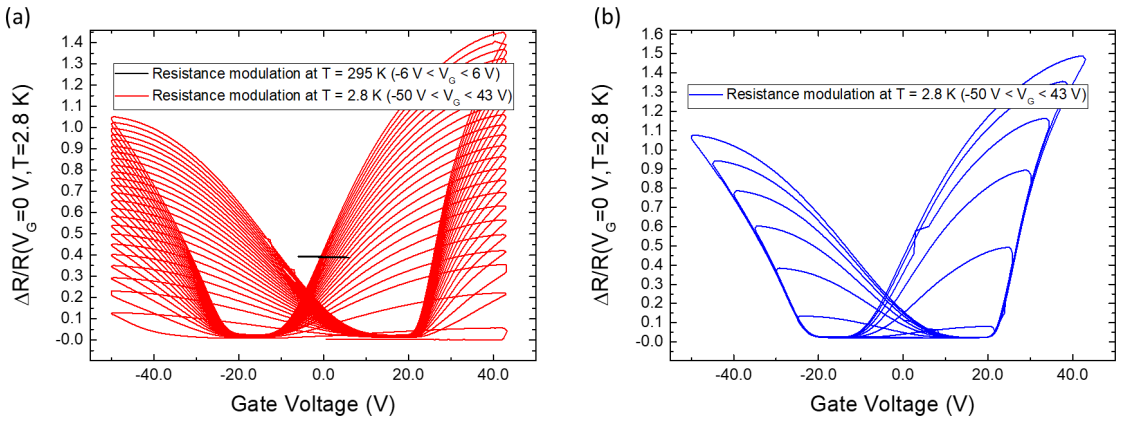

Figure 5.5: The resistance modulation of gold thin films due to the piezoelectric effect at $T = 2.8$ K. (a) Several consecutive cycles with fixed V_G range ($-50V \leq V_G \leq 43V$): $\Delta R/R'$ increases at each cycle (red lines). For comparison, the same data of figure 5.4a (-6 V $\leq V_G \leq$ 6 V) are reported in this scale (black lines). (b) Several consecutive cycles with reducing V_G range (from $-50V \leq V_G \leq 43V$ to $-6V \leq V_G \leq 6V$): $\Delta R/R'$ decreases at each cycle down to zero, returning to its original value at $T = 2.8$ K.

To do so, we went down to base temperature, and we pushed V_G up to 40 V. Since we can simultaneously measure the resistance of the gold film while applying V_G, we used the metallic film as a detector of the strain loop: indeed, in metals $\Delta R/R' \propto \Delta l/L$, being L the ferroelectric length and Δl the modulation of it. In our case, L is along the current flow direction. Figure 5.5.a shows what happens when the piezoelectric effect is measured: the resistance starts increasing at high V_G values, and then, with removing V_G, it returns to its original value with an hysteretic behaviour. We notice that the resistance modulation increases at each cycle, and the dependence of the resistance upon the cycling of the gate voltage, shows the characteristic butterfly loops.
At its maximum value $\Delta R/R' \gtrsim 1.4$ (i.e. the resistance increases $\gtrsim 140\%$ w.r.t. its original value). We attribute the increase of the resistance modulation with cycle repetition to a rearrangement of the domains that acquire more and more mobility under the electric field induced stress.
It is possible to return to the original R value by progressively depolarizing the piezoelectric medium. To do so, we perform several V_G cycles reducing the V_G range at each cycle (figure 5.3b shows this procedure). However, after the first high V_G application that led to the onset of the ferroelectric effect, the V_G threshold needed to activate the piezoelectric effect reduces dramatically.
Concluding, the piezoelectric effect is dominating on the ferroelectric one at high V_G values and as far as the modulation of the transport properties of the Au film are concerned. This implies that we must consider both the effects in trying to modulate the superconducting properties of an eventual superconductor deposited on top of the PZT layer.

5.2 Ionic gating in ultra-thin NbN films

After the characterization of the PZT ferroelectric and piezoelectric properties, we moved our attention to the possibility of modulating the superconducting properties of NbN ultra-thin films via ferroelectric gating.
Piatti *et al.* demonstrated that the modulation of the superconducting properties of NbN thin films by means of ionic gating is enhanced with reducing the film thickness [26, 27]. Thus, reducing the film thickness as much as possible could, in principle, lead to the possibility of modulating the SC properties of NbN even with the induced charge densities that we reached in our ferroelectric gating experiments in gold. This possibility could pave the way to very interesting applications, like the control of the superconducting state, via a solid gating device, operated at low temperatures. This fact, indeed, hints at the possibility to fabricate superconducting transistors with metastable phases, i.e. it could be possible to fabricate electronic paths in which superconductivity can be switched on and off as needed

and, probably, at high frequency.
For this reason, we used ultra-thin NbN films, grown by Marco Colangelo at the Massachusetts Institute of Technology, which thickness ranged between ~ 3.5 and ~ 5.8 nm. The films were grown on amorphous Si/SiO_2 substrates at room temperature by a DC reactive magnetron sputtering for a deposition time of 100 to 160 s. Subsequently, the films were patterned in the Hall bar geometry using a Heidelberg μPG 101 direct writer followed by reactive ion etching using CF_4.
We performed our experiments on four samples with different thicknesses. Measuring the thickness t of our ultra-thin NbN films is of fundamental importance for the purpose of our study, however it is often not straightforward [214] (e.g. AFM measurements would require additional fabrication steps). Fortunately, Medeiros *et al.* [214] reported a complete characterization of the t dependence on R_s^{-1} (being R_s the sheet resistance) in ultra-thin NbN films grown on Si/SiO_2 via the same fabrication process used in this work (see figure 5.6). Thus, to have a good estimation of our films thicknesses, we first measured the sheet resistance R_s of each sample (namely, $R_{s1} = 502\ \Omega/\square$; $R_{s2} = 614\ \Omega/\square$; $R_{s3} = 732\ \Omega/\square$; $R_{s4} = 916\ \Omega/\square$), then we related each R_s with the thickness t by exploiting the linear fitting curve in figure 5.6. Therefore, the film thicknesses are, respectively: $t_1 \simeq 5.8$ nm, $t_2 \simeq 4.9$ nm, $t_3 \simeq 4.2$ nm and $t_4 \simeq 3.5$ nm.

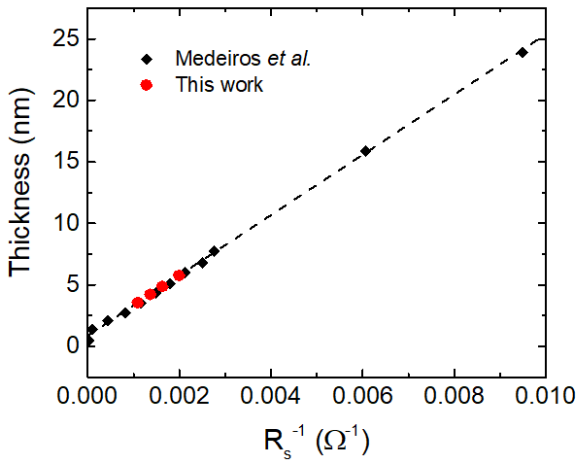

Figure 5.6: t dependence on R_s^{-1} for ultra-thin NbN films reported in Ref. [214] (black diamonds) and for our films (red dots). The black dashed line represents the linear fit of the black diamond points. The slope of the linear fit ($\simeq 245\ \mu\Omega$ cm) represents the resistivity ρ of the films, since, by definition, $R_s = \rho/t$. The red points are obtained by assuming that the t vs. R_s^{-1} points for our films would lie on the linear fitting curve.

We measured the resistance as function of temperature of each device with the

usual setup described in detail in the previous chapters; simultaneously, we performed ionic gating in order to understand the relation between the amount of charge induced at the film surface and the consequent T_c shift. We performed the experiments in a T range between 2.8 K and room temperature in the high vacuum chamber of the Cryomech® pulse-tube cryocooler.
As in Chapter 2, we used a reference ungated channel that acts as a very precise local temperature reference. This solution is mandatory to reliably determine small shifts in the SC transition temperature. In fact, we are expecting T_c shifts of the order of tens (or hundreds) of mK, since the thickness of these samples is reduced with respect to what previously studied in thicker samples (10-20 nm) [26, 27].
The active channel is covered by the electrolyte: we used a standard electrolyte DEME-TFSI to perform these experiments since it was found to be compatible with this material in earlier experiments [27]. The application of V_G occurs at $T = 220$ K, that is right above the glass temperature of the electrolyte.
Figure 5.7 shows the resistance modulation upon the application of three different V_G values: in all the cases we notice that the resistance does not return to its initial value upon the removal of V_G, but, instead, there is always an appreciable irreversible shift after the removal of V_G. In particular, for $V_G \leq -5$ V the resistance modulation is almost completely irreversible.

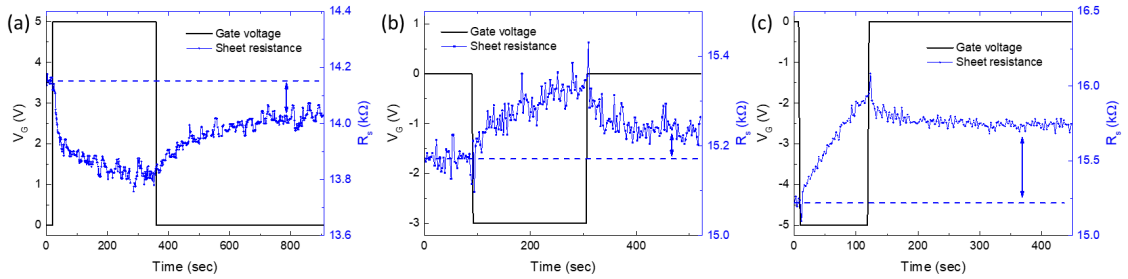

Figure 5.7: The resistance modulation due to the application of different V_G values on the thinner sample ($t_4 \simeq 3.5$ nm). Depending on the applied V_G, the modulation is almost reversible ((a) and (b)) or completely irreversible (c) for high values of negative V_G.

This fact leads to suspect the activation of electrochemical reactions at the surface between the sample and the electrolyte. However, as we mentioned before, the same electrolyte in thicker NbN samples is shown to act in a perfect electrostatic way, without the activation of electrochemical reactions. We preliminary address the change in the electrochemical behaviour to an enhanced reactivity at the surface due to the thinning of the sample.
The critical temperatures T_c[10] of these samples range from 4.5 K, for the $\simeq 3.5$ nm-thick sample, to 7.1 K, for the $\simeq 5.8$ nm-thick sample. These values are well

below the values reached in thicker samples [27], but, the reduction of T_c and its broadening are well-known effects of the reduction of film thickness. Moreover, we think that the amorphous substrate also plays a role in this degradation of T_c.
Figure 5.8 shows how the normalized resistance ($R/R(15K)$) as function of temperature is modulated by the application of the gate voltage.

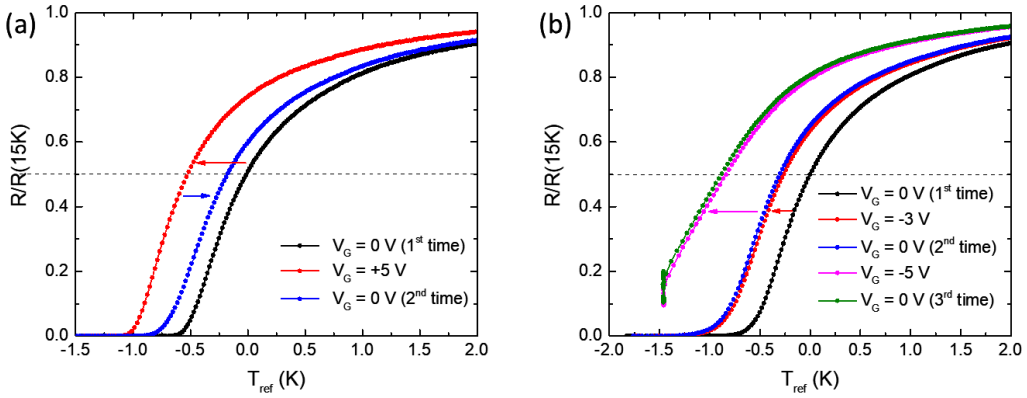

Figure 5.8: Referenced shift of the resistance as function of temperature upon the application of V_G for the $t_4 \simeq 3.5$ nm thick sample. The effect of application of positive V_G is almost reversible (a), while the application of negative V_G produces completely irreversible modifications of the superconductive transition. In the figure, the T scale is referenced to the midpoint of the transition in the reference channel. The legend of each panel tells the time ordering of the measurements, and the arrows suggests the time progress of the measurements.

The application of positive V_G leads to a maximum registered T_c shift of $\sim$ 600 mK, about 8-10 times larger than the ones obtained on 10-20 nm-thick films (60-80 mK) [27]. The T_c reduction is not entirely reversible upon removal of V_G.
The application of negative V_G leads to unexpected effects like the T_c decrease (opposite of what we observed in thicker films [27]) and the complete irreversibility of the shift (at anyV_G). In addition the SC transition shape is broadened (again, in contrast with what was observed in films thicker than 20 nm). This confirms the results on resistance shown above and suggests that electrochemical reactions occur when the anions go to the surface of NbN.
In films thicker than ours, with thickness equal or larger than 20 nm, the T_c modulation was completely reversible; while an irreversible, hysteretic behaviour was observed only by thinning the thickness down to 10 nm [27].
We determined the induced charge density Δn_{2D} via double-step chronocoulometry. In figure 5.9a we notice that Δn_{2D} reaches larger values for $V_G > 0$ (electron accumulation), as was observed in thicker films. However, the maximum values of

Δn_{2D} are much smaller than the ones obtained on thicker films, implying a suppressed EDL capacitance.

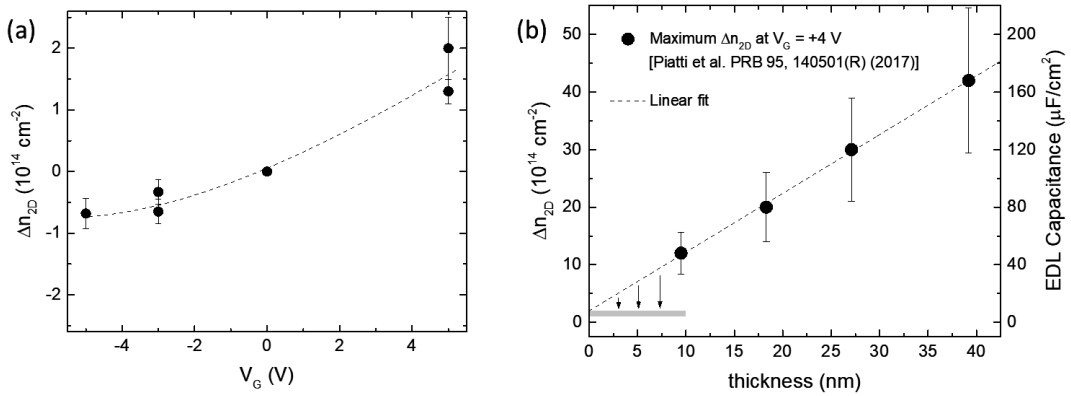

Figure 5.9: (a) Surface induced charge density Δn_{2D} as function of V_G for our NbN thinner sample. (b) comparison between Δn_{2D} trend as function of the thickness in thicker samples (black filled dots, Ref. [27]) and in our ultrathin films (gray band). The dashed line is a guide to the eye that shows the expected trend at low thickness; the arrows stress the difference between the expected trend and our results.

A progressive suppression of the EDL capacitance was already observed in thicker films; however, the capacitance (and consequently the maximum Δn_{2D}) in these ultrathin films (shaded grey band in figure 5.9b) is significantly below the trend expected from a simple linear extrapolation of the data for thicker films [27].
Finally, we notice that this suppressed Δn_{2D} is comparable to that which we obtained via ferroelectric gating on gold, as we expected.
Moreover, here we would like to point out that, with respect to what happens in the case of electrochemical gating, in ferroelectric gating we would not have to face problems with the electrochemical interactions between the ionic liquid and the sample surface, that actually seems to be what hampers the possibility of reversibly tuning SC in such thin samples.
We notice that, also in the case of our thickest sample ($t_1 \simeq 5.8$ nm), the behaviour is exactly the same. Figure 5.10 shows that a considerable T_c shift is also present in this sample, even though it is reduced of a factor 10; the reduction is expected since as observed in thicker films, reducing the film thickness enhances the T_c shift for comparable values of Δn_{2D} . However the maximum Δn_{2D} is still comparable with the previous results.

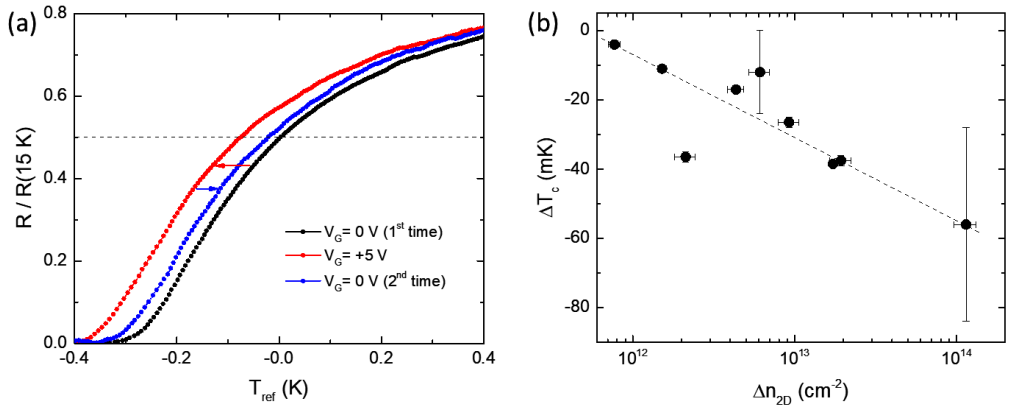

Figure 5.10: (a) Normalized resistance ($R/R(15K)$) as function of T upon the application of $V_G = +5$ V for the thickest sample ($t_1 \simeq 5.8$ nm. The figure shows R vs. T before (black dots), during (red dots) and after (blue dots) V_G application. (b) T_c shifts (ΔT_c) as function of the surface induced charge density Δn_{2D}. The dashed line is a guide to the eye.

5.2.1 Conclusions of the ionic-gating preliminary experiments on ultrathin NbN films

Experiments on ultrathin NbN films confirm a few results obtained on thicker films, such as that reducing sample thickness enhances the T_c shift, the electron accumulation suppresses T_c and, most importantly, that NbN films thinner than $\sim$ 10 nm show a strongly hysteretic behaviour. Moreover, thinner NbN films feature a smaller EDL capacitance. We also observed the presence of new features including the irreversible suppression of T_c upon electron depletion and an unexpected magnitude of the reduction in the EDL capacitance for thinner films.
The hysteretic behaviour may be due to electrostriction effects, if the film has an optimized but metastable structure which the electric field forces to relax, or to electrochemical interactions with the surface, if – for some reason – the surface of these ultra-thin films is more sensitive to the environment with respect to our earlier thicker films, or even to field-induced nitrogen migration which could be enhanced in non-stoichiometric samples [215].
Overall, ionic gating is not a suitable tool to reliably modify the properties of bare ultra-thin NbN films. However, the sizeable T_c shifts up to 0.6 K obtained at modest induced charge densities of 10^{14} cm^{-2} suggest that superconductivity in ultra-thin NbN film can be successfully tuned by less invasive gating techniques, such as standard solid gating (by using special high-ϵ_r dielectrics) or ferroelectric gating (by eliminating or, at least, strongly reducing the issues related to the piezoelectric effects), which can be operated at cryogenic temperatures (unlike the ionic

gating technique).

5.3 Conclusion

Concluding this chapter, we showed how a thin PZT film ($\sim$ 1 μm thick) can modulate the resistance of a gold thin film by exploiting the piezoelectric and the ferroelectric effect. We also find out that, once the piezoelectric effect is activated, it strongly overcomes the electrostatic modulation of the resistance operated by the ferroelectric gating.
On the second part of this chapter, we explored the ionic-gating technique applied to ultrathin NbN films. An unwanted consequence of reducing the film thickness is to render the sample more sensitive to effects that go beyond the electrostatic modulation of the charge density, but, as expected, it enhances the T_c shift magnitude.
Moreover, the surface induced charge density that is responsible for these T_c shifts is also comparable with what we found in our experiments on PZT.
Concluding, the possibility of using ferroelectric materials to tune SC seems to be reliable. Pros are that we do not incur in electrochemical reactions and that we can modulate SC even at low temperatures. Cons are that, most likely, and without specific (maybe complex) solutions, piezoelectric effects can be dominant over the ferroelectric ones. However we think that the results shown in this chapter could open the way to interesting developments of the subject in the near future.

Conclusion and perspectives

In this doctoral thesis we exploited the electric field effect to study and, potentially, modulate the transport properties of several disordered materials in thin film form. We had different goals and different results for each system we investigated. Moreover, we exploited three different techniques to perform field-effect experiments: the solid-gating, the ionic-gating and the ferroelectric-gating techniques.
Here we want to briefly summarize by points what was found for each system and the possible perspectives.

- We performed ionic-gating experiments on optimally P-doped Ba-122 ultrathin films aiming at modulating the superconducting properties of the system. The electrostatic modulation of the charge density at the surface has driven to an ambipolar suppression of T_c; we thus concluded that the system is already optimized for SC and any further change to the carrier density hampers T_c. However, underdoped P-doped Ba-122 ultrathin films are expected to increase T_c upon an electrostatic charge density modulation. Thus, interesting perspectives are open for the experiments in underdoped P-doped Ba-122 ultrathin films. The key findings of this work have been published in Ref. [73].

- We used the ionic-gating technique also on B-doped nanocrystalline diamond thin films, aiming at inducing insulator-to-metal and/or even SC transitions in slightly doped thin films. We found that a transition occurs in the surface conducting layer from variable-range hopping to the quantum critical regime, but never reaching the MIT; moreover, resistivity measurements show no evidence of a SC phase down to ~ 3 K. We attribute the impossibility of reaching the MIT transition to the high level of disorder. Thus, in perspective, the idea is to perform ionic-gating experiments on single crystal diamond thin films B-doped in a very thin layer at the surface. We performed preliminary experiments towards that direction, unfortunately showing that the maximum induced charge density is not yet sufficient to induce MIT in films with different crystallographic directions. However, the B-doped delta-layer in these

cases was extremely thin ($\sim$ 2 nm). We believe that a thicker B-doped delta-layer is probably necessary in order to induce (and maybe boost) SC by ionic gating in diamond. The key findings of this work have been published in Ref. [150].

- Then we characterized the transport properties of ink-jet printed graphene and MXene (Ti_3C_2) disordered thin films exploiting the solid-gating technique. We obtained reliable measurements of the mobility for both the systems. In graphene-ink films the mobility resulted to be orders of magnitude lower than in graphene. We have shown that the conduction is dominated by the network, and not by the single flakes properties, showing that the transport regime is a variable range hopping in 3D. Oppositely, in inkjet-printed MXene thin films we measured a 2D metallic conduction dominated by the properties of the single flakes, and not by the 3D network. This latter result suggests that the interesting characteristic of other inkjet-printed MXene films can be studied by the same technique, including the recently discovered superconducting properties of similar 2D materials (e.g. αMo_2C and Nb_2C).

- Finally, we investigated the feasibility of the use of ferroelectric materials to electrostatically tune the superconducting properties of ultrathin NbN films at low temperatures. To do so, we performed preliminary experiments of ferroelectric gating with PZT in gold reaching an electrostatic surface-induced charge density up to $\sim 10^{14}$ cm^{-2}; however piezoelectric effect dominates the transport properties modulation at high gate voltage. On the other hand, we performed preliminary ionic-gating experiments on ultrathin NbN films, going beyond the limits of previous works as far as the T_c shifts are concerned, and, simultaneously, reaching these values by a far lower surface-induced charge density ($\lesssim 10^{14}$ cm^{-2}). Both these results seem to prove the feasibility of a low-temperature tuning of the SC in these systems by ferroelectric gating once the piezoelectric effects will be properly reduced. Experiments on this direction are already ongoing.

Bibliography

1. Lilienfeld, J. E. US1745175A (1926).
2. Kahng, D. US3102230A (1963).
3. Atalla, M. M., Tannenbaum, E. & Scheibner, E. Stabilization of silicon surfaces by thermally grown oxides. *Bell System Technical Journal* **38,** 749–783 (1959).
4. Sze, S. M. & Ng, K. K. *Physics of semiconductor devices* (John wiley & sons, 2006).
5. Weimer, P. K. The TFT a new thin-film transistor. *Proceedings of the IRE* **50,** 1462–1469 (1962).
6. Fortunato, E., Barquinha, P. & Martins, R. Oxide semiconductor thin-film transistors: a review of recent advances. *Advanced materials* **24,** 2945–2986 (2012).
7. Novoselov, K., Mishchenko, A., Carvalho, A. & Neto, A. C. 2D materials and van der Waals heterostructures. *Science* **353,** aac9439 (2016).
8. Fatemi, V. *et al.* Electrically tunable low-density superconductivity in a monolayer topological insulator. *Science* **362,** 926–929 (2018).
9. Daghero, D. *et al.* Large conductance modulation of gold thin films by huge charge injection via electrochemical gating. *Physical review letters* **108,** 066807 (2012).
10. Ueno, K. *et al.* Field-induced superconductivity in electric double layer transistors. *Journal of the Physical Society of Japan* **83,** 032001 (2014).
11. Huang, A. P., Yang, Z. & Chu, P. K. in *Advances in solid state circuit technologies* (IntechOpen, 2010).
12. Ye, J. *et al.* Liquid-gated interface superconductivity on an atomically flat film. *Nature materials* **9,** 125 (2010).
13. Yuan, H. *et al.* High-density carrier accumulation in ZnO field-effect transistors gated by electric double layers of ionic liquids. *Advanced Functional Materials* **19,** 1046–1053 (2009).

14. Ueno, K. *et al.* Electric-field-induced superconductivity in an insulator. *Nature materials* **7,** 855 (2008).

15. Shi, W. *et al.* Superconductivity series in transition metal dichalcogenides by ionic gating. *Scientific reports* **5,** 12534 (2015).

16. Yu, Y. *et al.* Gate-tunable phase transitions in thin flakes of 1T-TaS_2. *Nature nanotechnology* **10,** 270 (2015).

17. Maruyama, S. *et al.* Reversible electrochemical modulation of the superconducting transition temperature of LiTi2O4 ultrathin films by ionic liquid gating. *Applied Physics Letters* **107,** 142602 (2015).

18. Jeong, J. *et al.* Suppression of metal-insulator transition in VO2 by electric field–induced oxygen vacancy formation. *Science* **339,** 1402–1405 (2013).

19. Li, M. *et al.* Suppression of ionic liquid gate-induced metallization of SrTiO3 (001) by oxygen. *Nano letters* **13,** 4675–4678 (2013).

20. Schladt, T. D. *et al.* Crystal-facet-dependent metallization in electrolyte-gated rutile TiO2 single crystals. *ACS nano* **7,** 8074–8081 (2013).

21. Walter, J., Wang, H., Luo, B., Frisbie, C. D. & Leighton, C. Electrostatic versus electrochemical doping and control of ferromagnetism in ion-gel-gated ultrathin La0. 5Sr0. 5CoO3- δ. *ACS nano* **10,** 7799–7810 (2016).

22. Shiogai, J., Ito, Y., Mitsuhashi, T., Nojima, T. & Tsukazaki, A. Electric-field-induced superconductivity in electrochemically etched ultrathin FeSe films on SrTiO3 and MgO. *Nature Physics* **12,** 42 (2016).

23. Yoshida, M., Ye, J., Nishizaki, T., Kobayashi, N. & Iwasa, Y. Electrostatic and electrochemical tuning of superconductivity in two-dimensional NbSe2 crystals. *Applied Physics Letters* **108,** 202602 (2016).

24. Sola, A. *Surface charge doping by polymer electrolyte gating in metals and superconductors* Ph.D. (Politecnico di Torino, 2013).

25. Stojek, Z. in *Electroanalytical methods* 3–9 (Springer, 2010).

26. Piatti, E. *et al.* Superconducting transition temperature modulation in NbN via EDL gating. *Journal of Superconductivity and Novel Magnetism* **29,** 587–591 (2016).

27. Piatti, E. *et al.* Control of bulk superconductivity in a BCS superconductor by surface charge doping via electrochemical gating. *Physical Review B* **95,** 140501 (2017).

28. Nakano, M. *et al.* Collective bulk carrier delocalization driven by electrostatic surface charge accumulation. *Nature* **487,** 459 (2012).

29. Galperin, Y. M., German, E. & Karpov, V. Hall effect under hopping conduction conditions. *Sov. Phys. JETP* **72,** 193–200 (1991).

30. Yang, H. *et al.* Fully band-resolved scattering rate in MgB_2 revealed by the nonlinear hall effect and magnetoresistance measurements. *Physical review letters* **101,** 067001 (2008).

31. Zhang, X., Yu, L., von Molnár, S., Fisk, Z. & Xiong, P. Nonlinear Hall Effect as a Signature of Electronic Phase Separation in the Semimetallic Ferromagnet EuB_6. *Physical review letters* **103,** 106602 (2009).

32. Scholz, F. *et al. Electroanalytical methods* (Springer, 2010).

33. http://link.aps.org/supplemental/10.1103/PhysRevMaterials.3.044801.

34. Takahashi, M. & Sakai, S. in *Ferroelectric-Gate Field Effect Transistor Memories: Device Physics and Applications* 23–56 (Springer, 2016).

35. IEEE Standard on Piezoelectricity. *ANSI/IEEE Std 176-1987* (1988).

36. Sirohi, J. & Chopra, I. Fundamental understanding of piezoelectric strain sensors. *Journal of intelligent material systems and structures* **11,** 246–257 (2000).

37. Yan, H. *et al.* The contribution of electrical conductivity, dielectric permittivity and domain switching in ferroelectric hysteresis loops. *Journal of Advanced Dielectrics* **1,** 107–118 (2011).

38. Chandra, P. & Littlewood, P. B. in *Physics of ferroelectrics* 69–116 (Springer, 2007).

39. Landau, L. D. On the theory of phase transitions. *Phys. Z. Sowjun.* ***11****, 26 , 545 (1937); Zh. Eksp. Teor. Fiz.* ***7*** *627 (1937).*

40. Devonshire, A. F. XCVI. Theory of barium titanate: Part I. *The London, Edinburgh, and Dublin Philosophical Magazine and Journal of Science* **40,** 1040–1063 (1949).

41. Devonshire, A. CIX. Theory of barium titanate—Part II. *The London, Edinburgh, and Dublin Philosophical Magazine and Journal of Science* **42,** 1065–1079 (1951).

42. Devonshire, A. Theory of ferroelectrics. *Advances in physics* **3,** 85–130 (1954).

43. Stewart, M., Cain, M. & Hall, D. *Ferroelectric hysteresis measurement and analysis* (National Physical Laboratory Teddington, 1999).

44. Jiang, W., Zhou, S., Li, X. & Shui, Y. *The second harmonic generation in piezoelectric resonators* in *1994 Proceedings of IEEE Ultrasonics Symposium* **2** (1994), 969–972.

45. Segouin, V., Kaeswurm, B., Webber, K. G. & Daniel, L. Temperature-dependent anhysteretic behavior of co-doped PZT. *Journal of Applied Physics* **124,** 104103 (2018).

46. Kamihara, Y. *et al.* Iron-based layered superconductor: LaOFeP. *Journal of the American Chemical Society* **128,** 10012–10013 (2006).

47. Kamihara, Y., Watanabe, T., Hirano, M. & Hosono, H. Iron-based layered superconductor $La[O_{1-x}F_x]FeAs$ (x= 0.05 - 0.12) with T_c= 26 K. *Journal of the American Chemical Society* **130,** 3296–3297 (2008).

48. Ishida, K., Nakai, Y. & Hosono, H. To what extent iron-pnictide new superconductors have been clarified: a progress report. *Journal of the Physical Society of Japan* **78,** 062001 (2009).

49. Luo, X., Wu, T. & Chen, X. in *Iron-Based Superconductivity* 21–71 (Springer, 2015).

50. Ogino, H. *et al.* Homologous series of iron pnictide oxide superconductors $(Fe_2As_2)[Ca_{n+1}(Sc,Ti)_nO_y]$(n= 3, 4, 5) with extremely thick blocking layers. *Applied Physics Letters* **97,** 072506 (2010).

51. Ogino, H. *et al.* A new homologous series of iron pnictide oxide superconductors $(Fe_2As_2)(Ca_{n+2}(Al,Ti)_nO_y)$(n= 2, 3, 4). *Superconductor Science and Technology* **23,** 115005 (2010).

52. Ogino, H. *et al.* Superconductivity above 40 K observed in a new iron arsenide oxide $(Fe_2As_2)(Ca_4(Mg,Ti)_3O_y)$. *Applied physics express* **3,** 063103 (2010).

53. Hosono, H., Yamamoto, A., Hiramatsu, H. & Ma, Y. Recent advances in iron-based superconductors toward applications. *Materials today* **21,** 278–302 (2018).

54. Jiang, S. *et al.* Superconductivity up to 30 K in the vicinity of the quantum critical point in $BaFe_2(As_{1-x}P_x)_2$. *Journal of Physics: Condensed Matter* **21,** 382203 (2009).

55. Imai, Y., Sawada, Y., Nabeshima, F. & Maeda, A. Suppression of phase separation and giant enhancement of superconducting transition temperature in $FeSe_{1-x}Te_x$ thin films. *Proceedings of the National Academy of Sciences* **112,** 1937–1940 (2015).

56. Lei, B. *et al.* Evolution of high-temperature superconductivity from a low-T_c phase tuned by carrier concentration in FeSe thin flakes. *Physical review letters* **116,** 077002 (2016).

57. Hanzawa, K., Sato, H., Hiramatsu, H., Kamiya, T. & Hosono, H. Electric field-induced superconducting transition of insulating FeSe thin film at 35 K. *Proceedings of the National Academy of Sciences* **113,** 3986–3990 (2016).

58. Miyakawa, T. *et al.* Enhancement of superconducting transition temperature in FeSe electric-double-layer transistor with multivalent ionic liquids. *Physical Review Materials* **2,** 031801 (2018).

59. Kouno, S. *et al.* Superconductivity at 38 K at an electrochemical interface between an ionic liquid and $FeSe_{0.8}$ $Te_{0.2}$ on various substrates. *Scientific reports* **8,** 14731 (2018).

60. Hiramatsu, H., Katase, T., Kamiya, T., Hirano, M. & Hosono, H. Water-induced superconductivity in $SrFe_2As_2$. *Physical Review B* **80,** 052501 (2009).

61. Takahashi, H. *et al.* Superconductivity at 43 K in an iron-based layered compound $LaO_{1-x}F_xFeAs$. *Nature* **453,** 376 (2008).

62. Fujioka, M. *et al.* Phase diagram and superconductivity at 58.1 K in α-FeAs-free $SmFeAsO_{1-x}F_x$. *Superconductor Science and Technology* **26,** 085023 (2013).

63. Lebegue, S. Electronic structure and properties of the Fermi surface of the superconductor LaOFeP. *Physical Review B* **75,** 035110 (2007).

64. Ding, H. *et al.* Observation of Fermi-surface-dependent nodeless superconducting gaps in $Ba_{0.6}K_{0.4}Fe_2As_2$. *EPL (Europhysics Letters)* **83,** 47001 (2008).

65. Coldea, A. *et al.* Fermi surface of superconducting LaFePO determined from quantum oscillations. *Physical review letters* **101,** 216402 (2008).

66. Sugawara, H. *et al.* de Haas-van Alphen effect in LaFePO with two-dimensional cylindrical Fermi surfaces. *Journal of the Physical Society of Japan* **77,** 113711 (2008).

67. Singh, D. J. & Du, M.-H. Density functional study of $LaFeAsO_{1-x}F_x$: A low carrier density superconductor near itinerant magnetism. *Physical Review Letters* **100,** 237003 (2008).

68. Singh, D. J. Electronic structure and doping in $BaFe_2As_2$ and LiFeAs: Density functional calculations. *Physical Review B* **78,** 094511 (2008).

69. Rotter, M., Tegel, M. & Johrendt, D. Superconductivity at 38 K in the iron arsenide $(Ba_{1-x}K_x)Fe_2As_2$. *Physical Review Letters* **101,** 107006 (2008).

70. Dong, J. *et al.* Competing orders and spin-density-wave instability in $La(O_{1-x}F_x)FeAs$. *EPL (Europhysics Letters)* **83,** 27006 (2008).

71. Avci, S. *et al.* Phase diagram of $Ba_{1-x}K_xFe_2As_2$. *Physical Review B* **85,** 184507 (2012).

72. Analytis, J., Chu, J.-H., McDonald, R., Riggs, S. & Fisher, I. Enhanced Fermi-surface nesting in superconducting $BaFe_2(As_{1-x}P_x)_2$ revealed by the de Haas-van Alphen effect. *Physical review letters* **105,** 207004 (2010).

73. Piatti, E. *et al.* Ambipolar suppression of superconductivity by ionic gating in optimally doped BaFe2(As, P)2 ultrathin films. *Physical Review Materials* **3,** 1–10 (2019).

74. Kawaguchi, T. *et al.* The strain effect on the superconducting properties of $BaFe_2(As,P)_2$ thin films grown by molecular beam epitaxy. *Superconductor Science and Technology* **27,** 065005 (2014).

75. Kasahara, S. *et al.* Evolution from non-Fermi-to Fermi-liquid transport via isovalent doping in $BaFe_2(As_{1-x}P_x)_2$ superconductors. *Physical Review B* **81,** 184519 (2010).

76. Daghero, D. *et al.* Effect of ion irradiation on surface morphology and superconductivity of $BaFe_2(As_{1-x}P_x)_2$ films. *Applied Surface Science* **395,** 9–15 (2017).

77. Täubert, C., Fleischhammer, M., Wohlfahrt-Mehrens, M., Wietelmann, U. & Buhrmester, T. LiBOB as electrolyte salt or additive for lithium-ion batteries based on $LiNi_{0.8}Co_{0.15}Al_{0.05}O_2$/graphite. *Journal of The Electrochemical Society* **157,** A721–A728 (2010).

78. Xu, K., Zhang, S. & Jow, T. R. LiBOB as additive in LiPF6-based lithium ion electrolytes. *Electrochemical and Solid-State Letters* **8,** A365–A368 (2005).

79. Jow, T. *et al.* LiBOB-based electrolytes for Li-ion batteries for transportation applications. *Journal of The Electrochemical Society* **151,** A1702–A1706 (2004).

80. Lee, S. *et al.* Artificially engineered superlattices of pnictide superconductors. *Nature materials* **12,** 392 (2013).

81. Eom, C. (private communication).

82. Likharev, K. Superconducting weak links. *Reviews of Modern Physics* **51,** 101 (1979).

83. Claassen, J. Josephson behavior in granular NbN weak links. *Applied Physics Letters* **36,** 771–773 (1980).

84. Plecenik, T. *et al.* Surface transport properties of Fe-based superconductors: The influence of degradation and inhomogeneity. *Applied Physics Letters* **103,** 052601 (2013).

85. Piatti, E., Romanin, D., Gonnelli, R. S. & Daghero, D. Anomalous screening of an electrostatic field at the surface of niobium nitride. *Applied Surface Science* **461,** 17–22 (2018).

86. Ummarino, G. *et al.* Proximity Eliashberg theory of electrostatic field-effect doping in superconducting films. *Physical Review B* **96,** 064509 (2017).

87. *Coulomb Screening by Mobile Charges: Applications to Materials Science, Chemistry, and Biology* (Springer, New York, 1999).

88. Sengwa, R. J., Kaur, K. & Chaudhary, R. Dielectric properties of low molecular weight poly (ethylene glycol) s. *Polymer international* **49,** 599–608 (2000).

89. Russel, W., Saville, D. & Schowalter, W. *Colloidal dispersions* (Cambridge university press, 1991).

90. Tortello, M. *et al.* Huge field-effect surface charge injection and conductance modulation in metallic thin films by electrochemical gating. *Applied Surface Science* **269,** 17–22 (2013).

91. Choi, J. *et al.* Electrical modulation of superconducting critical temperature in liquid-gated thin niobium films. *Applied Physics Letters* **105,** 012601 (2014).

92. Saito, Y. & Iwasa, Y. Ambipolar insulator-to-metal transition in black phosphorus by ionic-liquid gating. *ACS nano* **9,** 3192–3198 (2015).

93. Min, K.-J., Park, J., Kim, W.-S. & Chae, D.-H. Asymmetric Electron-Hole Decoherence in Ion-Gated Epitaxial Graphene. *Scientific reports* **7,** 12130 (2017).

94. Piatti, E. *et al.* Carrier mobility and scattering lifetime in electric double-layer gated few-layer graphene. *Applied Surface Science* **395,** 37–41 (2017).

95. Gonnelli, R. *et al.* Weak localization in electric-double-layer gated few-layer graphene. *2D Materials* **4,** 035006 (2017).

96. Piatti, E., Chen, Q. & Ye, J. Strong dopant dependence of electric transport in ion-gated MoS_2. *Applied Physics Letters* **111,** 013106 (2017).

97. Piatti, E., Chen, Q., Tortello, M., Ye, J. & Gonnelli, R. S. Possible charge-density-wave signatures in the anomalous resistivity of Li-intercalated multilayer MoS_2. *Applied Surface Science* **461,** 269–275 (2018).

98. Zhang, S. *et al.* Electric Field Induced Permanent Superconductivity in Layered Metal Nitride Chlorides HfNCl and ZrNCl. *Chinese Physics Letters* **35,** 097401 (2018).

99. De Jong, S. *et al.* High-resolution, hard x-ray photoemission investigation of $BaFe_2As_2$: Moderate influence of the surface and evidence for a low degree of Fe 3d As 4p hybridization of electronic states near the Fermi energy. *Physical Review B* **79,** 115125 (2009).

100. McLeod, J. A. *et al.* Effect of 3d doping on the electronic structure of $BaFe_2As_2$. *Journal of Physics: Condensed Matter* **24,** 215501 (2012).

101. Lu, N. *et al.* Electric-field control of tri-state phase transformation with a selective dual-ion switch. *Nature* **546,** 124 (2017).

102. Li, Z. *et al.* Electric-field Control of Magnetism with Emergent Topological Hall Effect in SrRuO3 through Proton Evolution. *arXiv preprint arXiv:1811.10794* (2018).

103. Fête, A., Rossi, L., Augieri, A. & Senatore, C. Ionic liquid gating of ultra-thin $YBa_2Cu_3O_{7-x}$ films. *Applied Physics Letters* **109,** 192601 (2016).

104. Paolucci, F. *et al.* Magnetotransport Experiments on Fully Metallic Superconducting Dayem-Bridge Field-Effect Transistors. *Physical Review Applied* **11,** 024061 (2019).

105. Ramos-Álvarez, A. *et al.* Superconducting fluctuations in isovalently substituted BaFe 2 (As 1- x P x) 2: Possible observation of multiband effects. *Physical Review B* **92,** 094508 (2015).

106. Brumme, T., Calandra, M. & Mauri, F. First-principles theory of field-effect doping in transition-metal dichalcogenides: Structural properties, electronic structure, Hall coefficient, and electrical conductivity. *Physical Review B* **91,** 155436 (2015).

107. Gallagher, P. *et al.* A high-mobility electronic system at an electrolyte-gated oxide surface. *Nature communications* **6,** 6437 (2015).

108. Ovchinnikov, D. *et al.* Disorder engineering and conductivity dome in ReS_2 with electrolyte gating. *Nature communications* **7,** 12391 (2016).

109. Petach, T. A. *et al.* Disorder from the bulk ionic liquid in electric double layer transistors. *ACS nano* **11,** 8395–8400 (2017).

110. Lu, J. *et al.* Full superconducting dome of strong Ising protection in gated monolayer WS_2. *Proceedings of the National Academy of Sciences* **115,** 3551–3556 (2018).

111. Piatti, E. *et al.* Multi-valley superconductivity in ion-gated MoS_2 layers. *Nano letters* **18,** 4821–4830 (2018).

112. Mizukami, Y. *et al.* Disorder-induced topological change of the superconducting gap structure in iron pnictides. *Nature communications* **5,** 5657 (2014).

113. Daghero, D. *et al.* Decoupling of critical temperature and superconducting gaps in irradiated films of a Fe-based superconductor. *Superconductor Science and Technology* **31,** 034005 (2018).

114. Colombier, E. *et al.* Electrical transport measurements under pressure for $BaFe_2As_2$ compounds doped with Co, Cr, or Sn. *Superconductor Science and Technology* **23,** 054003 (2010).

115. Torikachvili, M., Bud'ko, S., Ni, N. & Canfield, P. Effect of pressure on the structural phase transition and superconductivity in $(Ba_{1-x}K_x)Fe_2As_2 (x= 0$ and 0.45) and $SrFe_2$ As_2 single crystals. *Physical Review B* **78,** 104527 (2008).

116. Hassinger, E. *et al.* Pressure-induced Fermi-surface reconstruction in the iron-arsenide superconductor $Ba_{1-x}K_xFe_2As_2$: Evidence of a phase transition inside the antiferromagnetic phase. *Physical Review B* **86,** 140502 (2012).

117. E. Klintberg, L. *et al.* Chemical Pressure and Physical Pressure in $BaFe_2(As_{1-x}P_x)_2$. *Journal of the Physical Society of Japan* **79,** 123706 (2010).

118. Zinth, V. & Johrendt, D. The interplay of electron doping and chemical pressure in $Ba(Fe_{1-y}Co_y)_2(As_{1-x}P_x)_2$. *EPL (Europhysics Letters)* **98,** 57010 (2012).

119. Katase, T., Sato, H., Hiramatsu, H., Kamiya, T. & Hosono, H. Unusual pressure effects on the superconductivity of indirectly electron-doped $(Ba_{1-x}La_x)$ Fe_2 As_2 epitaxial films. *Physical Review B* **88,** 140503 (2013).

120. Kimber, S. A. *et al.* Similarities between structural distortions under pressure and chemical doping in superconducting $BaFe_2As_2$. *Nature materials* **8,** 471 (2009).

121. Zhu, C. *et al.* Tuning electronic properties of $FeSe_{0.5}Te_{0.5}$ thin flakes using a solid ion conductor field-effect transistor. *Physical Review B* **95,** 174513 (2017).

122. Pan, L. S. & Kania, D. R. *Diamond: electronic properties and applications* (Springer Science & Business Media, 2013).

123. Ekimov, E. *et al.* Superconductivity in diamond. *nature* **428,** 542 (2004).

124. Bustarret, E. *et al.* Dependence of the superconducting transition temperature on the doping level in single-crystalline diamond films. *Physical review letters* **93,** 237005 (2004).

125. Yokoya, T. *et al.* Origin of the metallic properties of heavily boron-doped superconducting diamond. *Nature* **438,** 647 (2005).

126. Takano, Y. *et al.* Superconductivity in diamond thin films well above liquid helium temperature. *Applied physics letters* **85,** 2851–2853 (2004).

127. Ishizaka, K. *et al.* Observation of a superconducting gap in boron-doped diamond by laser-excited photoemission spectroscopy. *Physical review letters* **98,** 047003 (2007).

128. Bustarret, E. Superconducting diamond: an introduction. *physica status solidi (a)* **205,** 997–1008 (2008).

129. Okazaki, H. *et al.* Signature of high T_c above 25 K in high quality superconducting diamond. *Applied physics letters* **106,** 052601 (2015).

130. Boeri, L., Kortus, J. & Andersen, O. Three-Dimensional MgB_2-Type Superconductivity in Hole-Doped Diamond. *Physical review letters* **93,** 237002 (2004).

131. Lee, K. & Pickett, W. E. Superconductivity in boron-doped diamond. *Physical review letters* **93,** 237003 (2004).

132. Boeri, L., Kortus, J. & Andersen, O. Electron-phonon superconductivity in hole-doped diamond: A first-principles study. *Journal of Physics and Chemistry of Solids* **67,** 552–556 (2006).

133. Giustino, F., Yates, J. R., Souza, I., Cohen, M. L. & Louie, S. G. Electron-phonon interaction via electronic and lattice Wannier functions: Superconductivity in boron-doped diamond reexamined. *Physical review letters* **98,** 047005 (2007).

134. Landstrass, M. & Ravi, K. V. Resistivity of chemical vapor deposited diamond films. *Applied Physics Letters* **55,** 975–977 (1989).

135. Maier, F., Riedel, M., Mantel, B., Ristein, J. & Ley, L. Origin of surface conductivity in diamond. *Physical review letters* **85,** 3472 (2000).

136. Strobel, P., Riedel, M., Ristein, J. & Ley, L. Surface transfer doping of diamond. *Nature* **430,** 439 (2004).

137. Kawarada, H. Hydrogen-terminated diamond surfaces and interfaces. *Surface Science Reports* **26,** 205–259 (1996).

138. Nebel, C. *et al.* Low temperature properties of the p-type surface conductivity of diamond. *Diamond and related materials* **11,** 351–354 (2002).

139. Nebel, C., Rezek, B. & Zrenner, A. Electronic properties of the 2D-hole accumulation layer on hydrogen terminated diamond. *Diamond and Related Materials* **13,** 2031–2036 (2004).

140. Edmonds, M. T., Pakes, C. I. & Ley, L. Self-consistent solution of the Schrödinger-Poisson equations for hydrogen-terminated diamond. *Physical Review B* **81,** 085314 (2010).

141. Edmonds, M. T. *et al.* Spin-orbit interaction in a two-dimensional hole gas at the surface of hydrogenated diamond. *Nano letters* **15,** 16–20 (2014).

142. Hirama, K. *et al.* Spontaneous polarization model for surface orientation dependence of diamond hole accumulation layer and its transistor performance. *Applied Physics Letters* **92,** 112107 (2008).

143. Dankerl, M. *et al.* Diamond transistor array for extracellular recording from electrogenic cells. *Advanced functional materials* **19,** 2915–2923 (2009).

144. Hirama, K. *et al.* High-performance P-channel diamond metal-oxide-semiconductor field-effect transistors on H-terminated (111) surface. *Applied physics express* **3,** 044001 (2010).

145. Kawarada, H. & Ruslinda, A. Diamond electrolyte solution gate FETs for DNA and protein sensors using DNA/RNA aptamers. *physica status solidi (a)* **208,** 2005–2016 (2011).

146. Yamaguchi, T. *et al.* Low-temperature transport properties of holes introduced by ionic liquid gating in hydrogen-terminated diamond surfaces. *Journal of the Physical Society of Japan* **82,** 074718 (2013).

147. Takahide, Y. *et al.* Quantum oscillations of the two-dimensional hole gas at atomically flat diamond surfaces. *Physical Review B* **89,** 235304 (2014).

148. Takahide, Y. *et al.* Spin-induced anomalous magnetoresistance at the (100) surface of hydrogen-terminated diamond. *Physical Review B* **94,** 161301 (2016).

149. Akhgar, G. *et al.* Strong and tunable spin-orbit coupling in a two-dimensional hole gas in ionic-liquid gated diamond devices. *Nano letters* **16,** 3768–3773 (2016).

150. Piatti, E., Galanti, F., Pippione, G., Pasquarelli, A. & Gonnelli, R. S. Towards the insulator-to-metal transition at the surface of ion-gated nanocrystalline diamond films. *European Physical Journal: Special Topics* **228,** 689–696 (2019).

151. Pippione, G., Olivero, P., Fischer, M., Schreck, M. & Pasquarelli, A. Characterization of CVD Heavily B-Doped Diamond Thin Films for Multi Electrode Array Biosensors. *physica status solidi (a)* **214,** 1700223 (2017).

152. Granado, T. C. *et al.* Progress in transparent diamond microelectrode arrays. *physica status solidi (a)* **212,** 2445–2453 (2015).

153. Ushizawa, K. *et al.* Boron concentration dependence of Raman spectra on {100} and {111} facets of B-doped CVD diamond. *Diamond and related materials* **7,** 1719–1722 (1998).

154. Lutterotti, L. Total pattern fitting for the combined size-strain-stress-texture determination in thin film diffraction. *Nuclear Instruments and Methods in Physics Research Section B: Beam Interactions with Materials and Atoms* **268,** 334–340 (2010).

155. Straumanis, M. & Aka, E. Precision Determination of Lattice Parameter, Coefficient of Thermal Expansion and Atomic Weight of Carbon in Diamond. *Journal of the American Chemical Society* **73,** 5643–5646 (1951).

156. Patterson, A. The Scherrer formula for X-ray particle size determination. *Physical review* **56,** 978 (1939).

157. Prawer, S. & Nemanich, R. J. Raman spectroscopy of diamond and doped diamond. *Philosophical Transactions of the Royal Society of London. Series A: Mathematical, Physical and Engineering Sciences* **362,** 2537–2565 (2004).

158. Bernard, M., Baron, C. & Deneuville, A. About the origin of the low wave number structures of the Raman spectra of heavily boron doped diamond films. *Diamond and Related Materials* **13,** 896–899 (2004).

159. Ferrari, A. & Robertson, J. Origin of the $1150 cm^{-1}$ Raman mode in nanocrystalline diamond. *Physical Review B* **63,** 121405 (2001).

160. Angus, J. C., Pleskov, Y. V. & Eaton, S. C. in *Semiconductors and semimetals* 97–119 (Elsevier, 2004).

161. Kraft, A. Doped diamond: a compact review on a new, versatile electrode material. *Int. J. Electrochem. Sci* **2,** 355–385 (2007).

162. Dankerl, M. *et al.* Hydrophobic interaction and charge accumulation at the diamond-electrolyte interface. *Physical review letters* **106,** 196103 (2011).

163. Dankerl, M., Tosun, M., Stutzmann, M. & Garrido, J. Solid polyelectrolyte-gated surface conductive diamond field effect transistors. *Applied Physics Letters* **100,** 023510 (2012).

164. Efetov, D. K. & Kim, P. Controlling electron-phonon interactions in graphene at ultrahigh carrier densities. *Physical review letters* **105,** 256805 (2010).

165. McMillan, W. Scaling theory of the metal-insulator transition in amorphous materials. *Physical Review B* **24,** 2739 (1981).

166. Larkin, A. & Khmel'nitskii, D. Activation conductivity in disordered systems with large localization length. *Sov. Phys. JETP* **56,** 647 (1982).

167. Heeger, A. J. The critical regime of the metal-insulator transition in conducting polymers: experimental studies. *Physica Scripta* **2002,** 30 (2002).

168. Gonon, P. *et al.* Characterization of heavily B-doped polycrystalline diamond films using Raman spectroscopy and electron spin resonance. *Journal of applied physics* **78,** 7059–7062 (1995).

169. Mott, N. F. & Davis, E. A. *Electronic processes in non-crystalline materials* (Oxford university press, 1979).

170. Mott, N. *Metal-Insulator Transition* (Oxford university press, 1990).

171. Lu, J. *et al.* Evidence for two-dimensional Ising superconductivity in gated MoS_2. *Science* **350,** 1353–1357 (2015).

172. Saito, Y., Kasahara, Y., Ye, J., Iwasa, Y. & Nojima, T. Metallic ground state in an ion-gated two-dimensional superconductor. *Science* **350,** 409–413 (2015).

173. http://www.ioffe.ru/SVA/NSM/Semicond/Diamond/bandstr.html#masses.

174. Collins, A. & Williams, A. The nature of the acceptor centre in semiconducting diamond. *Journal of Physics C: Solid State Physics* **4,** 1789 (1971).

175. Prosser, V. Sensitive method of measuring small changes in light intensities its use in measurements of high effective masses in semi-conductors from faraday rotation. *Cechoslovackij fiziceskij zurnal B* **15,** 128–134 (1965).

176. Braga, D., Gutiérrez Lezama, I., Berger, H. & Morpurgo, A. F. Quantitative determination of the band gap of WS_2 with ambipolar ionic liquid-gated transistors. *Nano letters* **12,** 5218–5223 (2012).

177. Stoppa, M. & Chiolerio, A. Wearable electronics and smart textiles: a critical review. *sensors* **14,** 11957–11992 (2014).

178. Torrisi, F. *et al.* Inkjet-printed graphene electronics. *ACS nano* **6,** 2992–3006 (2012).

179. Torrisi, F. & Carey, T. Graphene, related two-dimensional crystals and hybrid systems for printed and wearable electronics. *Nano Today* (2018).

180. Zhang, C. J. *et al.* Additive-free MXene inks and direct printing of micro-supercapacitors. *Nature communications* **10,** 1795 (2019).

181. Carey, T. *et al.* Fully inkjet-printed two-dimensional material field-effect heterojunctions for wearable and textile electronics. *Nature communications* **8,** 1202 (2017).

182. Torbatian, Z. & Asgari, R. Plasmonic physics of 2D crystalline materials. *Applied Sciences* **8,** 238 (2018).

183. Zhang, Y.-J. *et al.* Adsorption of uranyl species on hydroxylated titanium carbide nanosheet: A first-principles study. *Journal of hazardous materials* **308,** 402–410 (2016).

184. Kelly, A. G. *et al.* All-printed thin-film transistors from networks of liquid-exfoliated nanosheets. *Science* **356,** 69–73 (2017).

185. Alhabeb, M. *et al.* Guidelines for Synthesis and Processing of Two-Dimensional Titanium Carbide ($Ti_3C_2T_x$ MXene). *Chemistry of Materials* **29,** 7633–7644 (2017).

186. Ferrari, A. C. & Basko, D. M. Raman spectroscopy as a versatile tool for studying the properties of graphene. *Nature nanotechnology* **8,** 235 (2013).

187. Hu, J., Kang, Z., Li, F. & Huang, X. Graphene with three-dimensional architecture for high performance supercapacitor. *Carbon* **67,** 221–229 (2014).

188. Alyobi, M., Barnett, C. & Cobley, R. Effects of thermal annealing on the properties of mechanically exfoliated suspended and on-substrate few-layer graphene. *Crystals* **7,** 349 (2017).

189. Tian, S. *et al.* Facile thermal annealing of graphite oxide in air for graphene with a higher C/O ratio. *RSC Advances* **5,** 69854–69860 (2015).

190. Wu, J.-B., Lin, M.-L., Cong, X., Liu, H.-N. & Tan, P.-H. Raman spectroscopy of graphene-based materials and its applications in related devices. *Chemical Society Reviews* **47,** 1822–1873 (2018).

191. Schedin, F. *et al.* Detection of individual gas molecules adsorbed on graphene. *Nature materials* **6,** 652 (2007).

192. Ryu, S. *et al.* Atmospheric oxygen binding and hole doping in deformed graphene on a SiO2 substrate. *Nano letters* **10,** 4944–4951 (2010).

193. Xue, J., Huang, S., Wang, J.-Y. & Xu, H. Mott variable-range hopping transport in a MoS 2 nanoflake. *RSC Advances* **9,** 17885–17890 (2019).

194. Kim, J. S. *et al.* Electrical transport properties of polymorphic MoS2. *ACS nano* **10,** 7500–7506 (2016).

195. Yildiz, A., Serin, N., Serin, T. & Kasap, M. Crossover from nearest-neighbor hopping conduction to Efros-Shklovskii variable-range hopping conduction in hydrogenated amorphous silicon films. *Japanese Journal of Applied Physics* **48,** 111203 (2009).

196. Su, T.-I., Wang, C.-R., Lin, S.-T. & Rosenbaum, R. Magnetoresistance of $Al_{70}Pd_{22.5}Re_{7.5}$ quasicrystals in the variable-range hopping regime. *Physical Review B* **66,** 054438 (2002).

197. Gu, H. *et al.* Separating positive and negative magnetoresistance for polyaniline-silicon nanocomposites in variable range hopping regime. *Applied Physics Letters* **102,** 212403 (2013).

198. Sagar, R. U. R. *et al.* Large unsaturated room temperature negative magnetoresistance in graphene foam composite for wearable and flexible magnetoelectronics. *Nano Research* **12,** 101–107 (2019).

199. Rosenbaum, R. *et al.* Magnetoresistance of an insulating amorphous nickel-silicon film in large magnetic fields. *Physica B: Condensed Matter* **294,** 340–342 (2001).

200. Shklovskii, B. I. & Efros, A. L. *Electronic properties of doped semiconductors* (Springer Science & Business Media, 2013).

201. Halim, J. *et al.* Transparent conductive two-dimensional titanium carbide epitaxial thin films. *Chemistry of Materials* **26,** 2374–2381 (2014).

202. Bergmann, G. Quantitative analysis of weak localization in thin Mg films by magnetoresistance measurements. *Physical Review B* **25,** 2937 (1982).

203. Fivaz, R. & Mooser, E. Mobility of charge carriers in semiconducting layer structures. *Physical Review* **163,** 743 (1967).

204. Yu, Z. *et al.* Analyzing the Carrier Mobility in Transition-Metal Dichalcogenide MoS_2 Field-Effect Transistors. *Advanced Functional Materials* **27,** 1604093 (2017).

205. Blanter, Y. M., Vinokur, V. & Glazman, L. Weak localization in metallic granular media. *Physical Review B* **73,** 165322 (2006).

206. Biagini, C., Caneva, T., Tognetti, V. & Varlamov, A. Weak localization effects in granular metals. *Physical Review B* **72,** 041102 (2005).

207. Fashandi, H. *et al.* Dirac points with giant spin-orbit splitting in the electronic structure of two-dimensional transition-metal carbides. *Physical Review B* **92,** 155142 (2015).

208. Hikami, S., Larkin, A. I. & Nagaoka, Y. Spin-orbit interaction and magnetoresistance in the two dimensional random system. *Progress of Theoretical Physics* **63,** 707–710 (1980).

209. Bergmann, G. Weak localization in thin films: a time-of-flight experiment with conduction electrons. *Physics Reports* **107,** 1–58 (1984).

210. Altshuler, B. L., Aronov, A. & Khmelnitsky, D. Effects of electron-electron collisions with small energy transfers on quantum localisation. *Journal of Physics C: Solid State Physics* **15,** 7367 (1982).

211. *Hall Effect Measurements* https://www.nist.gov/pml/engineering-physics-division/popular-links/hall-effect.

212. Tang, Z. *et al.* Resistive switching properties of Ce and Mn co-doped BiFeO3 thin films for nonvolatile memory application. *AIP Advances* **3,** 122117 (2013).

213. Boyn, S. *Ferroelectric tunnel junctions: memristors for neuromorphic computing* PhD thesis (Paris Saclay, 2016).

214. Medeiros, O., Colangelo, M., Charaev, I. & Berggren, K. K. Measuring thickness in thin NbN films for superconducting devices. *Journal of Vacuum Science & Technology A: Vacuum, Surfaces, and Films* **37,** 041501 (2019).

215. Ermolieff, A. & Bernard, P. Angular X-ray photoelectron spectroscopy study of N (1s) and O (1s) lines during controlled oxidation of NbN thin film. *Journal of the Less Common Metals* **120,** 9–20 (1986).

This Ph.D. thesis has been typeset by means of the TEX-system facilities. The typesetting engine was pdfLATEX. The document class was `toptesi`, by Claudio Beccari, with option `tipotesi=scudo`. This class is available in every up-to-date and complete TEX-system installation.